Lithium- and oxygen-isotope compositions of chondrule constituents in the Allende meteorite

Tak Kunihiro*, Tsutomu Ota, and Eizo Nakamura (Accepted by Geochimica et Cosmochimica Acta on February 26, 2019)

The Pheasant Memorial Laboratory
Institute for Planetary Materials, Okayama University
Yamada 827, Misasa, Tottori 682-0193, Japan

Abstract

We report in situ ion-microprobe analyses of Li- and O-isotope compositions for olivine, low-Ca pyroxene, high-Ca pyroxene, and chondrule mesostasis/plagioclase in nine chondrules from the Allende CV3 chondrite. Based on their mineralogy and O-isotope compositions, we infer that the chondrule mesostasis/plagioclase and ferroan olivine rims were extensively modified or formed during metasomatic alteration and metamorphism on the Allende parent asteroid. We exclude these minerals in order to determine the correlations between Li and both O and the chemical compositions of olivines and low-Ca pyroxenes in the chondrules and their igneous rims. Based on the O-isotope composition of the olivines, nine chondrules were divided into three groups. Average Δ^{17}O of olivines ($Fo_{>65}$) in group 1 and 2 chondrules are -5.3 ± 0.4‰ and -6.2 ± 0.4‰, respectively. Group 3 chondrules are characterized by the presence of ^{16}O-rich relict grains and the Δ^{17}O of their olivines range from -23.7 to -6.2‰. In group 1 olivines, as Fa content increases, variation of δ^7Li becomes smaller and δ^7Li approaches the whole-rock value (2.4‰; Seitz et al., 2012), suggesting nearly complete Li-isotope equilibration. In group 2 and 3 olivines, variation of δ^7Li is limited even with a significant range of Fa content. We conclude that Li-isotope compositions of olivine in group 1 chondrules were modified not by an asteroidal process but by an igneous-rim formation process, thus chondrule olivines retained Li-isotope compositions acquired in the protosolar nebula. In olivines of the group 3 chondrule PO-8, we observed a correlation between O and Li isotopes: In relict ^{16}O-rich olivine grains with Δ^{17}O of ~ -25 to -20‰, δ^7Li ranges from -23 to -3‰; in olivine grains with Δ^{17}O > -20‰, δ^7Li is nearly constant (-8 ± 4‰). Based on the Li-isotope composition of low-Ca pyroxenes, which formed from melt during the crystallization of host chondrules and igneous rims, the existence of a gaseous reservoir with a δ^7Li ~ -11‰ is inferred.

Keywords: lithium, oxygen, chondrule, chondrite, asteroid, Allende, igneous rim, SIMS

*tkk@misasa.okayama-u.ac.jp

1. INTRODUCTION

Type 3 carbonaceous and ordinary chondrites have long been considered as primordial materials, relatively unchanged since their formation; however, most have been altered by interaction with aqueous fluid on their parent asteroids (Krot et al., 1995; Zolensky et al., 2008; Brearley, 2014). Lithium is highly soluble in aqueous fluids (Brenan et al., 1998) and Li isotopes exhibit significant fractionation in geologic materials (δ^7Li ranges from -20 to 40‰) because of the large mass difference between ^{6}Li and ^{7}Li (e.g., Tomascak et al., 2016). Solid phases preferentially retain ^{6}Li, while ^{7}Li preferentially enters solution. These unique geochemical characteristics of Li make it possible to trace aqueous alteration processes on asteroids.

Despite the potential role of Li as a geochemical tracer, its behavior with respect to geological processes, operating in the early solar system, is not well understood. Hanon et al. (1999) reported a wide range of Li abundances in chondrules using secondary ion mass spectrometry (SIMS). Chaussidon and Robert (1998) found a significant range of Li-isotope compositions (δ^7Li from -13 to +35‰) in chondrules from the Semarkona LL3.01 (Kimura et al., 2008) chondrite and interpreted these variations as a result of heterogeneity inherited from chondrule precursors. McDonough et al. (2003) and Seitz et al. (2007) determined the Li-isotope compositions (δ^7Li) of whole-rock carbonaceous and ordinary chondrites using inductively coupled plasma mass spectrometry (ICP-MS); the whole-rock δ^7Li range from -3.5 to +3.9‰ (McDonough et al., 2003) and from +1.8 to +5.4‰ (Seitz et al., 2007), respectively. McDonough et al. (2003) found a negative correlation between δ^7Li and the petrologic type of carbonaceous chondrites, suggesting that alteration on asteroids made the Li-isotope composition heavier. They inferred that isotopically heavy fluids had interacted with asteroidal materials to produce hydrous minerals that are enriched in ^{7}Li. Maruyama et al. (2009) carried out in situ Li-isotope analyses of chondrule olivines in the Allende meteorite using SIMS and suggested that variation of $\sim$ 50‰ observed in chondrule olivines could reflect a nebular process rather than an asteroidal process. Recently, Seitz et al. (2012) determined whole-rock Li-isotope compositions of chondrules, refractory inclusions, and dark inclusions from Allende and ordinary chondrites and demonstrated that the δ^7Li in these materials ranges from -8.5 to +10‰. Whilst these previous studies have contributed to our understanding of the behavior of Li in the early solar system, much concerning the role of asteroidal and nebular processes remains unclear.

Chondrules are the most abundant components in most chondrites and are believed to have formed in the solar nebula from clumps of precursor dust during repeatable transient heating events (e.g., Grossman, 1988; Jones, 1996a; Rubin, 1996; Hewins, 1997). Chondrules are composed of olivine, low-Ca pyroxenes, high-Ca pyroxenes, plagioclase, glass, metal, and sulfides. These phases respond differently to nebular and asteroidal processes. Variations of Li-isotope compositions observed in the above phases could have resulted from those of chondrule precursors, isotope fractionation

between silicates and melt, devolatilization, condensation, and interaction with isotope reservoirs, during nebular and asteroidal processes. Fully constraining the behavior of Li in these meteorites requires a more comprehensive approach involving analyses of a broader array of element and isotope compositions than previously investigated.

In order to understand the behavior of Li during nebular and asteroidal processes, we report the Li- and O-isotope compositions of individual minerals in the Allende chondrules and their igneous rims. We subsequently examine the formation and alteration processes associated with these phases.

2. EXPERIMENTAL METHODS

2.1. Major elements

The major-element and minor-element compositions of mineral phases (olivine, low-Ca pyroxene, high-Ca pyroxene, and plagioclase) were determined by electron microprobe (EPMA) in wavelength-dispersive mode using a JEOL JXA-8530F. The analyses were conducted at routine conditions (15 kV acceleration voltage and 12 nA beam current) and the oxide ZAF method was employed for matrix corrections. Calibration was undertaken using silicate, sulfide, oxide, and synthetic oxides minerals, which were assembled on a standard ASTIMEX, MINM25-53+FC mount (Astimex Standards Ltd., Canada). Major-element compositions of glass were determined using a JEOL JSM-7001F SEM equipped with energy dispersive X-ray spectrometers (EDS) and Oxford AZtec X-Max and X-act. The analyses were conducted under routine conditions (10 kV acceleration voltage, 3 nA beam current, and 100 s integration times).

2.2. Oxygen-isotope compositions

Oxygen-isotope compositions were determined by SIMS using a modified Cameca ims-1270 at the Pheasant Memorial Laboratory (PML). Thick sections were coated with 75 nm of Au to avoid charging. At the same surface condition, isotope compositions were determined relative to that of a working standard, and matrix effects of minerals were estimated based on analyses of a working standard on a different mount. A Cs^+ primary beam (200 pA) of 20 keV was focused and scanned on the sample surface by 5×5 μm^2, yielding a 6×6 μm^2 crater. Secondary O^- was accelerated to −10 kV and a normal incident electron gun was used to compensate positive charging on the sputtered area. In order to minimize the generation of OH^- secondary ions, a pressure of less than 5×10^{-9} Torr was maintained in the specimen chamber using a cold trap filled with liquid nitrogen. A contrast aperture of 400 μm was used and an optical gate of 1300×1300 μm^2, which corresponds to 25×25 μm^2 on the sample surface, was inserted and an energy band pass set from −10 to 30 eV. The mass-resolution was set to 5,000 for $^{17}O^-$ and 2,400 for $^{16}O^-$ and $^{18}O^-$. At these resolutions it was possible to

resolve OH^- interference at less than the 0.1‰ level. The pre-sputtering time, including auto peak-centering, was 190 s. Signal intensities were simultaneously determined by a Faraday cup mounted on trolley L2 ($^{16}O^-$) and pulse counting was done using electron multipliers located on axial ($^{17}O^-$) and trolley H1 ($^{18}O^-$). Typical ion intensities for $^{16}O^-$, $^{17}O^-$, and $^{18}O^-$ were 50M, 20k, and 100k cps, respectively. The ion-integration times were 14.5 s in each cycle, and each run consisted of 40 cycles. Typical external precision, estimated by repeated analyses of a working standard, was 0.3‰ (1SD) for both $\delta^{18}O$ and $\delta^{17}O$. The deviation of oxygen's isotope ratios from the terrestrial mass fractionation line is represented by $\Delta^{17}O = \delta^{17}O - 0.52 \times \delta^{18}O$ (Clayton, 1993).

Matrix effects on instrumental mass fractionation are known to occur for oxygen-isotope measurements (Hervig et al., 1992; Eiler et al., 1997; Leshin et al., 1997; Gurenko et al., 2001; Gurenko and Chaussidon, 2002; Isa et al., 2017). In order to understand the matrix effects, we first attached importance to chemical varieties represented by X_{Mg} ($\equiv \frac{[Mg]^{mol}}{[Fe]^{mol}+[Mg]^{mol}}$), X_{Ca} ($\equiv \frac{[Ca]^{mol}}{[Fe]^{mol}+[Mg]^{mol}+[Ca]^{mol}}$), and X_{Na} ($\equiv \frac{[Na]^{mol}}{[Ca]^{mol}+[Na]^{mol}+[K]^{mol}}$). We then examined the matrix effects through comparison with a working standard, San Carlos olivine ($\Delta\delta^{18}O^{phase}_{ol\cdot sc}$), analyses of reference olivines (Fo_{48-100}), low-Ca pyroxenes ($En_{88-91}Wo_{0.3-2}$), high-Ca pyroxenes ($En_{45-50}Wo_{37-50}$), plagioclases (Ab_{40-98}), and glass (Ab_{53-100}) (Appendix 1.1. and Table S1). We found that the matrix effects were mass dependent. Thus we calculated the matrix effects for $\delta^{17}O$ from that of $\delta^{18}O$ ($\Delta\delta^{17}O = 0.52 \times \Delta\delta^{18}O$) and no correction was necessary $\Delta^{17}O$.

In this study, we determined O-isotope compositions of olivine (Fo_{62-100}), low-Ca pyroxene ($En_{90-98}Wo_{1-9}$), high-Ca pyroxene ($En_{54-74}Wo_{26-45}$), and plagioclase (Ab_{17-19}) in Allende chondrules. The estimated matrix effects were negligibly small for olivine Fo_{70-100}, and plagioclase Ab_{17-19}, being within a reproducibility of ~0.2–0.3‰ (1SD) $\delta^{18}O$ for the working standard, thus we did not apply the matrix effect correction for these phases. Whereas for olivine (Fo_{62-70}), low-Ca pyroxene ($En_{90-98}Wo_{1-9}$), and high-Ca pyroxene ($En_{54-74}Wo_{26-45}$), we confirmed existence of significant matrix effects related with their chemical compositions (Table S2 and Figure S1). Therefore, we defined formula to represent their matrix effects, and corrected them for olivines and pyroxenes with particular chemical compositions (Appendix 1.1.).

2.3. Lithium concentrations and isotope compositions

Lithium-isotope compositions were determined by SIMS using the modified Cameca ims-1270 at the PML. Thick sections were coated with 30 nm of Au to avoid charging. O-isotope and Li-isotope measurements were carried out onto the same spots. However, in some cases spot locations differed by 20 μm. The primary O^- ion beam was accelerated to −23 keV and the primary beam current was varied from 1 to 15 nA to maintain constant secondary ion-intensity. A contrast aperture of 400 μm was used. An optical gate that corresponds to 50×50 μm^2 on sample surface was inserted and the energy band

pass was set to 0±50 eV. In order to attain a mass resolution of 1200, which is sufficient to eliminate interference from $^{6}LiH^{+}$, the width of the entrance- and exit-slits was set to 400 and 1200 μm, respectively. The intensity ratio of $^{6}Li^{+}$ and $^{7}Li^{+}$ was determined in magnetic peak-jumping mode by ion counting with an electron multiplier. Integration times for $^{6}Li^{+}$ and $^{7}Li^{+}$ were 4 and 1 s in each cycle, respectively, and each run consisted of 110 cycles. Craters were less than 20 μm in diameter. Lithium concentrations for the analyzed spots were estimated using ($^{7}Li^{+}/I_{PRI}$), where I_{PRI} is the primary ion-probe current.

As was the case for O-isotope analysis, instrumental mass fractionation represents one of the major difficulties in high-precision Li-isotope analysis by SIMS (e.g., Bell et al., 2009). Isotope compositions were determined by the formula $\delta^{7}Li = \delta^{7}Li^{\oplus} - \Delta\delta^{7}Li_{ws}^{phase}$, where $\delta^{7}Li^{\oplus}$ is the ion-intensity ratio that was used to correct the instrumental mass fractionation ($\delta^{7}Li^{\oplus} \equiv \delta^{7}Li^{+} - f_{IMF}$), and $\Delta\delta^{7}Li_{ws}^{phase}$ is the relative matrix effect of a particular phase relative to a working standard. Note that f_{IMF} is estimated using the working standard.

To evaluate the matrix effects relative to working standards, we analyzed reference olivine (Fo_{1-99}), low-Ca pyroxene ($En_{98}Wo_{0.1}$), high-Ca pyroxene ($En_{82-84}Wo_{31-39}$), and plagioclase (Ab_{42-72}) (Appendix 1.1. and Table S1). Significant matrix effects were recognized for olivines with Fo_{1-99} and between the working standards and the other reference materials. Therefor, we estimated $\Delta\delta^{7}Li_{ws}^{phase}$ for olivine, pyroxene, and plagioclase based on linear correlations between the matrix-related bias and the chemical composition of those phases (Table S3 and Figure S2). For olivine (Fo_{62-100}) in the Allende chondrules, matrix effects were estimated based on a linear correlation with chemical varieties, and the matrix effects were corrected. The estimated matrix effects of low-Ca and high-Ca pyroxenes (Wo_{1-9} and Wo_{26-45}) and plagioclase (Ab_{17-19}) in chondrules relative to the working standard en-sl1 were negligibly small, being within or comparable to analytical reproducibilities (1SD) for the working standards, en-sl1 (δ^{7}Li 2.6‰) or ol-sc1 (δ^{7}Li 0.6‰). Thus we did not apply the matrix effect correction on the pyroxenes and the plagioclase; further details are described in Appendix 1.1.

3. RESULTS

3.1. Sample Descriptions

Nine chondrules, including chondrule fragments, were hand-picked after disaggregation from the Allende meteorite and embedded in a resin mount with working standard materials (San Carlos olivine). They are shown in Figure 1 and classified as porphyritic-olivine (PO) chondrules, barred-olivine (BO) chondrules, and a barred-olivine-pyroxene (BOP) chondrule (Scott and Krot, 2014; Jones, 1990, 1994, 1996b,a). The major-element compositions for olivine, low-Ca pyroxene, high-Ca pyroxene, and plagioclase

in the chondrules are summarized in Table 1.

BOP-2 is a 2.0 mm-sized compound chondrule (Figs. 1a, 2a, 2b, S3a), which consists of a 1.0 mm-sized inner BO, a 2.0-mm sized outer BOP, and an igneous rim. The inner BO consists of olivine (Fo_{88-99}), mesostasis, and opaques. Olivine bars are typically 50 μm in width, elongated along a north east direction and surrounded by a 100 μm thick olivine and opaque rich shell. The mesostasis is dominated by An-rich plagioclase ($Ab_{18-24}An_{76-82}$), low-Ca pyroxene ($En_{94}Wo_5$), high-Ca pyroxene ($En_{60-78}Wo_{21-39}$), Ab-rich glass ($Ab_{84-89}An_{5-11}$), and opaques. The outer BOP consists of olivine (Fo_{95-99}), mesostasis, low-Ca pyroxene ($En_{90-99}Wo_{9-1}$), high-Ca pyroxene ($En_{57-74}Wo_{42-26}$), and opaques. The typical width of olivine and low-Ca pyroxene bars is 100 and 200 μm, respectively. Some barred olivines are surrounded by low-Ca pyroxenes. The mesostasis consists of Ab-rich glass ($Ab_{81-88}An_{19-5}$), low-Ca pyroxene ($En_{91-93}Wo_{7-6}$), high-Ca pyroxene ($En_{60-71}Wo_{39-28}$), and opaques. Bars of olivine and low-Ca pyroxene, elongated along a north east direction, are surrounded by a shell with a thickness of 140 μm. The shell consists of olivine and opaques, and is surrounded by an igneous rim of low-Ca pyroxene, olivine, and opaques. Olivine is anhedral and enclosed by low-Ca pyroxene (Fig. 2a).

PO-6 is a 2.3 mm-sized fragment of a PO chondrule with an igneous rim (Fig. 1b). The main region consists of olivine (Fo_{63-99}) and mesostasis, and the igneous rim consists of olivine, low-Ca pyroxene ($En_{96-98}Wo_1$), high-Ca pyroxene ($En_{58-66}Wo_{40-32}$), and opaques. The chondrule mesostasis consists of albitic glass ($Ab_{88-89}An_5$) and high-Ca pyroxene ($En_{70-80}Wo_{17-26}$). Typical sizes of olivine in the chondrule and its igneous rim are 100 μm and 20 μm, respectively.

BO-4 is a 1.7 mm-sized BO chondrule composed of olivine (Fo_{73-99}), mesostasis and opaques and surrounded by a 100 μm thick olivine (Fo_{90-95}) shell of (Figs. 1c, S3b). Olivines in the main region occur as bars aligned at two angles. Typical bar width is 20 μm, and the largest one is 200 μm (with a length of 800 μm). The mesostasis consists of An-rich glass (Ab_9An_{91}), anhedral low-Ca pyroxene ($En_{92}Wo_7$), anhedral high-Ca pyroxene ($En_{56-89}Wo_{11-37}$), and opaques.

PO-7 is a 1.3 mm-sized fragment of a PO chondrule (Figs. 1d, 2c) with an igneous rim. The main region consists of olivine (Fo_{90-98}) and albitic mesostasis ($Ab_{87}An_6$). Whereas the the igneous rim is composed of olivine, low-Ca pyroxene ($En_{98}Wo_9$), and opaques.

PO-1 is a 1.7 mm-sized fragment of a PO chondrule (Fig. 1e). The chondrule consists of olivine (Fo_{65-100}), euhedral low-Ca ($En_{92-95}Wo_{6-4}$) and high-Ca ($En_{54-59}Wo_{45-40}$) pyroxene and mesostasis (Fig. 1e). The mesostasis is dominated by Ab-rich glass ($Ab_{63-73}An_{32-21}$) with anhedral high-Ca pyroxene ($En_{24-47}Wo_{34-49}$). The typical size of olivine crystals is 80 μm. Olivines near the exterior of the chondrule are enriched in FeO compared to those in its core (Fo_{82-96} vs Fo_{86-99}).

PO-3c is a 160 μm-sized fragment of a PO chondrule that consists of olivine (Fo_{62-93})

(Fig. 1f). Similarly, PO-3s is a 180 μm-sized fragment of a PO chondrule that consists of olivine (Fo_{86-99}) (Fig. 1g).

PO-8 is a 1.6 mm-sized PO chondrule surrounded by an igneous rim (Figs. 1h, 2d, S3c). The chondrule has a core-mantle structure. The diameter of the core region is 500 μm and the thickness of the mantle and igneous rims are 500 μm and 100 μm, respectively. All three units are dominated by olivine (Fo_{81-98}) and opaques and their typical size in the mantle region is 40 μm. In addition to the aforementioned phases, the mantle region contains mesostasis, whilst the igneous rim comprises of low-Ca ($En_{92-93}Wo_{6-5}$) and high-Ca pyroxene ($En_{57-66}Wo_{42-33}$). The mesostasis consists of An-rich plagioclase ($Ab_{17-19}An_{83-81}$).

PO-3n is a 600 μm-sized fragment of a PO chondrule, which is composed of olivine (Fo_{77-95}), mesostasis, anhedral low-Ca pyroxene ($En_{96-98}Wo_{2-1}$), and opaques (Fig. 1i). The mesostasis consists of anorthitic glass ($Ab_{8-9}An_{92-91}$). The typical size of the olivine is 50 μm. This chondrule is surrounded by fayalitic olivines (shown in the lower left of Fig. 1i).

3.2. Oxygen-isotope compositions

All the chondrules described above were measured for their oxygen-isotope compositions and these analyses are shown in Table S4 and Figure 3. The isotope compositions of minerals and the chondrule they were measured in are summarized in Table 2. On the O isotope diagram shown in Figure 3, $\delta^{18}O$ and $\delta^{17}O$ values of chondrule minerals (olivine, low-Ca pyroxene, high-Ca pyroxene, and plagioclase) scatter around the PCM (primitive chondrule mineral) line (slope of 0.987 and intercept of −2.70; Ushikubo et al., 2012) and the Y&R line (slope of 1.00 ± 0.03 and intercept of −1.04; Young and Russell, 1998). These O-isotope compositions are in good agreement with those previously obtained by whole rock and in situ analyses of CV chondrules (Clayton, 1981; Rubin et al., 1990; Jones et al., 2000; Rudraswami et al., 2011).

Based on the O-isotope composition of the olivines, the nine chondrules studied here were divided into three groups. Average $\Delta^{17}O$ values of olivine ($Fo_{>65}$) in chondrules BOP-2, PO-6, and BO-4 (group 1) are −5.3, −5.2, and −5.4‰, varying by <1‰ (1SD). Average $\Delta^{17}O$ values of olivine ($Fo_{>65}$) in chondrules PO-7, PO-1, PO-3c, and PO-3s (group 2) are −6.1, −6.5, −6.3, and −6.0‰, varying by <1‰ (1SD). The average $\Delta^{17}O$ of olivine compositions in chondrules of group 1 and 2 are −5.3±0.4‰ and −6.2±0.4‰, respectively. Olivines in chondrules PO-8 and PO-3n (group 3) show variations in $\Delta^{17}O$ from −23.7 to −6.2‰.

In group 1, the $\delta^{18}O$ of olivine grains range from $\delta^{18}O$ −6‰ to −3‰, pyroxene is similar but slightly more $\delta^{18}O$-rich, and plagioclase in BOP-2 and FeO-rich olivines in PO-6, are a lot more $\delta^{18}O$-rich. In group 2, the $\delta^{18}O$ of olivine, low-Ca pyroxene, and high-Ca pyroxenes are $\sim$ −6‰, and FeO-rich olivines in PO-1 and PO-3c are a lot more $\delta^{18}O$-rich. In group 3, $\delta^{18}O$ of olivines range from −50‰ to −10‰. O-isotope

compositions of chondrule constituents in each group are summarized in Table 3 and Figures 5a,c,e. Further details are described in Appendix 1.2.

3.3. Lithium concentrations and isotope compositions

All chondrules measured for O-isotope compositions were also measured for Li-isotope compositions. All analyses are shown in Table S4 and Figure 4.

Low-Ca pyroxenes and plagioclases are the most Li enriched and depleted phases, respectively. Li-isotope compositions range from δ^7Li $-33‰$ (low-Ca pyroxene) to $+39‰$ (olivine). There is no obvious correlation between Li concentration [Li] and isotope composition (Fig. 4). Li concentration and isotope compositions of minerals that are organized by occurrences in each chondrule are summarized in Table 2. The portion of results is visualized in Figure 2. Spatial distributions of [Li] and δ^7Li are not systematic (Fig. 2).

The Li-isotope composition of chondrule constituents in each group is summarized in Table 3 and Figures 5b,d,f. Further details are described in Appendix 1.3.

4. DISCUSSION

4.1. The origin of phases in Allende chondrules

The Allende CV3 meteorite consists of chondrules, refractory inclusions and matrix and experienced significant alteration (e.g., Krot et al., 1995). Prior to investigation of Li behavior, we will evaluate the petrogenesis and alteration of Allende chondrule constituents.

Olivine occurs as phenocrysts and relict grains in chondrules (Ol) and igneous rims (Ol^{irim}), and as FeO-rich rims around phenocrysts (Ol^{FeO}). Chondrule olivine phenocrysts are typically euhedral, while olivine within igneous rims is anhedral. Some olivines are MgO-rich ($Fo_{\geq 95}$), whereas others possess higher Fe/Mg ratios (Fo_{65-95}). Igneous rims are present in about 50% of Allende chondrules and are also referred to as coarse-grained rim. Igneous rims are mostly composed of olivine and low-Ca pyroxene, although sulfide and metallic Fe-Ni are also present in minor amounts (Rubin, 1984). On average, Ol^{irim} is more enriched in Fe (Fo_{78-92}) relative to Ol. Ol^{FeO} is a minor constituent which occurs adjacent to Ol and forms euhedral crystals with significant Fe contents ($Fo_{\leq 65}$). Fe-enriched olivine is widespread in oxidized CV chondrites, being found in the rim, along cracks, and around Fe, Ni metal and sulfide inclusions, which form on forsteritic olivine phenocrysts (Brearley, 2014). The Fe-enriched olivines are formed through alteration on the parent body (Krot et al., 1995, 1998).

For Allende, Acfer 094, and CO chondrites, Δ^{17}O values of chondrules display a bimodal distribution with peaks at -5 and $-2.5‰$ (Rudraswami et al., 2011; Ushikubo et al., 2012; Tenner et al., 2013, 2015). Rudraswami et al. (2011) demonstrated that

O-isotope compositions of Allende chondrules formed from melt with a former $\Delta^{17}O$ reservoir range of -6 to -4.5‰. Similarly, O-isotope compositions of Ol, in group 1 and 2 chondrules from this study, suggest olivine formed from melt with a former O-isotope reservoir during chondrule formation, as they cooled from their peak temperature.

Chondrules PO-8 and PO-3n show internal O isotope variation above analytical uncertainties. The variations observed within the two chondrules are similar to those of heterogeneous chondrules from Mokoia, Allende, and Acfer 094 (Jones et al., 2004; Rudraswami et al., 2011; Ushikubo et al., 2012). The two chondrules contain olivine that is significantly ^{16}O-rich, which likely represents relict material that formed prior to chondrule formation, such as related to refractory inclusions and amoeboid olivine aggregates.

Group 1 and 2 chondrules were either more extensively melted or did not contain such relict grains. Chondrule BOP-2 consists of five layers (inner BO, shell of inner BO, outer BOP, shell of outer BOP, and igneous rim), and olivines from the five layers are indistinguishable within analytical uncertainties, suggesting that efficient O isotope exchange occurred between ambient gas and chondrule melt.

Plagioclase (Pl) is the last silicate to crystallized from a chondrule melt and occurs in the main chondrule as a constituent of the mesostasis. Pl has an average $\Delta^{17}O$ of -3.3 ± 0.5‰ and is significantly depleted in ^{16}O compared to Ol, which is rather consistent with the average $\Delta^{17}O$ of the matrix and whole rock (-2.87 and -3.52‰; Clayton and Mayeda, 1999). During parent body metamorphism, the O-isotope composition of 10 μm-sized anorthitic plagioclase could be completely modified, when considering the experimentally determined self-diffusion rate (Ryerson and McKeegan, 1994; Rudraswami et al., 2011). Pl can originate from either a chondrule formation or asteroidal process. Even in the case of chondrule formation, the ^{16}O-poor composition must result from an asteroidal process.

Ol^{FeO} is 10 μm in size, enriched in Fe (Fo_{61-65}) and infills 100 μm-sized Ol (Fig. 1f). Self-diffusion rates of O in olivine and pyroxene are several orders magnitude lower than that in anorthitic plagioclase (Ryerson and McKeegan, 1994; Cole and Chakraborty, 2001), so that O-isotope compositions recorded in these minerals during chondrule formation would not be affected by the metamorphism (Rudraswami et al., 2011). Ol^{FeO} has a similar O-isotope composition ($\Delta^{17}O$ -2.6 ± 0.9‰) to that of Pl and thus it is considered to be indicative of an asteroidal process (Imai and Yurimoto, 2003).

Low-Ca and high-Ca pyroxenes occur in both the main body of the chondrules and their igneous rims and are referred to as LPx and LPx^{irim} and HPx and HPx^{irim}, respectively. The O-isotope compositions of Ol, LPx, LPx^{irim}, and HPx of group 2 are indistinguishable. This finding suggests that the chondrule constituents formed from a melt with a homogeneous O-isotope composition, which reflects that of the ambient gas present during high temperature chondrule formation (Rudraswami et al., 2011).

Similarly to group 2, the $\Delta^{17}O$ values of group 1 Ol, Ol^{irim}, LPx, LPx^{irim}, and HPx

are essentially indistinguishable: -5.3 ± 0.4, -5.0 ± 0.4, -5.4 ± 0.4, -5.1 ± 0.4, and -5.6 ± 0.5‰, respectively. However, δ^{18}O values for LPx, LPx$^{\mathrm{irim}}$, and HPx (-3.1 ± 0.7, -2.4 ± 1.1, and -2.5 ± 0.9‰) are higher than those for Ol (-4.8 ± 0.8‰).

The existence of a gap in δ^{18}O between olivines and pyroxenes is consistent with the model of Chaussidon et al. (2008). They proposed that most of the olivine is relict and that the pyroxene was formed by interaction between the melt of a precursor dominated by olivine and gas of a constant isotope composition (δ^{18}O, δ^{17}O = 1.2‰, 0.6‰, respectively). Using the proposed formulas by Chaussidon et al. (2008), the expected δ^{18}O and δ^{17}O of pyroxenes for group 1 is calculated to be -2.2‰ and -5.7‰, respectively and our measured values for pyroxenes from group 1 chondrules are -3.1‰ and -7.0‰, respectively. The observed δ^{18}O is 1‰ lighter than predicted and our observation is not consistent with the proposed gas having a constant O-isotope composition. Furthermore, the model of Chaussidon et al. (2008) cannot explain the similar Δ^{17}O of olivine and low-Ca pyroxene in the chondrules of group 1 and 2.

The O-isotope composition of olivine and pyroxene in group 1 and 2 chondrules have the same Δ^{17}O but the pyroxenes have heavier δ^{18}O than the olivines, which is opposite to the trend reported by Rudraswami et al. (2011), Ushikubo et al. (2012), and Tenner et al. (2013, 2015). These authors explain their observed trend by preferential evaporation of light isotopes from the melt during chondrule formation, prior to olivine crystallization. After crystallization of olivine, recondensing ambient gas could have supplied the melt with light isotope as it cooled, prior to pyroxene crystallization. However, our O-isotope compositions, for melt associated with group 1 chondrules, because heavier between the crystallization of Ol and LPx. Such a relationship could arise if evaporation was not terminated during crystallization of pyroxenes. Alternatively, melt-gas reactions involving gas of a constant or changing O-isotope composition may have started to play a role during the crystallization of pyroxene.

Although the average Fe/Mg ratio of Ol$^{\mathrm{irim}}$ is larger than that of Ol, both the Δ^{17}O and δ^{18}O values of Ol$^{\mathrm{irim}}$ are indistinguishable to those of Ol. One possible explanation is that Ol$^{\mathrm{irim}}$ and LPx$^{\mathrm{irim}}$ formed during the later stages of chondrule formation from a melt with a fluctuating temperature and O-isotope composition. The addition of SiO to the outer part of a chondrule would also be necessary (Jones et al., 2005). However, the petrographic observation (Ol$^{\mathrm{irim}}$ is anhedral and poikilitically enclosed by LPx$^{\mathrm{irim}}$) suggests that the igneous rim underwent partial melting, which was caused by a secondary heating event, after the formation of the chondrule (Krot and Wasson, 1995). We refer to the heating and cooling processes that formed LPx$^{\mathrm{irim}}$ from the melt as igneous-rim formation processes. The O-isotope compositions suggest that Ol$^{\mathrm{irim}}$ formed from melt during chondrule formation, with the Fe/Mg ratio modified and O-isotope composition maintained during the igneous-rim formation. Subsequently, LPx$^{\mathrm{irim}}$ formed from melt during the igneous-rim formation with the same O-isotope composition as LPx.

Rubin et al. (1990) determined O-isotope compositions of Allende main chondrule

bodies and their igneous rims using a conventional method and demonstrated that igneous rims tend to have higher Δ^{17}O, up to 1.3‰ relative the main region. It is likely that the presence of secondary phases in the igneous rim, such as plagioclase, results in these higher Δ^{17}O values.

4.2. Lithium isotope systematics

Lithium concentration [Li] and δ^7Li of whole-rock Allende are 1.93 $\mu g \cdot g^{-1}$ and 2.4‰ (Seitz et al., 2012), respectively. Lithium concentrations of olivine, mesostasis, and low-Ca pyroxene in Allende chondrules range from 0.1 to 3.5 $\mu g \cdot g^{-1}$. The δ^7Li of the olivine in Allende ranges from −32 to +21‰ (Maruyama et al., 2009).

4.2.1 Effects of alteration processes on the CV asteroid and in the solar nebula

Relative to Ol and Ol^{irim}, Ol^{FeO} has a low Liconcentration ($0.05 < [Li] < 0.3\ \mu g \cdot g^{-1}$) and its Li-isotope composition (δ^7Li=3 ± 2‰) is consistent with that of the whole rock (Figs. 5d,e,f). The same feature is observed for Pl ($0.008 < [Li] < 0.1\ \mu g \cdot g^{-1}$, δ^7Li 0 ± 5‰). The identical Δ^{17}O of Ol^{FeO} and Pl and their common Li concentrations and isotope compositions, suggest that the Li signature of the two phases originated from the asteroidal reservoir. By assuming that Ol^{FeO} and Pl were equilibrated with the fluid, we can estimate the Li concentration of the fluid reservoir. Although Allende a experienced peak metamorphic temperature of ∼ 550-600°C, aqueous/hydrothermal alteration occurred at a lower temperature (<300°C) (Krot et al., 1998). Caciagli et al. (2011) examined Li-partitioning between olivine and hydrous fluid, and plagioclase and hydrous fluid at 800–1000°C, which increases with decreasing temperature and plagioclase An-content. Using their partition coefficients for olivine and fluid 210^{+720}_{-160}, and for plagioclase ($An_{82}Ab_{18}$) and fluid $5.2^{+4.7}_{-2.5}$, both at 300°C, we estimate the Li concentration of the fluid reservoir to be [Li] ∼ 1^{+3}_{-1} ng $\cdot g^{-1}$ and ∼ 8^{+7}_{-4} ng $\cdot g^{-1}$, which was calculated from a current [Li] of Ol^{FeO} ($0.2\ \mu g \cdot g^{-1}$) and Pl ($0.04\ \mu g \cdot g^{-1}$).

Asteroidal processes altered the concentrations and isotope compositions of mineral phases toward equilibrium. Once equilibrated, the Li concentrations and isotope compositions of a specific mineral would be identical regardless of its origin. However, a significant difference in Li distribution is observed between Ol and Ol^{irim} and LPx and LPx^{irim}, of different origins. This observation precludes Li equilibrium in olivine and low-Ca pyroxene during asteroidal processing, even though alteration and metamorphism were significant on the Allende parent body (Krot et al., 1998).

We examined Li behavior in group 1 olivines. The area of [Li]-and-δ^7Li clusters in Figure 5b becomes smaller in the order of $Ol_{Fo>95}$, $Ol_{Fo<95}$, and Ol^{irim}, with constant averages of δ^7Li. In Figure 6a, δ^7Li is shown as a function of Fa content. Variation of δ^7Li becomes smaller as Fe content increases, which suggests that the Li-isotope composition was moving towards equilibrium values as the Fe/Mg ratio increased. Bell et al.

(2008) also reported that variation of δ^7Li is less in fayalitic olivines than in forsteritic olivines from Allende chondrules.

The ranges in the Fe/Mg ratio of group 2 and 3 olivines (from Fo_{81} to Fo_{100}, and from Fo_{77} to Fo_{98}) are similar to that of group 1 olivines (from Fo_{78} to Fo_{99}). However, the trend, in which Li-isotope composition reaches equilibrium as the Fe/Mg ratio increases, is not observed in either group 2 or 3 olivines. If the Li-isotope equilibration observed for group 1 olivines occurred during asteroidal alteration, the Li-isotope compositions of group 2 and 3 olivines should have reached equilibrium as well. The Li-isotope composition could approach equilibrium through solid-state diffusion on the asteroid. Average Li concentration of Ol is higher than that of Ol^{FeO}. Therefore, Li of Ol was not equilibrated in the asteroidal environment. Since diffusion velocity of ^{6}Li is faster than ^{7}Li, alteration by asteroidal processes should give a negative-correlation between Li concentrations and isotope compositions. We do not see such a correlation and thus infer that modification of Li in olivines by a diffusion process was insignificant. Since Ol^{irim} of group 1 contains the highest Fe/Mg ratio and its δ^7Li is the most equilibrated (Fig. 5a), the Li-isotope equilibration of group 1 olivines must have taken place during igneous-rim formation.

4.2.2 Effects of igneous processes in the solar nebula

We find heavy Li (δ^7Li$\sim$ +40‰) in both Ol and LPx in group 1 chondrules (Fig. 4a). Since the diffusion velocity of Li is faster than O both in solid materials and melt (Lowry et al., 1981; Wendlandt, 1991; Dohmen et al., 2002; Parkinson et al., 2007; Dohmen et al., 2010), the Li isotopes of the melt must have been homogenized at the same time as the O isotopes. The variation of δ^7Li in Ol of group 1 should have been obtained after homogenization of the melt. Since the isotope fractionation between silicate and melt within the temperature range of chondrule formation is negligible, devolatilization is the only process that can give rise to the variation in isotope composition in the melt. In case of an evaporative loss of Li, the Li remaining in the melt would be enriched in the heavy isotope (Chaussidon and Robert, 1998). A variation of Li-isotope composition by $\sim$ 50‰ is observed in $Ol_{Fo>95}$, which is the least Li altered phase during igneous-rim formation. Since devolatilization makes the melt heavier and the lightest Li-isotope composition of $Ol_{Fo>95}$ in group is δ^7Li ~ -10‰, we infer the Li-isotope composition of the melt during homogenization of the O-isotope composition should have been δ^7Li ~ -10‰. We propose that the Li-isotope composition of the melt evolved from δ^7Li$\sim$ -10‰ to +40‰.

The abundance of Na remained relatively constant during chondrule formation (Alexander et al., 2008). Prevention of the evaporation of Na may require that chondrules formed in regions with high dust/gas ratios (Alexander et al., 2008). Fractionation of K isotopes could have been avoided by gas-melt isotope exchange during chondrule formation, if the K-vapor pressure was significantly high (Alexander et al., 2000). Since

Li is a trace element, pressure of Li-vapor was not as high as those of Na-vapor and K-vapor. If the Li-isotope fractionation observed by this study contributed to Rayleigh-type evaporation, >90% of Li in chondrule melt would have been transported into gas, with an isotope fractionation factor $\alpha = (^7\mathrm{Li}/^6\mathrm{Li})_{\mathrm{vapor}}/(^7\mathrm{Li}/^6\mathrm{Li})_{\mathrm{melt}} \sim 0.993$ (Kasemann et al., 2005).

The melt on LPx formation had different O and Li isotopes relative to the early melt. An obvious negative-correlation between concentration and isotope composition is not observed in $\mathrm{Ol}_{\mathrm{Fo>95}}$ (Figs. 4a-c, 5b). However, we infer that the variation in δ^7Li of the melt, produced by devolatilization, is maintained in or recorded by the olivines, but the gas-melt Li-isotope exchange during igneous rim formation obscured the negative-correlation.

The variation in both Li-isotope composition and Fe/Mg ratios in group 1 olivine and the preservation of variation in Li-isotope composition, but modification of Fe/Mg ratio in group 2 and 3 olivines, is consistent with the conclusion of Parkinson et al. (2007). They state that diffuses 4–8 times slower than Fe-Mg in olivine and together with our findings contradicts the report by Dohmen et al. (2010), which reports that Li diffuses 10^{5-7} times faster than Fe-Mg in olivine at 800°C.

Low-Ca pyroxenes are the most Li-enriched phases identified in our study (Figs. 5b,d,f). The LPx of group 1 chondrules (Fig. 5b) demonstrates a significant range of [Li] and δ^7Li between two components (0.4 μg·g^{-1}, +33‰ for component 1 and 3 μg·g^{-1}, −33‰ for component 2). $\mathrm{LPx}^{\mathrm{irim}}$ forms a cluster with an average [Li] of 7 μg · g^{-1} and δ^7Li of −11‰. The existence of the array of LPx and the cluster of $\mathrm{LPx}^{\mathrm{irim}}$ is also observed on group 2 (Fig. 5d).

The partition coefficients for Li between olivine and the melt and between low-Ca pyroxenes and melt are estimated to be from 0.01 to 1.04, and 0.13 to 0.22, respectively, at 0.1–3000 MPa and 1320–1390°C (Tomascak et al., 2016). Using these values, the partition coefficient for Li (k_{Li}) between olivine and low-Ca pyroxene is estimated as being 0.1 to 5. From the observations of this study we find the [Li] of $\mathrm{Ol}^{\mathrm{irim}}$ and $\mathrm{LPx}^{\mathrm{irim}}$ to be 0.2 and 7 μg · g^{-1}, respectively. The enrichment of Li in $\mathrm{LPx}^{\mathrm{irim}}$ goes against element partitioning under an equilibrium condition during asteroidal processing. The high [Li] and low δ^7Li observed in $\mathrm{LPx}^{\mathrm{irim}}$ from both group 1 and group 2 ([Li] and $\delta^7\mathrm{Li} = 7$ μg · g^{-1} and −11‰, respectively) should reflect those of the melt during igneous-rim formation. The Li-isotope composition of the final melt on igneous-rim formation ($\delta^7\mathrm{Li} \sim -11$‰) is coincidentally consistent with that of the initial chondrule melt ($\delta^7\mathrm{Li} \sim -10$‰) estimated from group 1 olivines. Evaporation of Li from chondrule melt and recondensation of Li to the final melt could explain the reprise of the isotope composition. However, the igneous rim is characterized by high abundances of not only alkalines, but also Si relative to the main region of the chondrules (Rubin and Wasson, 1987). Krot et al. (2004) suggested that igneous rims formed by either gas-solid condensation of silica-normative materials onto chondrule surfaces and subsequent in-

complete melting, or by direct condensation of gas, enriched in alkalines and SiO. Thus the enrichment of Li in LPx^{irim} resulted from a gaseous reservoir that may not be genetically related with the chondrule melt. The Li-isotope composition of the gaseous reservoir is estimated to be δ^7Li$\sim -11‰$. During chondrule formation the δ^7Li of LPx was approaching the Li-isotope composition of the gaseous reservoir, indicating that the chondrule melt interacted with the gaseous reservoir during chondrule formation.

4.2.3 Li-isotope distribution within chondrule groups

Ol^{irim} of group 1 is depleted in Li (Fig. 6a) and surrounded by LPx^{irim} enriched in Li. Li-isotope compositions were equilibrated among Ol^{irim} but Li concentrations between Ol^{irim} and LPx^{irim} were out of equilibration, as mentioned previously. These observations, together with O-isotope composition and the anhedral shape of Ol^{irim}, suggest that Li was diffusing out from Ol^{irim}, as the size of Ol^{irim} was becoming smaller. The duration, of igneous-rim formation for group 1, was sufficiently long to allow equilibration of Li isotopes, but not O isotopes.

For group 2, it is not obvious if Li isotopes of Ol were reaching equilibrium during igneous-rim formation (Fig. 6b), because of the lack of analyses in Ol^{irim}. Further analyses are required.

The Li of LPx^{irim} in group 3 chondrules differs to that in group 1 and 2 (Fig. 5f). The concentration of LPx^{irim} Li is low, but its isotope composition is consistent, when compared to whole rock values. Perhaps the Li concentration and isotope composition of the gas during igneous-rim formation differs from those of group 1 and group 2. Ol^{irim} tends to have a higher Fe/Mg ratio relative to that of Ol, thus the Fe/Mg ratios of olivine could have been modified during igneous-rim formation. However, both Ol and Ol^{irim} maintain Li-isotope variation. We conclude that unlike the igneous-rim formation process of group 1 chondrules, the igneous-rim formation process of group 3 did not equilibrate Li isotopes. We do not find pure galactic cosmic ray components with ^{7}Li/^{6}Li$\sim$ 2 that corresponds to δ^7Li$\sim -800‰$ (Read and Viola, 1984; Ramaty et al., 1996; Meneguzzi et al., 1971) in group 3 olivines. Therefore, group 3 olivines do not maintain the Li-isotope signature of the interstellar medium, from before the formation of the solar nebula, although they do maintain the O-isotope variation inherited from precursors.

4.3. Li isotope compositions of chondrule precursors

Considering that chondrules experienced multiple heating events (e.g., Jones et al., 2005) and asteroidal alteration, the ^{7}Li/^{6}Li heterogeneity could be caused by high temperature fractional crystallization, devolatilization, and diffusion (Tomascak et al., 2016). Although Chaussidon and Robert (1998) assumed the isotope heterogeneities observed in ordinary chondrite chondrules were inherited only from precursors, our combined O-

and Li-isotope study of the Allende chondrules can distinguish between the Li-isotope heterogeneity produced before, during and after chondrule formation.

Group 3 chondrules contain relict olivines which are overgrown by olivine, which crystallized from chondrule melts and their range of O-isotope compositions is inherited from precursors. Also group 3 olivines maintain variations in Li isotopes of the precursors that formed prior to chondrule formation and igneous-rim formation. Since the number of analyses for chondrule PO-3n is limited (Fig. 4i), we focus on group 3 chondrule PO-8 that preserves significant variation of both O- and Li-isotope compositions. The δ^7Li as a function of Δ^{17}O for group 3 chondrule PO-8 is shown in Figure 7. Olivines in group 3 chondrule PO-8 have different Δ^{17}O and δ^7Li values, which reflects either distinct relicts or melt. We see that variation of δ^7Li differs depending on values of Δ^{17}O. The Li-isotope composition varies from δ^7Li -23‰ to -3‰ with an O-isotope composition close to that of refractory inclusions ($-25 < \Delta^{17}\mathrm{O} < -20$‰) and is relatively constant (-8 ± 4‰), when the O-isotope composition is in between Δ^{17}O -20‰ and -5‰. Note that average Li-isotope compositions of group 3 olivines ($\delta^7\mathrm{Li} \sim -8$‰) is consistent with that of the chondrule melt ($\delta^7\mathrm{Li} \sim -10$‰) estimated from group 1 olivines. We infer that even with a constant Δ^{17}O ($-25 < \Delta^{17}\mathrm{O} < -20$‰), δ^7Li is distributed heterogeneously, probably reflecting kinetic processes.

We evaluate if it is possible that the heterogeneities of Δ^{17}O and δ^7Li resulted from measurements of ^{16}O-rich relict-olivine and ^{16}O-poor olivine with overgrowths, which the probe overlapped. Depending on the relative fraction of the two domains, the array of δ^{18}O/δ^{17}O on a three O-isotope diagram could be produced. If this is the case, the Li-isotope composition of ^{16}O-rich relict olivine is estimated to be δ^7Li -23‰. Chaussidon et al. (2006) analyzed refractory inclusions that do not show evidence for post-melting redistribution of Li and estimated δ^7Li to be -24 ± 46‰. The average of δ^7Li values of refractory inclusions is consistent with the relict olivine end component. If the variation of Δ^{17}O is dominated by a relative fraction of relict olivine and olivine with overgrowths on probing, we would expect to see mixing between δ^7Li of the end components (-23‰) and δ^7Li of the chondrule melt (-10‰; estimated from group 1 olivines). However, we see no monotonic correlation in Δ^{17}O-δ^7Li space (Fig. 7). We suggest that the variations of Δ^{17}O and δ^7Li are not dominated by probing and they reflect distinct relicts or melt having different O- and Li-isotope compositions either changing with time or having local heterogeneity.

Chaussidon and Robert (1998) reported Li-isotope variation preserved in ordinary chondrite chondrules ($-12.7 < \delta^7\mathrm{Li} < 34.5$‰) and proposed that the variation is inherited from chondrule precursors that preserved signatures resulting from the mixing of two different nucleosynthetic sources (galactic cosmic rays and big-bang nucleosynthesis). The variation is consistent with the range observed in group 1 olivines (from δ^7Li -10 to $+40$‰) and could result from the chondrule formation process. The lack of δ^7Li values below -10‰ in ordinary chondrite chondrules can be explained because or-

dinary chondrite chondrules do not have the ^{16}O-rich signature of refractory inclusions (Kita et al., 2010).

We conclude that the δ^7Li values of olivine, which formed prior to the asteroid, reflect a combination of: (1) variation of δ^7Li from -23 to -3‰ inherited from precursors with O-isotope composition of refractory inclusions ($-25 < \Delta^{17}\mathrm{O} < -20$‰), (2) relatively constant δ^7Li -8 ± 4‰ inherited from precursors with O isotopes in the rage $-20 < \Delta^{17}\mathrm{O} < -5$‰, (3) homogenization of δ^7Li in the melt during chondrule formation with δ^7Li~ -10‰, (4) modification of δ^7Li in the melt by devolatilization up to δ^7Li$\sim +40$‰, and (5) homogenization of δ^7Li during igneous-rim formation.

4.4. Lithium and oxygen reservoirs in the solar nebula

It has been suggested that gas-melt interactions played an important role during the formation of magnesium-rich chondrules. Libourel et al. (2006) inferred that typical type I chondrules are objects composed of an inherited igneous component (mainly forsteritic olivine with varying amounts of Fe,Ni-metal) and a second igneous component (low-Ca pyroxene, high-Ca pyroxene, and glass) formed through interaction with the nebula gas. Tissandier et al. (2002) demonstrated experimentally that partially molten chondrule-like samples exposed to gaseous SiO incorporate silica, inducing the crystallization of low-Ca pyroxene. These experiments suggest that various features observed in many type I chondrules, such as the presence of low-Ca pyroxene in the igneous rim of chondrules or the partial resorption of olivine, can be obtained by varying the duration or the temperature of the gas-melt interaction. High partial pressures of SiO (g) in the solar nebula have been invoked to explain the apparent enrichment of low-Ca pyroxene relative to olivine at the periphery of porphyritic chondrules.

Chaussidon et al. (2008) analyzed olivines and pyroxenes of CR and CV chondrules and estimated the O-isotope composition of the nebular gas to be $\Delta^{17}\mathrm{O}$ -0.1‰. It was inferred that the O-isotope compositions indicate that olivines in type I chondrules are relict grains that formed prior to the last chondrule formation. Chaussidon et al. (2008) also state that interaction between the gas and melt (forming pyroxenes) during chondrule formation was in an open system. Harju et al. (2014) observed a sub-‰ difference in δ^{29}Si between olivine and low-Ca pyroxene in CV and CR chondrules and concluded that the difference reflects Si isotopic condensation in the nebula under near-equilibrium conditions. Their model proposes that all olivines are relict, being either inherited from an earlier generation of igneous bodies, or from an earlier generation of chondrules, and that pyroxenes are produced by interaction of chondrule melt with the gas. In contrast, there are many chondrules in which it is clear that both olivine and pyroxene grew from the same melt during chondrule cooling, and Rudraswami et al. (2011), Ushikubo et al. (2012), and Tenner et al. (2013, 2015) have shown that there is no difference in O-isotope compositions between olivine and pyroxene in chondrules.

Our O- and Li-isotope observations suggest that olivines and low-Ca pyroxenes

formed from the same melt. Subsequently, low-Ca pyroxenes formed from the melt while interacting with a gaseous reservoir. The finding is inconsistent with the existence of a gaseous reservoir with a constant isotope composition during the period of chondrule formation. Rubin (2017) argued that the petrologic observation made on Semarkona is controversial for later stage gas-melt interaction and insisted that the formation of low-Ca pyroxene in the periphery region does not require gas-melt interaction. We predict that Li analyses of low-Ca pyroxenes in the periphery region will reveal the existence of gas-melt interaction during formation of ordinary chondrite chondrules.

We summarize Li reservoirs in the solar nebula inferred from this study (Fig. 8). Prior to chondrule formation, olivines with a different O-isotope composition were formed at different times or in different places. There were isotope reservoirs with δ^7Li that were varying from -23 to -3‰ and with the Δ^{17}O of refractory inclusions. During chondrule formation, the precursors were melted and O- and Li-isotope compositions were homogenized. Due to the high solidus temperature, olivine solidified first from the melt. Before low-Ca pyroxene crystallized, the O-isotope composition of the melt could have changed by a few ‰. Li-isotope composition of the melt changed from δ^7Li$\sim$ -10‰ to +40‰ by devolatilization. A portion of olivines and low-Ca pyroxene subsequently crystallized from isotopically heavy melt (δ^7Li$\sim$ +40‰). At the end of chondrule formation (during crystallization of low-Ca pyroxene), the Li-isotope composition of the melt changed drastically via interaction with a gaseous reservoir that was enriched in alkalines and Si with δ^7Li$\sim$ -11‰. Then on igneous-rim formation, low-Ca pyroxenes formed from melt that was enriched in Li. A mechanical mixture of objects with differing Li results in an asteroidal reservoir corresponding to whole rock Allende δ^7Li$\sim$ 2.4‰. After accumulation into the asteroid, plagioclase and a portion of olivine obtained O- and Li-isotope compositions reflecting the asteroidal reservoir.

We are now aware of existence of a distinct reservoir, as suggested by Seitz et al. (2007), with δ^7Li -11‰ in the early Solar system. Lithium-isotope compositions of chondrite, achondrite, lunar, and Martian meteorites obtained by whole-rock analyses range from δ^7Li -2 to 6‰ (Tomascak et al., 2016) and none of these can serve as the reservoir. It has been suggested that a primordial water reservoir existed in the early solar system (Sakamoto et al., 2007). Whilst the oxygen isotopic signatures identified by the current study are different from those of this theoretical reservoir, a similarly water rich reservoir could be the source of the Li-isotope composition predicted here. It is not clear if the reservoir still exists in the current Solar system.

5. CONCLUSIONS

We carried out 258 pairs of in situ O- and Li-isotope analyses for olivine, low-Ca pyroxene, high-Ca pyroxene, and plagioclase from the main bodies of type IAllende (CV3) chondrules and their igneous rims. We suggest that the isotope compositions

of plagioclases and secondary ferroan olivine (Fo_{62}–Fo_{65})resulted from asteroidal processes. Their Li-isotope compositions are similar to that of whole-rock Allende. After excluding these olivines and plagioclases, by comparison of O, Li, and Fe/Mg, we suggest that the Li-isotope composition of most chondrules was modified during igneous-rim formation, but not significantly by asteroidal process.

By analyzing a chondrule, which lacks evidence of equilibration in both O- and Li-isotope compositions during the period of chondrule and igneous-rim formation, we demonstrate a correlation between $\Delta^{17}O$ and $\delta^{7}Li$ preserved in olivine. We found that $\delta^{7}Li$ varied from -23 to -3‰ for a given $\Delta^{17}O$ of refractory inclusions. Based on the Li-isotope composition of low-Ca pyroxene formed during chondrule formation and igneous-rim formation, we suggest that chondrule melt reacted with a gaseous reservoir with $\delta^{7}Li \sim -11$‰.

Li concentrations and isotope compositions of chondrules from the Allende chondrite resulted from the multiple layers of processing that the chondrules have undergone. The variation of Li-isotope compositions reflects (1) variation of $\delta^{7}Li$ from -23 to -3‰ inherited from precursors with the O-isotope composition of refractory inclusions ($-25 < \Delta^{17}O < -20$‰), (2) relatively constant $\delta^{7}Li$ -8 ± 4‰ inherited from precursors with O isotopes that range by $-20 < \Delta^{17}O < -5$‰, (3) homogenization of $\delta^{7}Li$ in the melt during chondrule formation with $\delta^{7}Li \sim -10$‰, (4) modification of $\delta^{7}Li$ in the melt by devolatilization up to $\delta^{7}Li \sim +40$‰, and (5) homogenization of $\delta^{7}Li$ during igneous-rim formation.

6. ACKNOWLEDGMENT

We thank Y. Shimaki for technical support of the SIMS. We thank G. E. Bebout, C. Potiszil, A. E. Rubin, K. Kobayashi, R. Tanaka, and H. Kitagawa for useful discussions. We thank A. Krot, K. Nagashima, H.-M. Seitz, and the two anonymous reviewers for their constructive comments. We also thank M. Yamanaka, Y. Yachi and C. Sakaguchi, for technical support. We are greatly indebted to K. Tanaka, K. Anji, and Y. Shimizu and for their assistance maintaining the laboratory. This work was supported in part by Ministry of Education, Culture, Sports, Science and Technology (MEXT) of Japan.

References

Alexander, C. O., Grossman, J., Wang, J., Zanda, B., Bourot-Denise, M., and Hewins, R. (2000). The lack of potassium-isotopic fractionation in Bishunpur chondrules. *Meteorit. Planet. Sci.*, **35**(4), 859–868.

Alexander, C. O., Grossman, J. N., Ebel, D., and Ciesla, F. (2008). The formation conditions of chondrules and chondrites. *Science*, **320**(5883), 1617–1619.

Bell, D. R., Buseck, P. R., Channon, M. D., Hervig, R., Rieck, K. D., and Singletary, S. J. (2008). SIMS analysis of the isotopic composition of lithium in meteorites (abstract #2276). In *39th Lunar and Planetary Science Conference, CD-ROM*.

Bell, D. R., Hervig, R. L., Buseck, P. R., and Aulbach, S. (2009). Lithium isotope analysis of olivine by SIMS: Calibration of a matrix effect and application to magmatic phenocrysts. *Chem. Geol.*, **258**, 5–16.

Brearley, A. (2014). Nebular versus parent body processing. In H. D. Holland and K. K. Turekian (Eds.), *Treatise on Geochemistry* (pp. 309–334). Elsevier, Oxford, second edition.

Brenan, J. M., Ryerson, F. J., and Shaw, H. F. (1998). The role of aqueous fluids in the slab-to-mantle transfer of boron, beryllium, and lithium during subduction: Experiments and models. *Geochim. Cosmochim. Acta*, **62**, 3337–3347.

Caciagli, N., Brenan, J., McDonough, W., and Phinney, D. (2011). Mineral–fluid partitioning of lithium and implications for slab–mantle interaction. *Chem. Geol.*, **280**(3), 384–398.

Chaussidon, M., Libourel, G., and Krot, A. N. (2008). Oxygen isotopic constraints on the origin of magnesian chondrules and on the gaseous reservoirs in the early solar system. *Geochim. Cosmochim. Acta*, **72**(7), 1924–1938.

Chaussidon, M. and Robert, F. (1998). ^{7}Li/^{6}Li and ^{11}B/^{10}B variations in chondrules from Semarkona unequilibrated chondrite. *Earth Planet. Sci. Lett.*, **164**, 577–589.

Chaussidon, M., Robert, F., and McKeegan, K. D. (2006). Li and B isotopic variations in an Allende CAI: Evidence for the in situ decay of short-lived ^{10}Be and for the possible presence of the short-lived nuclide ^{7}Be in the early solar system. *Geochim. Cosmochim. Acta*, **70**, 224–245.

Clayton, R. N. (1981). Isotopic variations in primitive meteorites. *Philosophical Transactions of the Royal Society of London A: Mathematical, Physical and Engineering Sciences*, **303**(1477), 339–349.

712 Clayton, R. N. (1993). Oxygen isotopes in meteorites. *Annu. Rev. Earth Planet. Sci.*,
713 **21**, 115–149.

714 Clayton, R. N. and Mayeda, T. K. (1999). Oxygen isotope studies of carbonaceous
715 chondrites. *Geochim. Cosmochim. Acta*, **63**(13-14), 2089–2104.

716 Cole, D. R. and Chakraborty, S. (2001). Rates and mechanisms of isotopic exchange.
717 *Reviews in Mineralogy and Geochemistry*, **43**(1), 83–223.

718 Dohmen, R., Chakraborty, S., and Becker, H. W. (2002). Si and O diffusion in olivine
719 and implications for characterizing plastic flow in the mantle. *Geophys Res. Lett.*,
720 **29**(21), 261–264.

721 Dohmen, R., Kasemann, S. A., Coogan, L., and Chakraborty, S. (2010). Diffusion of
722 Li in olivine. Part I: Experimental observations and a multi species diffusion model.
723 *Geochim. Cosmochim. Acta*, **74**(1), 274–292.

724 Eiler, J., Graham, C., and Valley, J. (1997). SIMS analysis of oxygen isotopes: Matrix
725 effects in complex minerals and glasses. *Chem. Geol.*, **138**(3-4), 221–244.

726 Grossman, J. N. (1988). Formation of chondrules. In J. F. Kerridge and M. S. Matthews
727 (Eds.), *Meteorites and the Early Solar System* (pp. 680–696). University of Arizona
728 Press, Tucson.

729 Gurenko, A. A. and Chaussidon, M. (2002). Oxygen isotope variations in primitive
730 tholeiites of Iceland: evidence from a SIMS study of glass inclusions, olivine phe-
731 nocrysts and pillow rim glasses. *Earth Planet. Sci. Lett.*, **205**(1), 63–79.

732 Gurenko, A. A., Chaussidon, M., and Schmincke, H.-U. (2001). Magma ascent and
733 contamination beneath one intraplate volcano: evidence from S and O isotopes in
734 glass inclusions and their host clinopyroxenes from miocene basaltic hyaloclastites
735 southwest of Gran Canaria (Canary Islands). *Geochim. Cosmochim. Acta*, **65**(23),
736 4359–4374.

737 Hanon, P., Chaussidon, M., and Robert, F. (1999). Distribution of lithium, beryllium,
738 and boron in meteoritic chondrules. *Meteorit. Planet. Sci.*, **34**, 247–258.

739 Harju, E. R., Kohl, I. E., Rubin, A. E., and Young, E. D. (2014). Evaluating Silicon
740 condensation in type 1AB chondrules using in-situ silicon isotopes (abstract #2829).
741 In *45th Lunar and Planetary Science Conference, CD-ROM*.

742 Hervig, R. L., Williams, P., Thomas, R. M., Schauer, S. N., and Steele, I. M. (1992).
743 Microanalysis of oxygen isotopes in insulators by secondary ion mass spectrometry.
744 *International Journal of Mass Spectrometry and Ion Processes*, **120**(1-2), 45–63.

Hewins, R. H. (1997). Chondrules. *Annu. Rev. Earth Planet. Sci.*, **25**(1), 61–83.

Imai, H. and Yurimoto, H. (2003). Oxygen isotopic distribution in an amoeboid olivine aggregate from the Allende CV chondrite: Primary and secondary processes. *Geochim. Cosmochim. Acta*, **67**(4), 765–772.

Isa, J., Kohl, I., Liu, M.-C., Wasson, J., Young, E., and McKeegan, K. (2017). Quantification of oxygen isotope SIMS matrix effects in olivine samples: Correlation with sputter rate. *Chem. Geol.*, **458**, 14–21.

Jones, R. H. (1990). Petrology and mineralogy of type II, FeO-rich chondrules in Semarkona (LL3.0): Origin by closed-system fractional crystallization, with evidence for supercooling. *Geochim. Cosmochim. Acta*, **54**(6), 1785–1802.

Jones, R. H. (1994). Petrology of FeO-poor, porphyritic pyroxene chondrules in the Semarkona chondrite. *Geochim. Cosmochim. Acta*, **58**(23), 5325–5340.

Jones, R. H. (1996a). relict grains in chondrules: Evidence for chondrule recycling. In R. H. Hewins, R. H. Jones, and E. R. D. Scott (Eds.), *Chondrules and the protoplanetary disk* (pp. 163–172). Cambridge University Press, Cambridge.

Jones, R. H. (1996b). FeO-rich, porphyritic pyroxene chondrules in unequilibrated ordinary chondrites. *Geochim. Cosmochim. Acta*, **60**(16), 3115–3138.

Jones, R. H., Grossman, J. N., and Rubin, A. E. (2005). Chemical, mineralogical and isotopic properties of chondrules: Clues to their origin. In A. N. Krot, E. R. D. Scott, and B. Reipurth (Eds.), *Chondrites and the protoplanetary disk*, volume 341 (pp. 251–285). Astronomical Society of the Pacific, San Francisco.

Jones, R. H., Leshin, L. A., Guan, Y., Sharp, Z. D., Durakiewicz, T., and Schilk, A. J. (2004). Oxygen isotope heterogeneity in chondrules from the Mokoia CV3 carbonaceous chondrite. *Geochim. Cosmochim. Acta*, **68**(16), 3423–3438.

Jones, R. H., Saxton, J. M., Lyon, I. C., and Turner, G. (2000). Oxygen isotopes in chondrule olivine and isolated olivine grains from the CO3 chondrite Allan Hills A77307. *Meteorit. Planet. Sci.*, **35**(4), 849–857.

Kasemann, S. A., Jeffcoate, A. B., and Elliott, T. (2005). Lithium isotope composition of basalt glass reference material. *Analytical Chemistry*, **77**(16), 5251–5257.

Kimura, M., Grossman, J., and Weisberg, M. (2008). Fe-Ni metal in primitive chondrites: Indicators of classification and metamorphic conditions for ordinary and CO chondrites. *Meteorit. Planet. Sci.*, **43**(7), 1161–1177.

Kita, N., Nagahara, H., Tachibana, S., Tomomura, S., Spicuzza, M., Fournelle, J., and Valley, J. (2010). High precision SIMS oxygen three isotope study of chondrules in LL3 chondrites: Role of ambient gas during chondrule formation. *Geochim. Cosmochim. Acta*, **74**(22), 6610–6635.

Krot, A. N., Libourel, G., Goodrich, C. A., and Petaev, M. I. (2004). Silica-rich igneous rims around magnesian chondrules in CR carbonaceous chondrites: Evidence for condensation origin from fractionated nebular gas. *Meteorit. Planet. Sci.*, **39**(12), 1931–1955.

Krot, A. N., Petaev, M. I., Scott, E. R. D., Choi, B. G., Zolensky, M. E., and Keil, K. (1998). Progressive alteration in CV3 chondrites: More evidence for asteroidal alteration. *Meteorit. Planet. Sci.*, **33**, 1065–1085.

Krot, A. N., Scott, E. R. D., and Zolensky, M. E. (1995). Mineralogical and chemical modification of components in CV3 chondrites: Nebular or asteroidal processing? *Meteoritics*, **30**, 748–775.

Krot, A. N. and Wasson, J. T. (1995). Igneous rims on low-FeO and high-FeO chondrules in ordinary chondrites. *Geochim. Cosmochim. Acta*, **59**(23), 4951–4966.

Leshin, L. A., Rubin, A. E., and McKeegan, K. D. (1997). The oxygen isotopic composition of olivine and pyroxene from CI chondrites. *Geochim. Cosmochim. Acta*, **61**(4), 835–845.

Libourel, G., Krot, A. N., and Tissandier, L. (2006). Role of gas-melt interaction during chondrule formation. *Earth Planet. Sci. Lett.*, **251**(3), 232–240.

Lowry, R. K., Reed, S. J. B., Nolan, J., Henderson, P., and Long, J. V. P. (1981). Lithium tracer-diffusion in an alkali-basaltic melt – An ion-microprobe determination. *Earth Planet. Sci. Lett.*, **53**, 36–40.

Maruyama, S., Watanabe, M., Kunihiro, T., and Nakamura, E. (2009). Elemental and isotopic abundances of lithium in chondrule constituents in the Allende meteorite. *Geochim. Cosmochim. Acta*, **73**(3), 778–793.

McDonough, W. F., Teng, F. Z., Tomascak, P. B., Ash, J. N., Grossman, J. N., and Rudnick, R. L. (2003). Lithium isotopic composition of chondritic meteorites (abstract #1931). In *34th Lunar and Planetary Science Conference, CD-ROM*.

Meneguzzi, M., Audouze, J., and Reeves, H. (1971). Petrographic variations among carbonaceous chondrites of the Vigarano type. *Astron. Astrophys.*, **15**, 337–359.

809 Parkinson, I. J., Hammond, S. J., James, R. H., and Rogers, N. W. (2007). High-
810 temperature lithium isotope fractionation: insights from lithium isotope diffusion in
811 magmatic systems. *Earth Planet. Sci. Lett.*, **257**(3), 609–621.

812 Ramaty, R., Kozlovski, B., and Lingenfelter, R. E. (1996). Light isotopes, extinct ra-
813 dioisotopes, and gamma-ray lines from low-energy cosmic-ray interactions. *Astro-*
814 *phys. J.*, **456**, 525–540.

815 Read, S. M. and Viola, V. E. (1984). Excitation functions for A $\geq$ 6 fragments formed
816 in ^{1}H- and ^{4}He- induced reactions on light nuclei. *Atomic Data and Nuclear Data*
817 *Tables*, **31**, 359–385.

818 Rubin, A. E. (1984). Coarse-grained chondrule rims in type 3 chondrites. *Geochim.*
819 *Cosmochim. Acta*, **48**(9), 1779–1789.

820 Rubin, A. E. (1996). Multiple heating of chondrules. In R. H. Hewins, R. H. Jones,
821 and E. R. D. Scott (Eds.), *Chondrules and the protoplanetary disk* (pp. 173–179).
822 Cambridge University Press, Cambridge.

823 Rubin, A. E. (2017). Type-IAB chondrules in LL3.0 Semarkona: no need for high
824 partial pressures of SiO(g) in the Solar nebula (abstract #2700). In *48th Lunar and*
825 *Planetary Science Conference, CD-ROM*.

826 Rubin, A. E. and Wasson, J. T. (1987). Chondrules, matrix and coarse-grained chon-
827 drule rims in the Allende meteorite: Origin, interrelationships and possible precursor
828 components. *Geochim. Cosmochim. Acta*, **51**(7), 1923–1937.

829 Rubin, A. E., Wasson, J. T., Clayton, R. N., and Mayeda, T. K. (1990). Oxygen isotopes
830 in chondrules and coarse-grained chondrule rims from the Allende meteorite. *Earth*
831 *Planet. Sci. Lett.*, **96**(3), 247–255.

832 Rudraswami, N., Ushikubo, T., Nakashima, D., and Kita, N. (2011). Oxygen isotope
833 systematics of chondrules in the Allende CV3 chondrite: High precision ion micro-
834 probe studies. *Geochim. Cosmochim. Acta*, **75**(23), 7596–7611.

835 Ryerson, F. and McKeegan, K. D. (1994). Determination of oxygen self-diffusion in
836 åkermanite, anorthite, diopside, and spinel: Implications for oxygen isotopic anoma-
837 lies and the thermal histories of Ca-Al-rich inclusions. *Geochim. Cosmochim. Acta*,
838 **58**(17), 3713–3734.

839 Sakamoto, N., Seto, Y., Itoh, S., Kuramoto, K., Fujino, K., Nagashima, K., Krot, A. N.,
840 and Yurimoto, H. (2007). Remnants of the early solar system water enriched in heavy
841 oxygen isotopes. *Science*, **317**(5835), 231–233.

Scott, E. and Krot, A. (2014). Chondrites and their components. In H. D. Holland and K. K. Turekian (Eds.), *Treatise on Geochemistry* (pp. 143–200). Elsevier, Oxford, second edition.

Seitz, H.-M., Brey, G. P., Zipfel, J., Ott, U., Weyer, S., Durali, S., and Weinbruch, S. (2007). Lithium isotope composition of ordinary and carbonaceous chondrites, and differentiated planetary bodies: Bulk solar system and solar reservoirs. *Earth Planet. Sci. Lett.*, **260**(3–4), 582–596.

Seitz, H.-M., Zipfel, J., Brey, G. P., and Ott, U. (2012). Lithium isotope compositions of chondrules, CAI and a dark inclusion from Allende and ordinary chondrites. *Earth Planet. Sci. Lett.*, **329**, 51–59.

Tenner, T. J., Nakashima, D., Ushikubo, T., Kita, N. T., and Weisberg, M. K. (2015). Oxygen isotope ratios of FeO-poor chondrules in CR3 chondrites: Influence of dust enrichment and H_2O during chondrule formation. *Geochim. Cosmochim. Acta*, **148**, 228–250.

Tenner, T. J., Ushikubo, T., Kurahashi, E., Kita, N. T., and Nagahara, H. (2013). Oxygen isotope systematics of chondrule phenocrysts from the CO3.0 chondrite Yamato 81020: Evidence for two distinct oxygen isotope reservoirs. *Geochim. Cosmochim. Acta*, **102**, 226–245.

Tissandier, L., Libourel, G., and Robert, F. (2002). Gas-melt interactions and their bearing on chondrule formation. *Meteorit. Planet. Sci.*, **37**(10), 1377–1389.

Tomascak, P. B., Magna, T., and Dohmen, R. (2016). *Advances in Lithium Isotope Geochemistry*. Springer, New York.

Ushikubo, T., Kimura, M., Kita, N. T., and Valley, J. W. (2012). Primordial oxygen isotope reservoirs of the solar nebula recorded in chondrules in Acfer 094 carbonaceous chondrite. *Geochim. Cosmochim. Acta*, **90**, 242–264.

Wendlandt, R. F. (1991). Oxygen diffusion in basalt and andesite melts - experimental results and discussion of chemical versus tracer diffusion. *Contrib. Mineral. Petrol.*, **108**(4), 463–471.

Young, E. D. and Russell, S. S. (1998). Oxygen reservoirs in the early solar nebula inferred from an Allende CAI. *Science*, **282**(5388), 452–455.

Zolensky, M. E., Krot, A. N., and Benedix, G. (2008). Record of low-temperature alteration in asteroids. *Reviews in Mineralogy and Geochemistry*, **68**(1), 429–462.

Table 1: Major-element compositions of chondrule constituents.

		phase	occurrence	n	compo*	[SiO_2]	[TiO]	[Al_2O_3]	[Cr_2O_3]	[FeO]	[MnO]	[MgO]	[CaO]	[Na_2O]	[K_2O]	[NiO]	[SO_3]	[P_2O_5]	[F]	[Cl]	total
group 1	BOP-2	$Ol_{>Fo95}$	inner BO	7	Fo_{99}	42.86	0.08	0.19	0.13	1.48	0.13	54.91	0.19	–	–	0.02	0.02	0.01	0.01	0.01	100.03
		$Ol_{>Fo95}$	shell of inner BO	34	Fo_{98}	42.62	0.08	0.26	0.24	2.00	0.10	54.55	0.21	0.01	–	0.02	0.01	0.02	0.01	–	100.12
		$Ol_{<Fo95}$	shell of inner BO	7	Fo_{93}	41.69	0.07	0.26	0.24	6.87	0.10	50.59	0.16	0.02	–	0.02	0.01	0.01	–	–	100.03
		$Ol_{>Fo95}$	inner BO	2	Fo_{98}	42.70	0.07	0.23	0.16	2.42	0.08	54.27	0.18	0.01	–	–	0.01	0.02	–	–	100.15
		$Ol_{>Fo95}$	shell of outer BOP	17	Fo_{97}	42.60	0.08	0.30	0.25	2.82	0.10	53.79	0.20	0.03	–	0.02	0.01	0.01	0.01	–	100.24
		$Ol_{<Fo95}$	shell of outer BOP	1	Fo_{95}	42.13	0.05	0.26	0.20	5.28	0.06	51.99	0.17	–	–	0.03	0.02	–	–	–	100.20
		Ol^{irim}	igneous rim	2	Fo_{91}	41.29	0.03	0.17	0.08	8.78	0.04	49.21	0.15	0.01	–	0.01	0.01	–	0.01	–	99.77
		LPx	outer BOP	41	$En_{97}Wo_2$	59.14	0.26	1.63	0.50	0.41	0.07	37.40	1.11	0.01	0.01	0.02	0.02	0.02	0.01	–	100.61
		LPx^{irim}	igneous rim	7	$En_{98}Wo_1$	59.70	0.13	0.86	0.48	0.67	0.11	38.11	0.55	–	–	0.01	0.02	0.01	0.01	–	100.67
		HPx	outer BOP	6	$En_{68}Wo_{31}$	55.58	0.96	3.41	0.72	0.38	0.12	24.05	15.44	0.01	–	0.01	0.02	–	0.02	–	100.72
		Pl	outer BOP	10	$An_{82}Ab_{18}$	48.70	0.05	30.86	0.04	0.45	0.03	1.58	16.45	2.00	–	0.02	0.01	–	0.03	–	100.21
	PO-6	$Ol_{>Fo95}$	main	2	Fo_{99}	42.99	0.09	0.35	0.24	1.35	0.02	54.51	0.41	–	–	–	–	–	–	–	99.97
		$Ol_{<Fo95}$	main	4	Fo_{89}	40.98	0.05	0.26	0.20	10.62	0.15	47.38	0.22	0.01	0.01	0.06	0.02	0.06	–	–	100.00
		Ol^{irim}	igneous rim	3	Fo_{84}	40.42	0.02	0.14	0.06	14.45	0.18	44.19	0.16	–	–	0.07	0.01	0.03	–	–	99.74
		Ol^{FeO}	main	2	Fo_{64}	37.11	0.01	1.26	0.40	29.61	0.19	29.19	0.16	0.09	0.01	0.05	0.09	0.08	0.01	–	98.26
		LPx^{irim}	igneous rim	12	$En_{97}Wo_1$	59.73	0.14	0.99	0.55	1.11	0.08	37.96	0.50	0.01	–	0.03	0.02	0.02	0.02	–	101.15
	BO-4	$Ol_{>Fo95}$	main	10	Fo_{98}	43.10	0.05	0.23	0.24	1.98	0.06	54.43	0.26	0.02	–	0.03	–	0.02	0.01	–	100.44
		$Ol_{<Fo95}$	shell	3	Fo_{92}	41.95	0.04	0.20	0.26	7.50	0.10	49.73	0.13	0.01	0.01	0.03	0.01	0.02	0.01	–	99.99
group 2	PO-7	$Ol_{>Fo95}$	main	2	Fo_{98}	42.97	0.04	0.24	0.18	1.88	0.04	54.39	0.23	0.02	–	0.04	0.01	0.06	–	–	100.08
		$Ol_{<Fo95}$	main	1	Fo_{90}	41.33	–	0.14	0.07	9.94	0.05	47.65	0.20	–	0.01	–	–	–	0.04	–	99.41
		LPx^{irim}	igneous rim	3	$En_{98}Wo_1$	59.58	0.21	1.49	0.60	0.76	0.11	37.49	0.58	–	0.01	–	0.03	0.04	0.01	–	100.90
	PO-1	$Ol_{>Fo95}$	main	4	Fo_{99}	42.96	0.04	0.29	0.11	1.36	0.01	54.63	0.49	–	–	0.02	0.01	0.07	0.01	–	100.01
		$Ol_{<Fo95}$	main	1	Fo_{93}	41.06	0.07	0.23	0.16	6.61	0.08	50.31	0.45	0.01	–	0.07	0.01	–	0.03	–	99.07
		Ol^{FeO}	main	1	Fo_{65}	30.13	0.62	13.06	0.25	26.42	0.15	27.41	0.70	0.15	–	0.15	0.26	0.06	–	0.02	99.39
		LPx	main	3	$En_{93}Wo_5$	58.45	0.26	1.29	0.66	1.48	0.12	36.10	2.49	–	–	0.02	0.01	–	0.01	–	100.88
		HPx	main	3	$En_{56}Wo_{43}$	50.71	1.31	9.38	1.11	0.61	0.22	18.22	19.10	0.02	–	0.02	0.01	–	–	–	100.70
	PO-3c	$Ol_{<Fo95}$	main	3	Fo_{85}	40.33	0.04	0.22	0.16	14.05	0.10	45.01	0.23	0.01	–	0.03	0.01	0.04	–	–	100.23
		Ol^{FeO}	main	1	Fo_{62}	36.66	0.10	0.18	0.43	32.92	0.22	30.43	0.19	–	–	–	0.01	0.06	–	–	101.32
	PO-3s	$Ol_{>Fo95}$	main	2	Fo_{98}	43.04	0.03	0.26	0.20	2.02	0.04	54.70	0.45	–	–	0.05	0.01	–	–	0.01	100.76
		$Ol_{<Fo95}$	main	3	Fo_{91}	41.67	0.03	0.24	0.18	8.25	0.04	49.36	0.30	–	0.01	0.01	–	0.02	0.02	–	100.11
group 3	PO-8	$Ol_{<Fo95}$	core	3	Fo_{87}	40.85	0.02	0.29	0.28	12.26	0.10	45.57	0.38	0.01	–	0.12	0.03	–	–	–	99.90
		$Ol_{>Fo95}$	mantle	12	Fo_{96}	42.52	0.02	0.17	0.12	3.73	0.11	52.80	0.26	0.01	–	0.13	0.02	0.03	0.01	–	99.93
		$Ol_{<Fo95}$	mantle	22	Fo_{92}	41.93	0.02	0.19	0.09	7.47	0.10	49.90	0.27	0.01	–	0.04	0.02	0.03	0.01	–	100.07
		Ol^{irim}	igneous rim	10	Fo_{87}	41.09	0.02	0.22	0.05	12.21	0.11	45.89	0.27	–	–	0.05	0.01	0.03	0.01	–	99.96
		LPx^{irim}	igneous rim	2	$En_{93}Wo_6$	59.71	0.23	1.26	0.67	0.99	0.13	34.65	3.00	–	–	0.06	0.04	0.03	0.03	–	100.78
		HPx^{irim}	igneous rim	4	$En_{62}Wo_{37}$	54.82	0.79	4.00	0.83	0.72	0.13	21.72	17.92	0.01	–	0.03	0.02	0.01	0.02	–	101.02
		Pl	mantle	3	$An_{82}Ab_{18}$	48.33	0.04	30.78	0.04	1.29	0.01	0.79	16.63	2.01	0.01	0.03	0.01	–	–	–	99.97
	PO-3n	$Ol_{>Fo95}$	main	1	Fo_{95}	42.62	0.01	0.14	0.01	4.44	0.16	52.41	0.17	–	–	0.05	–	–	0.05	–	100.04
		$Ol_{<Fo95}$	main	4	Fo_{89}	41.45	0.02	0.14	0.05	10.28	0.10	47.50	0.19	–	–	0.04	0.01	0.01	0.02	0.01	99.77

Element concentration is expressed in wt%. Element concentration not available is denoted by —.
Abbreviation compo* denotes major-element composition and is defined by $\frac{\mathrm{Fo}}{100} \equiv \frac{\mathrm{Mg}}{\mathrm{Mg+Fe}}$, $\frac{\mathrm{En|Wo}}{100} \equiv \frac{\mathrm{Mg|Ca}}{\mathrm{Mg+Fe+Ca}}$, and $\frac{\mathrm{Ab|An}}{100} \equiv \frac{\mathrm{Na|Ca}}{\mathrm{Ca+Na+K}}$ in molar units.
Ol, LPx, and HPx are olivine, low-Ca pyroxene, and high-Ca pyroxene at the main chondrule (including mantle or core regions).
$Ol_{>Fo95}$ and $Ol_{<Fo95}$ are Ol with chemical composition $Fo_{>95}$ and $Fo_{65–95}$.
Ol^{irim}, LPx^{irim}, and HPx^{irim} are olivine, low-Ca pyroxene, and high-Ca pyroxene at igneous rims.
Pl is plagioclase and Ol^{FeO} is olivine with chemical composition $Fo_{\leq 65}$.

Table 2: O- and Li-isotope compositions of chondrule constituents.

		phase	occurrence	n	compo*	δ^{18}O	δ^{17}O	Δ^{17}O	δ^{7}Li	[Li]$^{\mu g \cdot g^{-1}}$
group 1	BOP-2	$Ol_{>Fo95}$	inner BO	7	$Fo_{99.0(4)}$	-5 (1)	-7.7 (7)	-5.4 (4)	22 (6)	0.5 (2)
		$Ol_{>Fo95}$	shell of inner BO	34	$Fo_{98(1)}$	-5.0 (8)	-7.9 (6)	-5.3 (5)	6 (4)	0.7 (4)
		$Ol_{<Fo95}$	shell of inner BO	7	$Fo_{93(3)}$	-4.8 (6)	-7.9 (5)	-5.4 (3)	7 (4)	0.8 (4)
		$Ol_{>Fo95}$	outer BOP	2	$Fo_{98(1)}$	-4.6 (2)	-7.9 (4)	-5.5 (3)	17 (14)	0.3 (1)
		$Ol_{>Fo95}$	shell of outer BOP	17	$Fo_{97(1)}$	-4.6 (9)	-7.7 (5)	-5.3 (4)	9 (4)	0.2 (2)
		$Ol_{<Fo95}$	shell of outer BOP	1	Fo_{95}	-6.0	-8.4	-5.2	-5	0.2
		Ol^{irim}	igneous rim	2	Fo_{91}	-4.8 (1)	-7.9 (3)	-5.4 (2)	5 (1)	0.2 (1)
		LPx	outer BOP	41	$En_{97(2)}Wo_{2(2)}$	-3.1 (7)	-7.0 (6)	-5.4 (4)	-4 (13)	3 (2)
		LPx^{irim}	igneous rim	7	$En_{98.0(3)}Wo_{1.0(2)}$	-3.1 (7)	-7.0 (6)	-5.4 (4)	-4 (5)	5.2 (4)
		HPx	outer BOP	6	$En_{68(6)}Wo_{31(6)}$	-2 (1)	-6.3 (9)	-5.1 (5)	-6 (6)	0.6 (3)
		Pl	outer BOP	10	$An_{82(1)}Ab_{18(1)}$	-2.5 (9)	-6.9 (9)	-5.6 (5)	1 (4)	0.0 (0)
	PO-6	$Ol_{>Fo95}$	main	2	$Fo_{99(1)}$	-6 (1)	-9 (2)	-6 (1)	-3 (7)	0.7 (3)
		$Ol_{<Fo95}$	main	4	$Fo_{89(3)}$	-4.2 (6)	-7.1 (3)	-5.0 (3)	5 (3)	0.2 (1)
		Ol^{irim}	igneous rim	3	$Fo_{84(6)}$	-4.4 (3)	-7.0 (4)	-4.7 (3)	6 (6)	0.1 (1)
		Ol^{FeO}	main	2	$Fo_{64(1)}$	4.8 (2)	0 (2)	-3 (1)	2 (2)	0.2 (2)
		LPx^{irim}	igneous rim	12	$En_{97(1)}Wo_{0.9(2)}$	-3.7 (6)	-7.0 (6)	-5.0 (3)	-15 (6)	8 (3)
	BO-4	$Ol_{>Fo95}$	main	10	$Fo_{98(1)}$	-4.4 (6)	-7.8 (7)	-5.5 (5)	11 (12)	0.1 (1)
		$Ol_{<Fo95}$	shell	3	$Fo_{92(2)}$	-4.8 (1)	-7.6 (3)	-5.1 (3)	9 (9)	0.3 (2)
group 2	PO-7	$Ol_{>Fo95}$	main	2	$Fo_{98.0(1)}$	-5.9 (4)	-9.2 (6)	-6.1 (4)	-7 (11)	1.1 (6)
		$Ol_{<Fo95}$	main	1	Fo_{90}	-6.3	-9.3	-6.0	10	0.2
		LPx^{irim}	igneous rim	3	$En_{98.0(2)}Wo_{1.1(2)}$	-5.7 (2)	-9.1 (5)	-6.2 (4)	-13 (3)	7.7 (9)
	PO-1	$Ol_{>Fo95}$	main	4	$Fo_{99(1)}$	-6.2 (7)	-9.9 (2)	-6.7 (3)	4 (12)	0.2 (2)
		$Ol_{<Fo95}$	main	1	Fo_{93}	-6.9	-9.3	-5.7	4	0.4
		Ol^{FeO}	main	1	Fo_{65}	5.8	0.84	-2.2	-2	0.1
		LPx	main	3	$En_{93(2)}Wo_{5(1)}$	-5.2 (3)	-9.1 (6)	-6.4 (5)	4 (13)	3 (1)
		HPx	main	3	$En_{56(2)}Wo_{43(2)}$	-6.4 (6)	-9.7 (2)	-6.4 (2)	5 (9)	0.4 (2)
	PO-3c	$Ol_{<Fo95}$	main	3	$Fo_{85(7)}$	-6.8 (8)	-9.8 (4)	-6.3 (4)	-6 (6)	0.1 (0)
		Ol^{FeO}	main	1	Fo_{62}	-2.7	-4.5	-3.1	5	0.0
	PO-3s	$Ol_{>Fo95}$	main	2	$Fo_{98(2)}$	-6.6 (3)	-9.7 (3)	-6.3 (2)	-11 (10)	0.4 (1)
		$Ol_{<Fo95}$	main	3	$Fo_{91(4)}$	-6.7 (5)	-9.2 (5)	-5.7 (4)	2 (7)	0.5 (2)
group 3	PO-8	$Ol_{<Fo95}$	core	3	$Fo_{87(5)}$	-17 (6)	-20 (6)	-11 (3)	-7 (1)	0.2 (1)
		$Ol_{>Fo95}$	mantle	12	$Fo_{96(1)}$	-28 (15)	-30 (14)	-15 (6)	-6 (5)	0.2 (1)
		$Ol_{<Fo95}$	mantle	22	$Fo_{92(2)}$	-34 (14)	-35 (13)	-18 (6)	-9 (4)	0.2 (2)
		Ol^{irim}	igneous rim	10	$Fo_{87(4)}$	-27 (18)	-29 (17)	-15 (8)	-12 (7)	0.3 (2)
		LPx^{irim}	igneous rim	2	$En_{93(1)}Wo_{6(1)}$	-2 (2)	-6 (1)	-5.5 (1)	-1 (3)	0.9 (5)
		HPx^{irim}	igneous rim	4	$En_{62(4)}Wo_{37(4)}$	-5.4 (4)	-8.1 (6)	-5.3 (6)	-9 (7)	0.2 (1)
		Pl	mantle	3	$An_{82(1)}Ab_{18(1)}$	3 (2)	-2 (1)	-3.3 (4)	-4 (6)	0.1 (0)
	PO-3n	$Ol_{>Fo95}$	main	1	Fo_{95}	-19	-21	-11	36	0.2
		$Ol_{<Fo95}$	main	4	$Fo_{89(8)}$	-18 (8)	-20 (8)	-11 (3)	5 (1)	0.1 (1)

Abbreviation compo* denotes major-element composition. Variation among n analyses (1SD) is shown in parenthesis.
Ol, LPx, and HPx are olivine, low-Ca pyroxene, and high-Ca pyroxene at the main chondrule (including mantle or core regions).
$Ol_{>Fo95}$ and $Ol_{<Fo95}$ are Ol with chemical composition $Fo_{>95}$ and Fo_{65-95}.
Ol^{irim}, LPx^{irim}, and HPx^{irim} are olivine, low-Ca pyroxene, and high-Ca pyroxene at igneous rims.
Pl is plagioclase and Ol^{FeO} is olivine with chemical composition $Fo_{\leq 65}$.

Table 3: Summary of O- and Li-isotope compositions of chondrule constituents.

	phase	n	compo*	δ^{18}O	δ^{17}O	Δ^{17}O	δ^{7}Li	[Li]$^{\mu g \cdot g^{-1}}$
group 1	$Ol_{>Fo95}$	72	$Fo_{98(1)}$	-4.8 (8)	-7.8 (6)	-5.4 (5)	9 (8)	0.5 (4)
	$Ol_{<Fo95}$	15	$Fo_{87(5)}$	-4.7 (7)	-7.7 (5)	-5.2 (3)	6 (6)	0.5 (4)
	Ol^{irim}	5	$Fo_{91(2)}$	-4.5 (3)	-7.3 (6)	-5.0 (4)	5 (4)	0.2 (1)
	LPx	41	$En_{97(4)}Wo_{2(4)}$	-3.1 (7)	-7.0 (6)	-5.4 (4)	-4 (13)	3 (2)
	LPx^{irim}	19	$En_{98(1)}Wo_{1(0)}$	-3 (1)	-6.7 (8)	-5.1 (4)	-11 (8)	7 (3)
	HPx	6	$En_{69(8)}Wo_{30(8)}$	-2.5 (9)	-6.9 (9)	-5.6 (5)	-6 (6)	0.6 (3)
	Pl	10	$An_{81(2)}Ab_{19(2)}$	5 (2)	-1 (1)	-3.3 (5)	1 (4)	0.04 (4)
	Ol^{FeO}	2	$Fo_{64(1)}$	4.8 (2)	0 (2)	-3 (1)	2 (2)	0.2 (2)
group 2	$Ol_{>Fo95}$	8	$Fo_{98(1)}$	-6.2 (6)	-9.7 (4)	-6.4 (4)	-3 (12)	0.5 (5)
	$Ol_{<Fo95}$	8	$Fo_{89(6)}$	-6.7 (5)	-9.5 (5)	-6.0 (4)	0 (7)	0.3 (2)
	LPx	3	$En_{94(1)}Wo_{5(1)}$	-5.2 (3)	-9.1 (6)	-6.4 (5)	4 (13)	3 (1)
	LPx^{irim}	3	$En_{99(1)}Wo_{1(1)}$	-5.7 (2)	-9.1 (5)	-6.2 (4)	-13 (3)	7.7 (9)
	HPx	3	$En_{53(4)}Wo_{46(4)}$	-6.4 (6)	-9.7 (2)	-6.4 (2)	5 (9)	0.4 (2)
	Ol^{FeO}	2	$Fo_{63(3)}$	2 (6)	-2 (4)	-2.6 (6)	1 (5)	0.08 (4)
group 3	$Ol_{>Fo95}$	13	$Fo_{96(1)}$	-27 (14)	-29 (13)	-15 (6)	-3 (12)	0.20 (7)
	$Ol_{<Fo95}$	29	$Fo_{91(4)}$	-30 (14)	-31 (14)	-16 (6)	-7 (6)	0.2 (2)
	Ol^{irim}	10	$Fo_{87(4)}$	-27 (18)	-29 (17)	-15 (8)	-12 (7)	0.3 (2)
	LPx^{irim}	2	$En_{93(0)}Wo_{6(1)}$	-2 (2)	-6 (1)	-5.5 (1)	-1 (3)	0.9 (5)
	HPx^{irim}	4	$En_{64(5)}Wo_{34(6)}$	-5.4 (4)	-8.1 (6)	-5.3 (6)	-9 (7)	0.20 (6)
	Pl	3	$An_{83(2)}Ab_{17(2)}$	3 (2)	-2 (1)	-3.3 (4)	-4 (6)	0.08 (4)

Abbreviation compo* denotes major-element composition. Variation within group (1SD) is shown in parenthesis.
Ol, LPx, and HPx are olivine, low-Ca pyroxene, and high-Ca pyroxene at the main chondrule (including mantle or core regions).
$Ol_{>Fo95}$ and $Ol_{<Fo95}$ are Ol with chemical composition $Fo_{>95}$ and Fo_{65-95}.
Ol^{irim}, LPx^{irim}, and HPx^{irim} are olivine, low-Ca pyroxene, and high-Ca pyroxene at igneous rims.
Pl is plagioclase and Ol^{FeO} is olivine with chemical composition $Fo_{\leq 65}$.

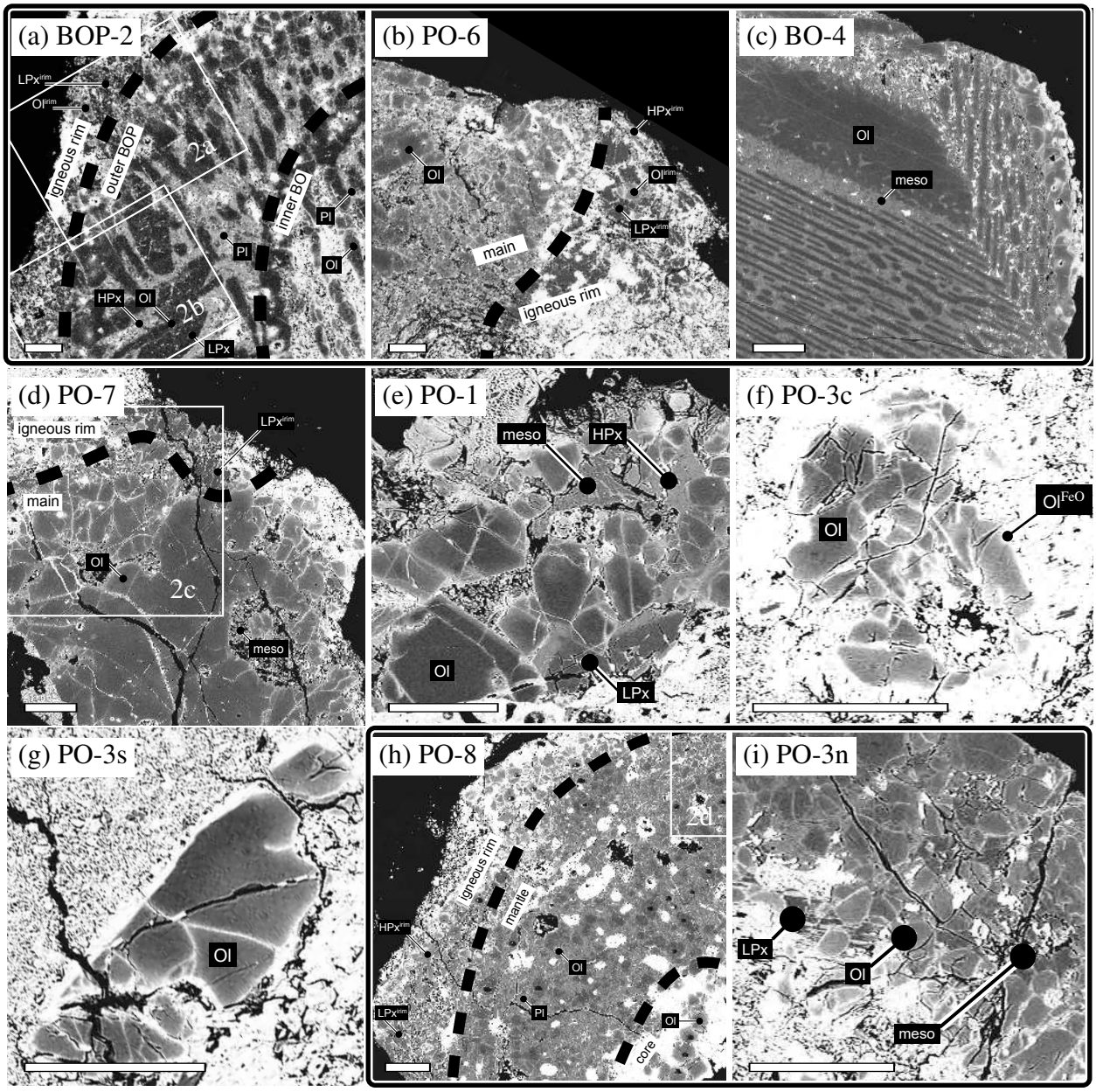

Figure 1: Backscattered electron images of (a, b, c) group 1 chondrules BOP-2, PO-6, and BO-4, (d, e, f, g) group 2 chondrules PO-7, PO-1, PO-3c, and PO-3s, and (h, i) group 3 chondrules PO-8 and PO-3n. Width of scale bar is 100 μm.

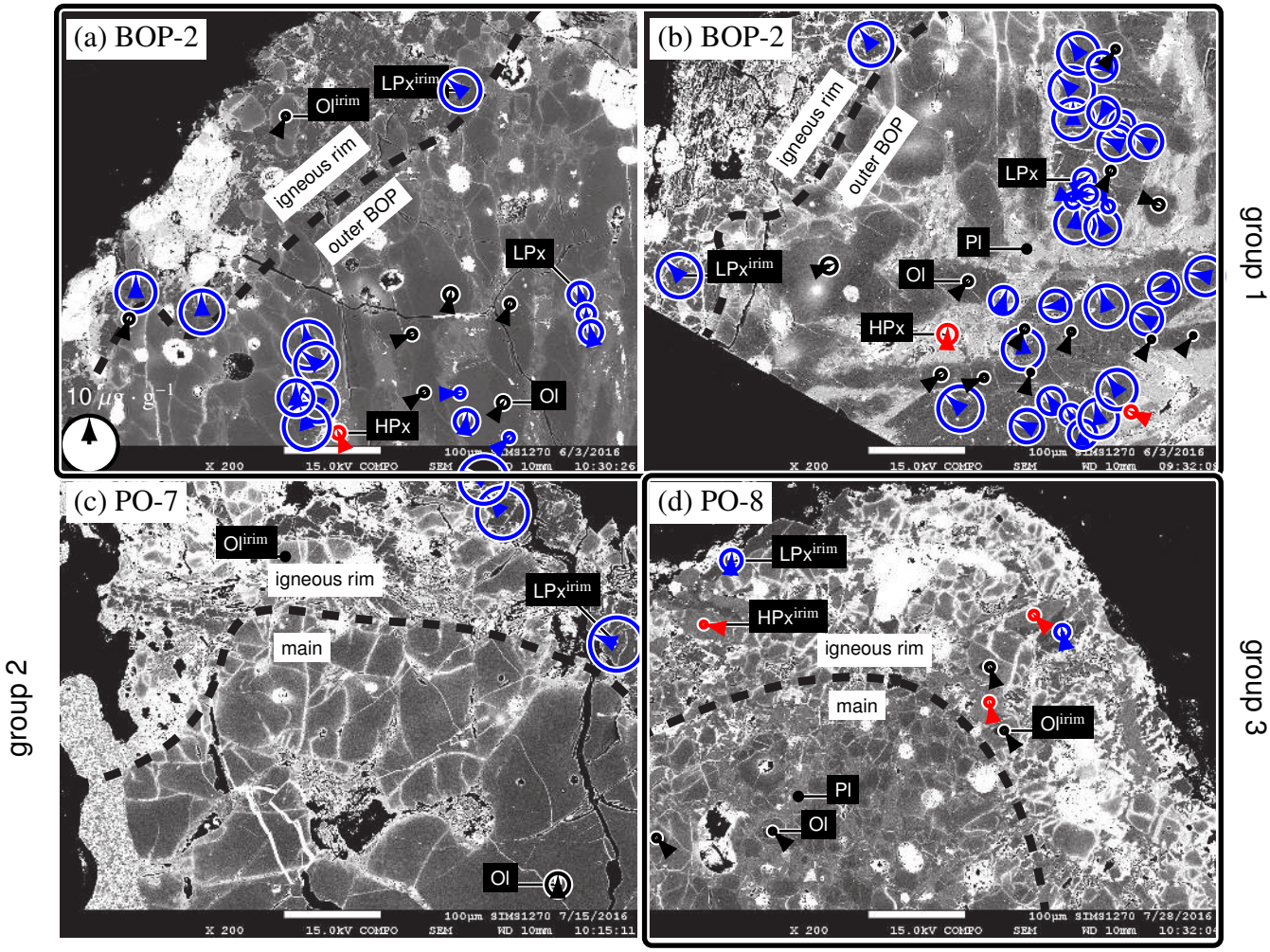

Figure 2: Li element-and-isotope compositions superimposed on BSE images: (a,b) group 1 chondrule BOP-2, (c) group 2 chondrule PO-7, and (d) group 3 chondrule PO-8. Element concentration is proportional to the area of the circle and isotope composition is shown by angle of needle. Angle of nine, twelve, and three o'clock correspondences to δ^7Li −20, 0, and +20‰, respectively. A reference circle shown on left-and-bottom corner of (a) corresponds to [Li] 10 μg · g^{-1} and δ^7Li 0‰.

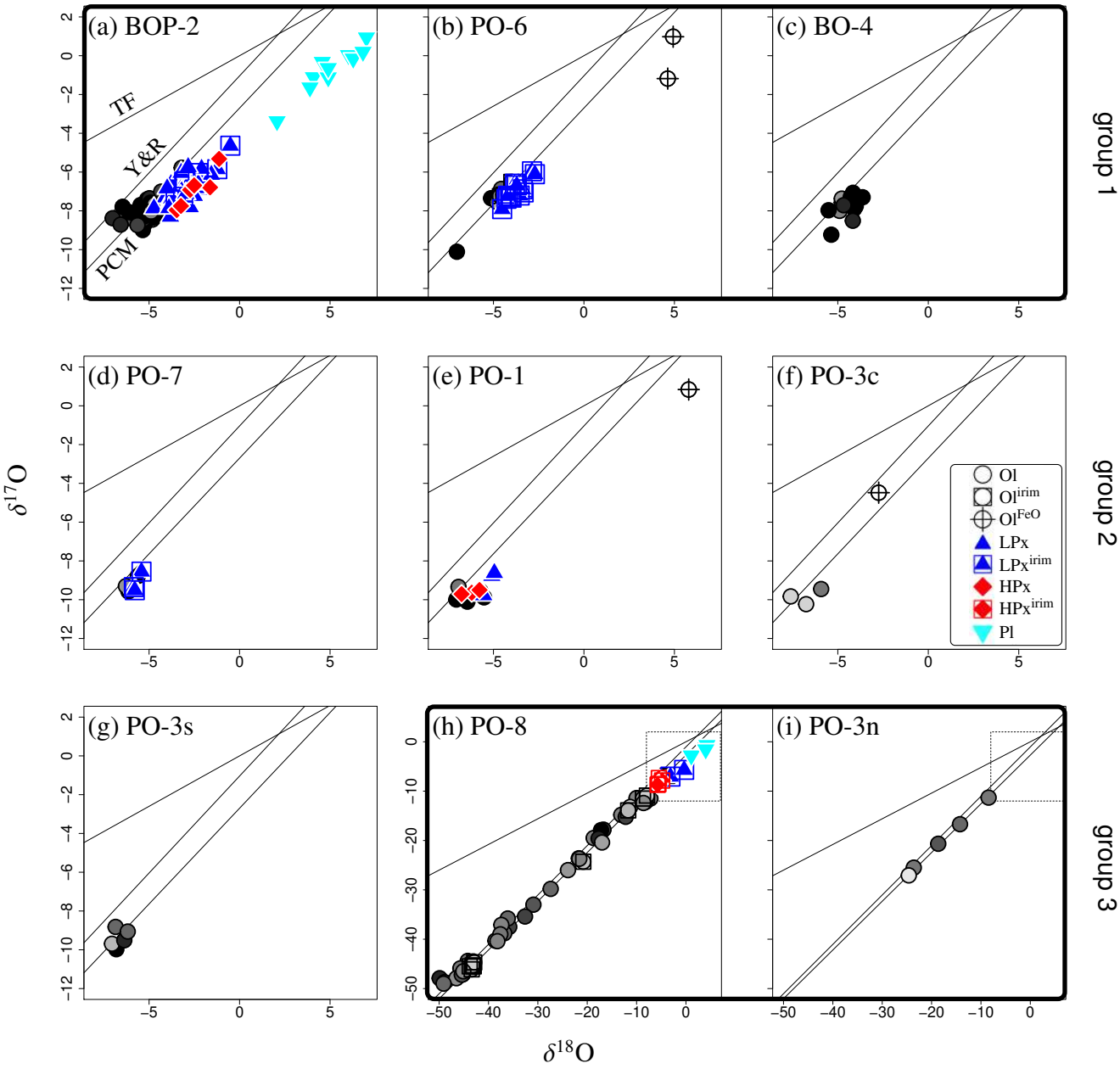

Figure 3: O-isotope compositions of constituents of (a, b, c) group 1 chondrules BOP-2, PO-6, and BO-4, (d, e, f, g) group 2 chondrules PO-7, PO-1, PO-3c, and PO-3s, and (h, i) group 3 chondrules PO-8 and PO-3n. Olivines are shown by circle. Olivines with chemical composition $Fo_{\leq 65}$ (Ol^{FeO}) are shown with a cross symbol. The Fe/Mg ratio is indicated by the color of the circle. White and black circles correspond to Fo_{70} and Fo_{100}, respectively. Low-Ca pyroxenes, high-Ca pyroxenes, and plagioclase are shown by triangle (blue), diamond (red), and inversed triangle (cyan), respectively. Olivines, low-Ca pyroxenes, and high-Ca pyroxenes in igneous rims (Ol^{irim}, LPx^{irim}, and HPx^{irim}) are shown with symbol of square.

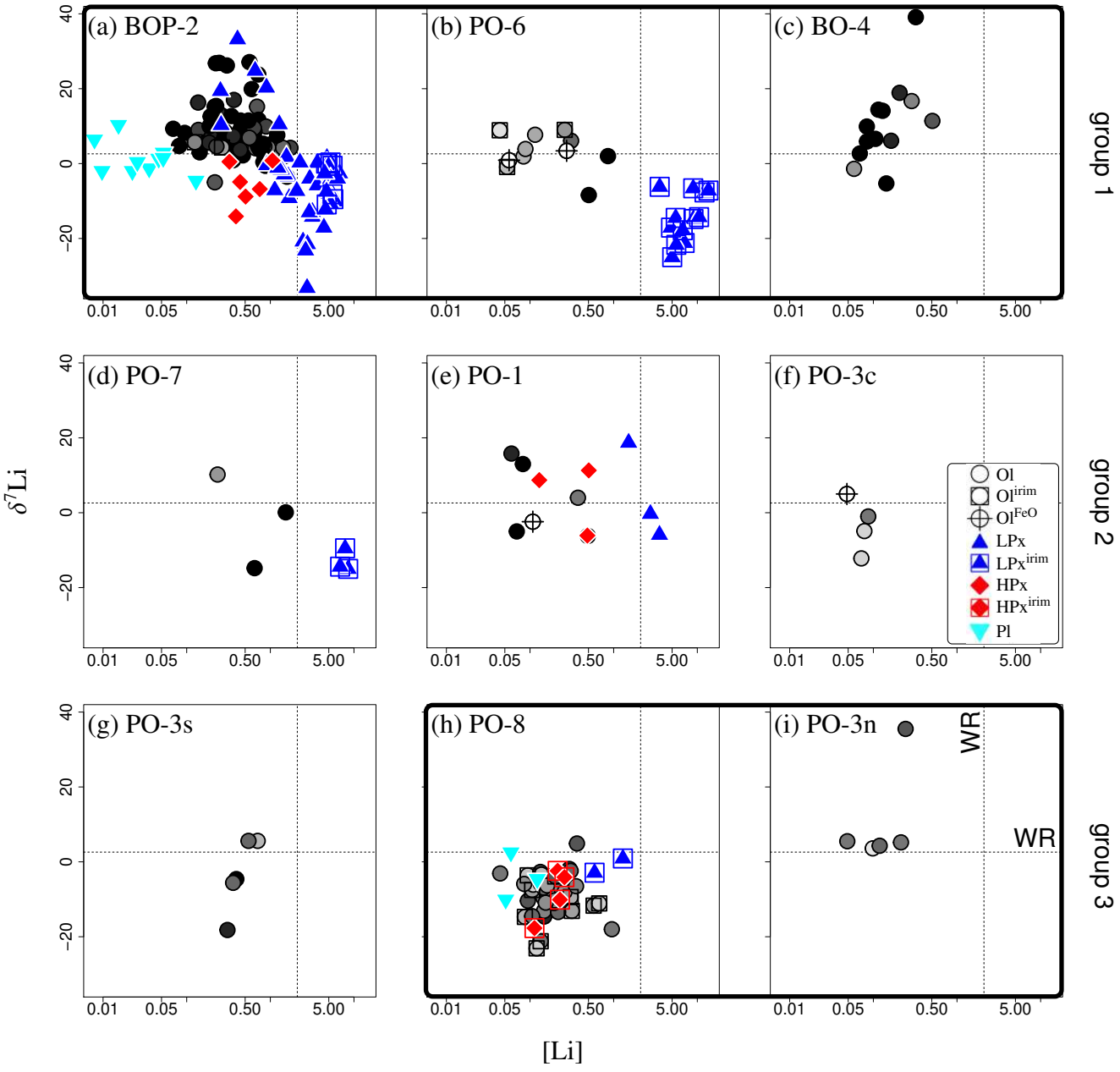

Figure 4: Li element-and-isotope compositions of constituents of (a, b, c) group 1 chondrules BOP-2, PO-6, and BO-4, (d, e, f, g) group 2 chondrules PO-7, PO-1, PO-3c, and PO-3s, and (h, i) group 3 chondrules PO-8 and PO-3n.

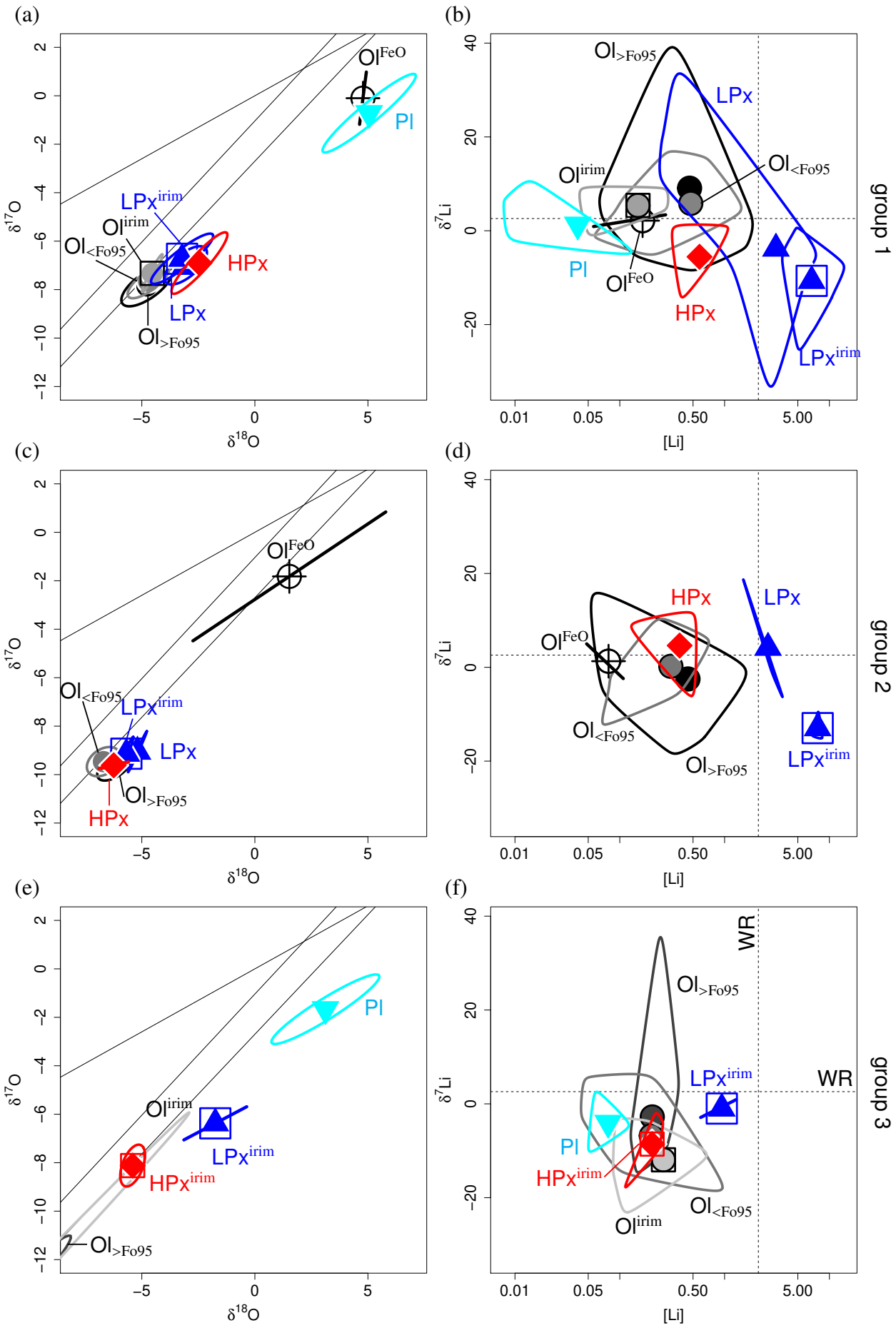

Figure 5: O-isotope and Li-element and -isotope compositions of constituents of (a, b) group 1 chondrule, (c, d) group 2 chondrule, and (e, f) group 3 chondrule. For each constituent and region an average of datasets is shown.

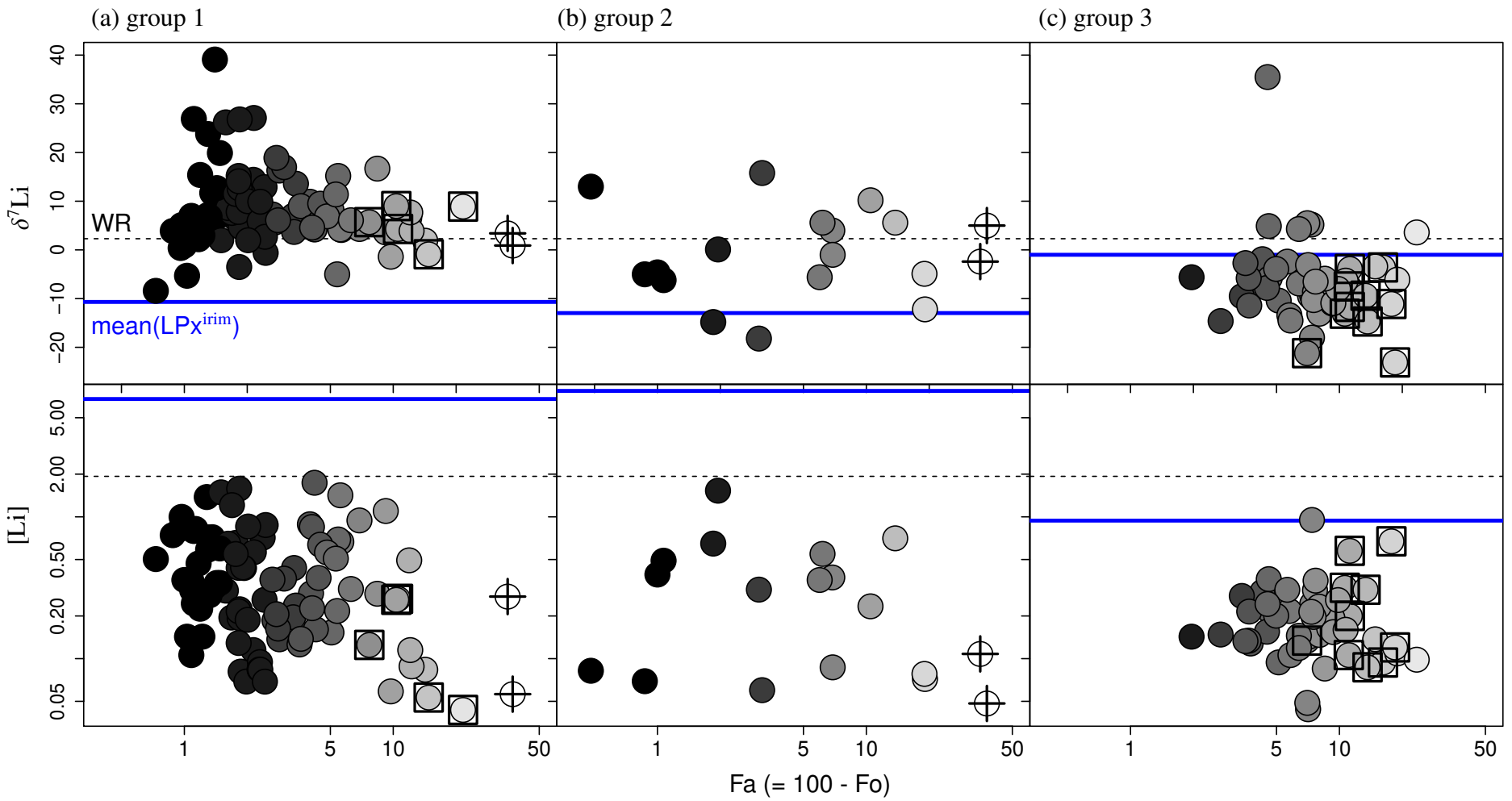

Figure 6: Li element-and-isotope compositions of olivines as a function of the Fe/Mg ratio. Olivines of (a) chondrule group 1, (b) chondrule group 2, and (c) chondrule group 3 are shown. Olivine that occurred in igneous rims (Ol^{irim}) and those with chemical composition Fo$_{\leq 65}$ (Ol^{FeO}) are shown with symbols of square and cross, respectively.

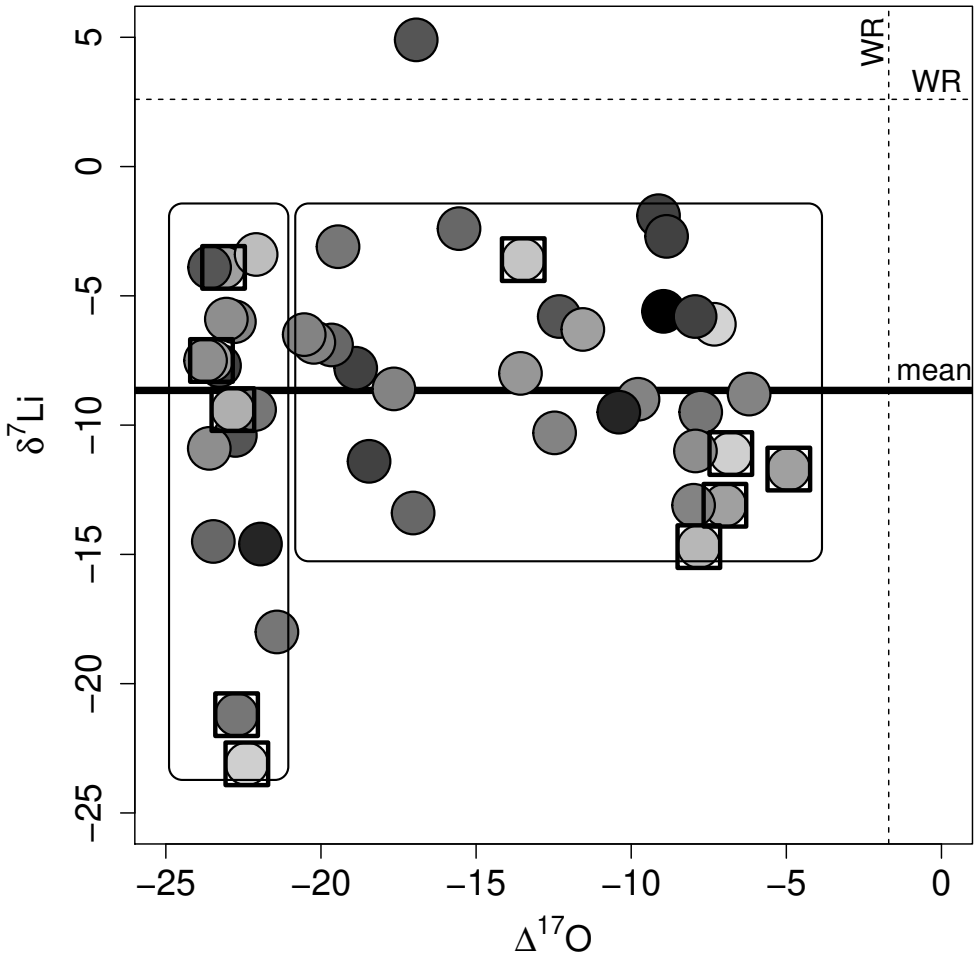

Figure 7: O- and Li-isotope compositions of group 3 chondrule PO-8: The Fe/Mg ratio is shown by color of circle. WR and mean indicate whole-rock Allende and the mean of olivine from group 3 chondrule PO-8, respectively.

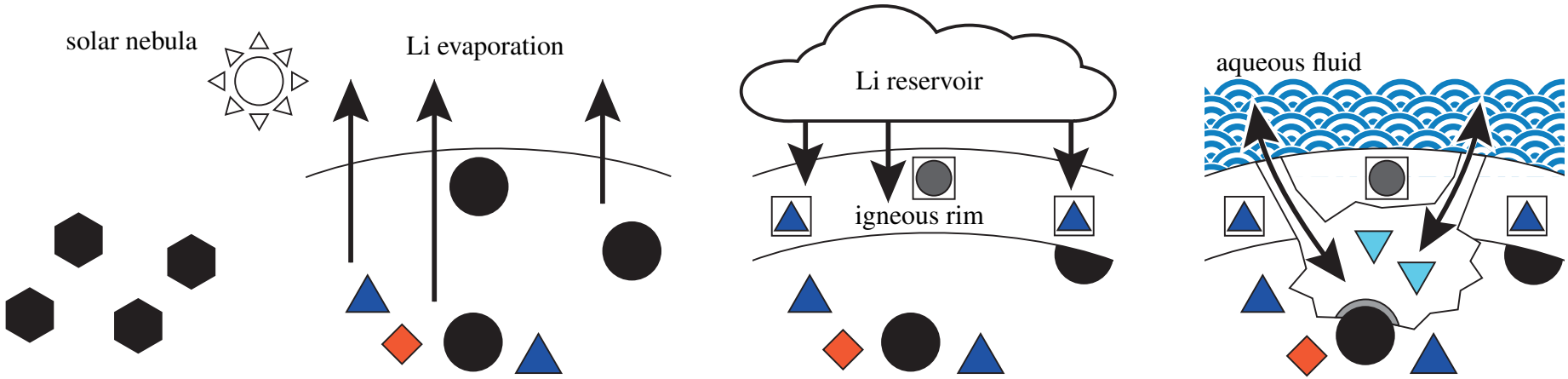

(a) relicts (b) chondrule formation (c) igneous-rim formation (d) asteroidal process

Figure 8: Schematic illustration of Li-isotope evolution.

Appendix 1 RESULTS

All datasets presented in this manuscript are included on our institutional depository DREAM, which is open to the public.

Appendix 1.1. Matrix effect correction on isotope analyses

Matrix effects on instrumental mass fractionation have been known to occur for oxygen- and lithium-isotope measurements by using SIMS. Therefore, we estimated the matrix effects of olivine, low-Ca pyroxene, high-Ca pyroxene, and plagioclase, relative to working standards, based on the isotope measurements of reference olivines, pyroxenes, plagioclases, and synthetic glasses with certain extents of compositional varieties in terms of X_{Mg} ($\equiv \frac{[\mathrm{Mg}]^{\mathrm{mol}}}{[\mathrm{Fe}]^{\mathrm{mol}}+[\mathrm{Mg}]^{\mathrm{mol}}}$), X_{Ca} ($\equiv \frac{[\mathrm{Ca}]^{\mathrm{mol}}}{[\mathrm{Fe}]^{\mathrm{mol}}+[\mathrm{Mg}]^{\mathrm{mol}}+[\mathrm{Ca}]^{\mathrm{mol}}}$), and X_{Na} ($\equiv \frac{[\mathrm{Na}]^{\mathrm{mol}}}{[\mathrm{Ca}]^{\mathrm{mol}}+[\mathrm{Na}]^{\mathrm{mol}}+[\mathrm{K}]^{\mathrm{mol}}}$).

Elemental and isotope compositions of the reference materials analyzed in this study are summarized in Table S1, where major element concentrations were determined by EPMA (JEOL JXA-8800 and JXA-8530F) and FE-SEM (JEOL JSM-7001F) equipped with EDS and Oxford AZtec X-Max and X-act. O-isotope compositions were determined by CO_2 laser fluorination and by using a Finnigan MAT253 mass spectrometer (Tanaka and Nakamura, 2013). Li concentrations and isotope compositions were determined by the method described in Moriguti and Nakamura (1998), except that Li-isotope measurements were carried out using a multicollector-inductively coupled plasma-mass spectrometer, Thermo-Finnigan Neptune (Tang et al., 2007).

Matrix effects on oxygen-isotope analysis Matrix effects on O-isotope analysis of olivine (Fo_{62-100}) relative to the working standard ol-sc (Fo_{91}) were examined by analyses of reference olivines (Fo_{48-100}). The estimated matrix effects of olivine (Fo_{70-100}) were within spot-to-spot reproducibility on the working standard ol-sc (δ^{18}O 0.2‰; 1SD). Thus we did not apply the matrix effect correction for olivines with Fo_{70-100}. Whereas for olivines with Fo_{62-70}, the matrix effects relative to ol-sc were significant (Table S2 and Fig. S1a). Thus we corrected the matrix effect (δ^{18}O from −0.6 to 0‰) on olivines with Fo_{62-70}.

Matrix effects of low-Ca pyroxene ($En_{90-98}Wo_{1-9}$) and high-Ca pyroxene ($En_{54-74}Wo_{26-45}$) relative to the working standard ol-sc were examined by analyses of reference low-Ca pyroxenes ($Wo_{0.3-2}$) and high-Ca pyroxenes (Wo_{37-50}), and chemical-composition dependence was confirmed (Table S2 and Fig. S1b). We corrected the matrix effects on low-Ca pyroxene (δ^{18}O from −2.2 to −1.7‰) and high-Ca pyroxene (δ^{18}O from −0.6 to +0.7‰).

Matrix effect of plagioclase ($Ab_{17-19}An_{81-83}$) relative to the working standard ol-sc was estimated by analyses of reference plagioclases (Ab_{40-98}) and synthetic glasses (Ab_{53-100}), to be δ^{18}O from +0.1 to +0.2‰, from the chemical-composition dependence (Table S2 and Fig. S1c). Since the matrix effects of plagioclases ($Ab_{17-19}An_{81-83}$) were comparable to spot-to-spot reproducibility on ol-sc (δ^{18}O$\sim$ 0.2‰; 1SD), we did not apply the matrix effect correction to plagioclase ($Ab_{17-19}An_{81-83}$).

For any phases examined in this study, the matrix effects were estimated consistently with compositional variations of the phases. By the correction, the matrix-related systematic deviations in analyses were significantly reduced (≤0.4‰). Although uncertainty on the matrix effect correction is controlled also by spot-to-spot reproducibility on each reference material, the standard deviations (1SD) on reference olivines, pyroxenes, plagioclases, and glasses range from 0.1 to 0.4‰. Accordingly we estimated the total

uncertainty including that on the matrix effect correction to be ±0.4‰, which is comparable to or slightly larger than the internal standard error ($1\sigma_m$) on individual analysis (±0.1~0.3‰ in $\delta^{18}O$; Table S4).

Matrix effects on lithium element and isotope analysis Li concentrations were calculated using secondary ion-intensity relative to primary beam-current ($^7Li^+/I_{PRI}$), and a correction factor k ($\frac{\mu g \cdot g^{-1}}{cps/nA}$) estimated by analyses of working standards, ol-sc1 and en-sl1. The correction factor could change from session to session thus the working standards were analyzed for each session.

Representative secondary ion intensities of $^7Li^+$ were 4–9×10^4 cps for ol-sc1 ($[Li]^{\mu g \cdot g^{-1}}$=1.26) and en-sl1 ($[Li]^{\mu g \cdot g^{-1}}$=29.2) at primary beam currents of 1–15 nA, and typical 1SD errors on estimation of elemental concentrations were 8–13%. The correction factor changed depending on the primary beam-current, and the apparent elemental concentrations of the working standards were deviated to some extent from the reference values of the working standards; typically ≤25%, but up to ~ 50% for the low-[Li] standard by the low primary beam-current.

Matrix effects on Li-isotope analysis of olivine relative to ol-sc1 (Fo_{91}), of low-Ca pyroxene and high-Ca pyroxene relative to en-sl1 ($En_{98}Wo_{0.1}$), and of plagioclase ($Ab_{15-37}An_{63-85}$) relative to ol-sc1 were estimated by analyses of reference olivines, pyroxenes, and plagioclases, respectively. As for olivine, we estimated the matrix effects, and corrected them for olivine (Fo_{62-100}) from +2.6 to −0.7‰ relative to ol-sc1 (Table S3 and Figure S2a). Matrix effects of low-Ca pyroxene ($En_{90-98}Wo_{1-9}$) and high-Ca pyroxene ($En_{54-74}Wo_{26-45}$) were estimated to be from +0.0 to +0.4‰, and from +1.0 to +1.8‰, respectively (Table S3). However, spot-to-spot reproducibility on the working standard en-sl1 was 2.6‰ in 1SD (Fig. S2b), thus we did not apply the matrix effect correction. As for plagioclase, matrix effects were estimated to be from −0.6 to −0.6‰ (Table S3), but spot-to-spot reproducibility on the working standard ol-sc1 (0.6‰ in 1SD) was comparable to the estimated matrix effects (Fig. S2c), thus we did not apply the matrix effect correction.

For any phases examined in this study, the matrix effects were estimated consistently with compositional variations of the phases, and the matrix-related systematic bias in Li-isotope analysis was successfully corrected. Thus uncertainty on the matrix effect correction is controlled mainly by the spot-to-spot reproducibility on reference materials. The standard deviations on reference olivines, pyroxenes, and plagioclases range from 0.6 to 2.6‰ (1SD), thus we estimated the total uncertainty on the matrix effect correction to be ±3‰, which is comparable to the internal standard error ($1\sigma_m$) on individual analysis (typically ±1~3‰ and occasionally up to 6‰ in δ^7Li; Table S4).

Appendix 1.2. Oxygen-isotope compositions

O-isotope compositions are shown in Table S4. O-isotope compositions of each chondrule are detailed in this section.

BOP-2, PO-6, and BO-4: Average $\Delta^{17}O$ values of olivines ($Fo_{>65}$ in mantle) of the chondrules are -5.4 ± 0.6‰ (±1SD). Average $\Delta^{17}O$ values for MgO-rich olivines ($Fo_{>95}$ in main region) of BOP-2, PO-6, and BO-4 are −5.5, −6.0, and −5.5‰, respectively.

BOP-2 consists of inner BO, outer BOP, and an igneous rim, as inferred already. We refer to the bar-dominated area and shell-dominated area of the BO as inner BO and shell of inner BO, respectively. We also refer to bar-dominated areas and shell-dominated areas of the BOP as outer BOP and shell of outer BOP, respectively. The BOP-2 is composed of five layers (inner BO, shell of inner BO, outer BOP, shell of outer BOP, and igneous rim) and contains four silicate phases (olivine, high-Ca pyroxene, low-Ca pyroxene, and plagioclase). $\delta^{18}O$ and $\Delta^{17}O$ values for all olivines ($Fo_{>65}$) range from −7.0 to −3.2‰ and from −6.2 to −4.1‰, respectively. Average $\delta^{18}O$ values for olivines ($Fo_{>65}$) in inner BO, shell of inner BO, outer BOP, shell of outer BOP, and igneous rim are −4.6, −4.9, −4.6, −4.7, and −4.8‰, respectively. Average $\Delta^{17}O$ values for olivines ($Fo_{>65}$) in inner BO, shell of inner BO, outer BOP, shell of outer BOP, and igneous rim are −5.4, −5.3, −5.5, −5.3, and −5.4‰, respectively. High-Ca pyroxenes occur only in outer BOP. $\delta^{18}O$ and $\Delta^{17}O$ values for high-Ca pyroxenes range from −3.5 to −1.1‰ and from −6.2 to −4.7‰, respectively. Low-Ca pyroxenes occur in outer BOP and igneous rims. $\delta^{18}O$ values for low-Ca pyroxenes in outer BOP and igneous rims range from −4.7 to −1.6 and from −3.5 to −0.5‰, respectively. $\Delta^{17}O$ values for low-Ca pyroxenes in outer BOP and igneous rims range from −6.4 to −4.3 and from −5.7 to −4.4‰, respectively. O-isotope compositions of high-Ca and low-Ca pyroxenes are heavier than those of olivines $\delta^{18}O$ and $\Delta^{17}O$ values for plagioclase range from +2.1 to +7.0‰ and from −4.5 to −2.7‰, respectively.

PO-6 consists of two layers (main and igneous rims). The main region is dominated by olivines and igneous rim is dominated by olivines and low-Ca pyroxenes. Average $\delta^{18}O$ and $\Delta^{17}O$ values for olivines ($Fo_{>65}$) in main region range from −7.0 to −3.6‰ and from −6.5 to −4.5‰, respectively. Average $\delta^{18}O$ and $\Delta^{17}O$ values for olivines ($Fo_{>65}$) in igneous rim range from −4.6 to −4.0‰ and from −4.9 to −4.4‰, respectively. $\delta^{18}O$ and $\Delta^{17}O$ values for an olivine with Fo_{99} in main region are −7.0 and −6.5‰, respectively. Average of ($\delta^{18}O$, $\Delta^{17}O$) for two FeO-rich olivines (Fo_{63} and Fo_{65}) is (+4.8‰, −2.6‰). Low-Ca pyroxenes occur only in igneous rim. $\delta^{18}O$ and $\Delta^{17}O$ values for low-Ca pyroxene range from −4.5 to −2.7‰ and from −5.6 to −4.5‰, respectively. Except for three olivines (one olivine Fo_{99} and two FeO-rich olivines), O-isotope compositions of olivine and low-Ca pyroxene are consistent.

BO-4 consists of two layers (main and shell regions). The main region consists of barred olivines and mesostasis, and the shell region is dominated by olivine. $\delta^{18}O$ values

for olivines in the main region ($Fo_{>95}$) and olivines in the shell region ($Fo_{>65}$) range from −5.5 to −3.6‰ and from −4.9 to −4.8‰, respectively. O-isotope composition of olivines in the shell region is similar to those in the main region.

PO-7, PO-1, PO-3c, and PO-3s: The O-isotope compositions of olivines ($Fo_{>65}$) of the chondrules are $\Delta^{17}O$ −6.2 ± 0.4‰ (±1SD). Average $\delta^{18}O$ values for olivines ($Fo_{>65}$) of PO-7, PO-1, PO-3c, and PO-3s, are −6.0, −6.3, −6.8, and −6.7‰, respectively. Average $\Delta^{17}O$ values for the olivines ($Fo_{>65}$) of PO-7, PO-1, PO-3c, and PO-3s, are −6.1, −6.5, −6.3, and −6.0‰, respectively. Average $\delta^{18}O$ and $\Delta^{17}O$ values for all analyses made on the olivines in the main regions of the four chondrules ($Fo_{>65}$) are −6.5 and −6.2‰, respectively.

PO-7 consists of main region dominated by olivines and igneous rim dominated by low-Ca pyroxenes. $\delta^{18}O$ and $\Delta^{17}O$ values for olivines ($Fo_{>65}$) range from −6.3 to −5.6‰ and from −6.4 to −5.9‰, respectively. $\delta^{18}O$ and $\Delta^{17}O$ values for low-Ca pyroxenes range from −5.8 to −5.4‰ and from −6.5 to −5.7‰, respectively. O-isotope composition of low-Ca pyroxene on the igneous rim is consistent with those on main region.

PO-1 consists of olivine ($Fo_{>65}$), FeO-rich olivine ($Fo_{\leq 65}$), high-Ca pyroxene, and low-Ca pyroxene. $\delta^{18}O$ and $\Delta^{17}O$ values for olivines ($Fo_{>65}$) range from −7.0 to −5.5‰ and from −7.0 to −5.7‰, respectively. $\delta^{18}O$ and $\Delta^{17}O$ values for an FeO-rich olivine is +5.8 and −2.2‰, respectively. $\delta^{18}O$ and $\Delta^{17}O$ values for high-Ca pyroxenes range from −6.8 to −5.8‰ and from −6.5 to −6.2‰, respectively. $\delta^{18}O$ and $\Delta^{17}O$ values for low-Ca pyroxenes range from −5.5 to −5.0‰ and from −6.9 to −6.0‰, respectively.

PO-3c consists of olivine ($Fo_{>65}$) and FeO-rich olivine (Fo_{62}). $\delta^{18}O$ and $\Delta^{17}O$ values for olivines ($Fo_{>65}$) range from −7.6 to −5.9‰ and from −6.7 to −5.9‰, respectively. $\delta^{18}O$ and $\Delta^{17}O$ values for an FeO-rich olivine are −2.7 and −3.1‰, respectively.

PO-3s consists of olivine ($Fo_{>65}$). $\delta^{18}O$ and Δ^{17}values for olivines range from −7.0 to −6.2‰ and from −6.4 to −5.3‰, respectively.

PO-8 and PO-3n: The O-isotope compositions of olivine in two chondrules (PO-8 and PO-3n) vary significantly, and $\delta^{18}O$ and $\Delta^{17}O$ values range from −49.9 to −3.8‰ and from −23.7 to −4.9‰, respectively.

PO-8 consists of three layers (core, mantle, and igneous rims) with four silicates (olivine, high-Ca pyroxene, low-Ca pyroxene, and plagioclase). $\delta^{18}O$ values for olivines (Fo_{81-99}) in core, mantle, and igneous rims range from −23.9 to −11.3‰, from −49.9 to −7.2‰, and from −43.8 to −3.8‰, respectively. $\Delta^{17}O$ values for the olivines in core, mantle, and igneous rim range from −13.6 to −7.3‰, from −23.7 to −6.2‰, and from −23.5 to −4.9‰, respectively. Variation for O-isotope composition of olivines in core region (Fo_{81-90}) is small relative to olivine in mantle and igneous rims (Fo_{82-98}). High-Ca and low-Ca pyroxenes only occur in igneous rims. $\delta^{18}O$ values for high-Ca and

low-Ca pyroxenes range from −5.7 to −4.8‰ and from −3.1 to −0.4‰, respectively. $\Delta^{17}O$ values for high-Ca and low-Ca pyroxenes range from −5.7 to −4.5‰ and from −5.5 to −5.4‰, respectively. O-isotope compositions of high-Ca and low-Ca pyroxenes are more ^{16}O-depleted than that of olivines. $\delta^{18}O$ and $\Delta^{17}O$ values for plagioclase range from +1.1 to +4.3‰ and from −3.6 to −2.9‰, respectively. O-isotope composition of plagioclases is the heaviest among silicates.

PO-3n is dominated by olivine (Fo_{77-95}). $\delta^{18}O$ and $\Delta^{17}O$ values for the olivines range from −24.6 to −8.4‰ and from −14.3 to −6.9‰, respectively.

Appendix 1.3. Lithium concentrations and isotope compositions

Li concentration and isotope compositions are shown in Table S4. Li concentration and isotope compositions of each chondrule are detailed in this section.

BOP-2 consists of five layers (inner BO, shell of inner BO, outer BOP, shell of outer BOP, and igneous rim) with four silicates (olivine, low-Ca pyroxene, high-Ca pyroxene, and plagioclase), as inferred already. [Li] and δ^7Li of all olivines range from 0.069 to 1.74 $\mu g \cdot g^{-1}$ and from −5.0 to +27.1‰, respectively. [Li] of olivines in inner BO, shell of inner BO, outer BOP, shell of outer BOP, and igneous rim range from 0.22 to 0.72 $\mu g \cdot g^{-1}$, from 0.14 to 1.74 $\mu g \cdot g^{-1}$, from 0.20 to 0.30 $\mu g \cdot g^{-1}$, from 0.069 to 0.64 $\mu g \cdot g^{-1}$, and from 0.12 to 0.26 $\mu g \cdot g^{-1}$, respectively. δ^7Li values for olivines in inner BO, shell of inner BO, outer BOP, shell of outer BOP, and igneous rims range from +11.7 to +27.1‰, from −3.5 to +17.0‰, from +7.0 to +26.2‰, from −5.0 to +16.3‰, and from +4.3 to +5.7‰, respectively. [Li] and δ^7Li values for an olivine (Fo_{98}) are 0.56 $\mu g \cdot g^{-1}$ and +27.1‰. [Li] and δ^7Li values for high-Ca pyroxene occurring in outer BOP range from 0.32 to 1.1 $\mu g \cdot g^{-1}$ and from −14.1 to +0.8‰, respectively. Low-Ca pyroxenes are subdivided into two types based on occurrences in either outer BOP or igneous rim. [Li] values for low-Ca pyroxenes in outer BOP and igneous rim range from 0.25 to 6.7 $\mu g \cdot g^{-1}$ and 4.6 to 5.7 $\mu g \cdot g^{-1}$, respectively. δ^7Li values for low-Ca pyroxenes in outer BOP and igneous rim range from −33.2 to +33.2‰ and from −10.9 to +0.3‰, respectively. [Li] and δ^7Li values of plagioclase range from 0.0079 to 0.13 $\mu g \cdot g^{-1}$ and from −4.6 to +10.3‰, respectively. The plagioclase is the most Li-depleted mineral in BOP-2. Its element abundance is one order of magnitude smaller than that of bulk samples and δ^7Li values for the plagioclase are similar to those for the bulk samples (1.93 $\mu g \cdot g^{-1}$ and +2.4‰; Seitz et al., 2012).

PO-6 consists of two layers (main and igneous rim) dominated by three minerals [olivine ($Fo_{>65}$), FeO-rich olivine ($Fo_{\leq 65}$), and low-Ca pyroxene], as inferred already. [Li] values for olivines ($Fo_{>65}$) in main and igneous rim range from 0.084 to 0.86 $\mu g \cdot g^{-1}$ and from 0.044 to 0.26 $\mu g \cdot g^{-1}$, respectively. δ^7Li values for olivines ($Fo_{>65}$) in main and igneous rim range from −8.4 to +7.7‰ and from −0.9 to +9.0‰, respectively. [Li] and δ^7Li values for an olivine (Fo_{99}) are 0.50 $\mu g \cdot g^{-1}$ and −8.4‰, respectively. The Li-isotope composition of the olivine is the lightest among olivines ($Fo_{>65}$). Average [Li]

and δ^7Li values for FeO-rich olivines (Fo_{63-65}) are 0.17 $\mu g \cdot g^{-1}$ and +2.1‰, respectively. Li-isotope composition of the FeO-rich olivine is similar to that of bulk. [Li] and δ^7Li values for low-Ca pyroxenes in igneous rim range from 3.5 to 13.6 $\mu g \cdot g^{-1}$ and from −25.0 to −6.2‰, respectively.

BO-4 consists of two layers (main and shell) dominated by olivine ($Fo_{>65}$), as inferred already. [Li] values for olivines ($Fo_{>65}$) in main and shell regions range from 0.069 to 0.32 $\mu g \cdot g^{-1}$ and from 0.059 to 0.51 $\mu g \cdot g^{-1}$, respectively. δ^7Li values for olivines ($Fo_{>65}$) in main and shell regions range from −5.3 to +39.1‰ and from −1.4 to +16.7‰, respectively. [Li] and δ^7Li values for an olivine (Fo_{99}) are 0.32 $\mu g \cdot g^{-1}$ and 39.1‰. The Li-isotope composition of the olivine is the heaviest.

PO-7 consists of two layers (main and igneous rim) dominated two minerals [olivine ($Fo_{>65}$) and low-Ca pyroxene], as inferred already. [Li] and δ^7Li values for olivines (Fo_{90-98}) range from 0.23 to 1.53 $\mu g \cdot g^{-1}$ and from −14.8 to +10.2‰. [Li] and δ^7Li values for low-Ca pyroxenes in igneous rim range from 6.8 to 8.5 $\mu g \cdot g^{-1}$ and from −15.0 to −9.5‰, respectively. δ^7Li value for an olivine (Fo_{98}) is −14.8‰, whereas average δ^7Li value for other two olivines (Fo_{90-99}) is +5 ± 5‰.

PO-1 consists of four silicates [olivine ($Fo_{>65}$), FeO-rich olivine ($Fo_{\leq 65}$), high-Ca pyroxene, and low-Ca pyroxene], as inferred already. [Li] and δ^7Li values for olivines ($Fo_{>65}$) range from 0.06 to 0.49 $\mu g \cdot g^{-1}$ and from −6.2 to +15.8‰, respectively. [Li] values for high-Ca and low-Ca pyroxenes range from 0.13 to 0.50 $\mu g \cdot g^{-1}$ and from 1.5 to 3.5 $\mu g \cdot g^{-1}$, respectively. δ^7Li values for high-Ca and low-Ca pyroxenes range from −6.1 to +11.3‰ and from −5.9 to +18.7‰, respectively. [Li] and δ^7Li values for an FeO-rich olivine (Fo_{65}) are 0.11 $\mu g \cdot g^{-1}$ and −2.4‰, respectively. Average [Li] values for minerals increase in order of FeO-rich olivine (Fo_{65}, 0.11 $\mu g \cdot g^{-1}$), olivines ($Fo_{>65}$, 0.2 $\mu g \cdot g^{-1}$), high-Ca pyroxene (0.4 $\mu g \cdot g^{-1}$), and low-Ca pyroxene (2.6 $\mu g \cdot g^{-1}$).

PO-3c is dominated by olivines, as inferred already. A portion of olivines is classified as FeO-rich (Fo_{62}) olivines. [Li] and δ^7Li values for olivines (Fo_{81-93}) range from 0.072 to 0.087 $\mu g \cdot g^{-1}$ and from −12.2 to −1.0‰, respectively. [Li] and δ^7Li values for the FeO-rich olivine (Fo_{62}) are 0.048 $\mu g \cdot g^{-1}$ and +5.0‰, respectively.

PO-3s is dominated by olivines ($Fo_{>65}$), as inferred already. [Li] and δ^7Li values for the olivines range from 0.31 to 0.71 $\mu g \cdot g^{-1}$ and from −18.2 to +5.6‰, respectively. δ^7Li value for an olivine (Fo_{97}) is significantly light (−18.2‰).

PO-8 consists of three layers and four silicates, as inferred already. [Li] values for olivines ($Fo_{>65}$) in core, mantle, and igneous rim range from 0.11 to 0.26 $\mu g \cdot g^{-1}$, from 0.044 to 0.95 $\mu g \cdot g^{-1}$, and from 0.087 to 0.67 $\mu g \cdot g^{-1}$, respectively. δ^7Li values for the olivines in core, mantle, and igneous rim range from −8.0 to −6.1‰, from −18.0 to +4.9‰, and from −23.1 to −3.6‰, respectively. Average [Li] values for olivines in three layers are consistent but average δ^7Li values decrease from core to igneous rim. [Li] values for high-Ca and low-Ca pyroxenes range from 0.11 to 0.26 $\mu g \cdot g^{-1}$ and from 0.59 to 1.3 $\mu g \cdot g^{-1}$, respectively. δ^7Li values for high-Ca and low-Ca pyroxenes range

from −17.7 to −2.4‰ and from −2.9 to +0.9‰, respectively. [Li] and δ^7Li values for plagioclase range from 0.051 to 0.12 $\mu g \cdot g^{-1}$ and from −10.1 to +2.5‰, respectively. Average [Li] values for minerals increase in order of plagioclase (0.08 $\mu g \cdot g^{-1}$), olivines (0.2 $\mu g \cdot g^{-1}$ in three occurrences), high-Ca pyroxene (0.2 $\mu g \cdot g^{-1}$), and low-Ca pyroxene (0.9 $\mu g \cdot g^{-1}$).

PO-3n is dominated by olivines ($Fo_{>65}$), as inferred already. [Li] and δ^7Li values for olivines range from 0.049 to 0.24 $\mu g \cdot g^{-1}$ and from +3.6 to +35.5‰. δ^7Li value of an olivine (Fo_{95}) is +35.5‰, whereas average δ^7Li value for other four olivines (Fo_{77-94}) is +4.7‰.

References

Moriguti, T. and Nakamura, E. (1998). Across-arc variation of Li isotopes in arc lavas and implications for crust/mantle recycling at subduction zones. *Earth Planet. Sci. Lett.*, **163**, 167–174.

Seitz, H.-M., Zipfel, J., Brey, G. P., and Ott, U. (2012). Lithium isotope compositions of chondrules, CAI and a dark inclusion from Allende and ordinary chondrites. *Earth Planet. Sci. Lett.*, **329**, 51–59.

Tanaka, R. and Nakamura, E. (2013). Determination of 17O-excess of terrestrial silicate/oxide minerals with respect to Vienna Standard Mean Ocean Water (VSMOW). *Rapid Communications in Mass Spectrometry*, **27**(2), 285–297.

Tang, Y. J., Zhang, H. F., and Ying, J. F. (2007). Review of the lithium isotope system as a geochemical tracer. *International Geology Review*, **49**, 374–388.

Table S1: Elemental and isotope compositions of reference materials.

reference material	X_{Mg}	X_{Ca}	X_{Na}	$\delta^{18}O$	$\delta^{17}O$	$\delta^{7}Li$	$[Li]^{\mu g \cdot g^{-1}}$
olivine							
ol-sc	0.91	–	–	5.22	2.68	–	–
ol-AY	1.00	–	–	2.85	1.45	–	–
ol-fo	0.99	–	–	23.6	12.4	–	–
ol-LS1-A	0.70	–	–	5.34	2.80	–	–
ol-NWA6704(b)	0.48	–	–	4.09	1.12	–	–
ol-sc1	0.91	–	–	–	–	2.93	1.26
ol-fo1	0.99	–	–	–	–	5.57	29.0
ol-fa1	0.01	–	–	–	–	14.8	28.8
low-Ca pyroxene							
opx-tz1001	0.91	0.003	–	10.8	5.62	–	–
opx-klb1	0.90	0.02	–	5.73	3.01	–	–
en-sl1	0.98	0.001	–	–	–	1.86	29.2
high-Ca pyroxene							
cpx-sax33	0.72	0.37	–	5.85	3.03	–	–
cpx-klb1	0.90	0.46	–	5.42	2.82	–	–
cpx-di-tz1001	1.00	0.50	–	20.6	10.7	–	–
cpx-sae113	0.84	0.31	–	–	–	0.14	3.76
cpx-sae116	0.84	0.34	–	–	–	-7.52	9.02
cpx-sae152	0.82	0.39	–	–	–	1.74	4.85
cpx-sax39c	0.82	0.33	–	–	–	3.47	3.05
plagioclase							
pl-alb21245	–	–	0.98	10.6	5.56	–	–
pl-lab	–	–	0.40	6.43	3.38	–	–
pl-anorthoclase-c	–	–	0.72	–	–	2.2	21.6
pl-bytownite-c2s	–	–	0.42	–	–	-38.5	8.04
synthetic glass							
gl-ab100	–	–	1.00	18.5	9.39	–	–
gl-an25ab75	–	–	0.78	17.4	8.91	–	–
gl-an50ab50	–	–	0.53	16.5	8.45	–	–

Major element compositions, shown by X_{Mg} ($\equiv \frac{[Mg]^{mol}}{[Fe]^{mol}+[Mg]^{mol}}$), X_{Ca} ($\equiv \frac{[Ca]^{mol}}{[Fe]^{mol}+[Mg]^{mol}+[Ca]^{mol}}$), and X_{Na} ($\equiv \frac{[Na]^{mol}}{[Ca]^{mol}+[Na]^{mol}+[K]^{mol}}$), were determined by EPMA and SEM-EDS. O- and Li-isotope compositions were determined by laser fluorination and gas mass spectrometry, and by wet chemistry with ICP-MS, respectively. See text for analytical details.

Table S2: Matrix effects relative to a working standard for O isotope analysis.

phase	formula	${}^{\mathrm{calc}}\Delta\delta^{18}\mathrm{O}_{\mathrm{ws}}^{\mathrm{phase}}$	remark
olivine (Fo_{70-100})	$\Delta\delta^{18}\mathrm{O}_{\mathrm{ol-sc}}^{\mathrm{phase}} \equiv 0$	$\equiv 0$	no correction
olivine (Fo_{62-70})	$\Delta\delta^{18}\mathrm{O}_{\mathrm{ol-sc}}^{\mathrm{phase}} = 6.9 \times (\mathrm{X}_{\mathrm{Mg}} - 0.7)$	-0.6 to $+0.0$‰	correction applied
low-Ca pyroxene ($\mathrm{En}_{90-98}\mathrm{Wo}_{1-9}$)	$\Delta\delta^{18}\mathrm{O}_{\mathrm{ol-sc}}^{\mathrm{phase}} = 6.7 \times \mathrm{X}_{\mathrm{Ca}} - 2.3$	-2.2 to -1.7‰	correction applied
high-Ca pyroxene ($\mathrm{En}_{54-74}\mathrm{Wo}_{26-45}$)	$\Delta\delta^{18}\mathrm{O}_{\mathrm{ol-sc}}^{\mathrm{phase}} = 6.7 \times \mathrm{X}_{\mathrm{Ca}} - 2.3$	-0.6 to $+0.7$‰	correction applied
plagioclase ($\mathrm{Ab}_{17-19}\mathrm{An}_{81-83}$)	$\Delta\delta^{18}\mathrm{O}_{\mathrm{ol-sc}}^{\mathrm{phase}} = -5.8 \times \mathrm{X}_{\mathrm{Na}} + 1.2$	$+0.1$ to $+0.2$‰	no correction

Table S3: Matrix effects relative to working standards for Li isotope analysis.

phase	formula	${}^{\text{calc}}\Delta\delta^7\text{Li}_{\text{ws}}^{\text{phase}}$	remark
olivine (Fo_{62-100})	$\Delta\delta^7\text{Li}_{\text{ol-sc1}}^{\text{phase}} = -9.1 \times (X_{\text{Mg}} - 0.91)$	+2.6 to −0.8‰	correction applied
low-Ca pyroxene ($En_{90-98}Wo_{1-9}$)	$\Delta\delta^7\text{Li}_{\text{en-sl1}}^{\text{phase}} = 4.0 \times X_{\text{Ca}}$	+0.0 to +0.4‰	no correction
high-Ca pyroxene ($En_{54-74}Wo_{26-45}$)	$\Delta\delta^7\text{Li}_{\text{en-sl1}}^{\text{phase}} = 4.0 \times X_{\text{Ca}}$	+1.0 to +1.8‰	no correction
plagioclase ($Ab_{17-19}An_{81-83}$)	$\Delta\delta^7\text{Li}_{\text{ol-sc1}}^{\text{phase}} = -0.02 \times X_{\text{Na}} - 0.63$	−0.6 to −0.6‰	no correction

Table S4: Spot-to-spot O- and Li-isotope compositions of chondrule constituents. Uncertainty (1SD) is shown in parenthesis.

		phase	occurrence	compo*	O-analysis ID	Li-analysis ID	$\delta^{18}O$	$\delta^{17}O$	$\Delta^{17}O$	$\delta^{7}Li$	$[Li]^{\mu g \cdot g^{-1}}$
group 1	BOP-2	Ol	shell of inner BO	Fo_{95}	oxy-ol-chd2@9364	liso-ol-chd2@8692	-4.1 (1)	-7.2 (2)	-5.1	8.2 (1.3)	0.153
	BOP-2	Ol	shell of inner BO	Fo_{94}	oxy-ol-chd2@9365	liso-ol-chd2@8693	-4.7 (1)	-7.9 (3)	-5.5	4.2 (0.79)	1.42
	BOP-2	Ol	shell of inner BO	Fo_{96}	oxy-ol-chd2@9366	liso-ol-chd2@8694	-3.2 (1)	-5.8 (2)	-4.1	8.5 (1.1)	0.289
	BOP-2	Ol	shell of inner BO	Fo_{95}	oxy-ol-chd2@9433	liso-ol-chd2@8671	-3.9 (2)	-7.4 (3)	-5.4	15.2 (0.63)	0.693
	BOP-2	Ol	shell of inner BO	Fo_{98}	oxy-ol-chd2@9434	liso-ol-chd2@8672	-3.9 (1)	-7.7 (3)	-5.7	10.4 (1.2)	0.195
	BOP-2	Ol	inner BO	Fo_{99}	oxy-ol-chd2@9455	liso-ol-chd2@8705	-4.3 (1)	-7.9 (3)	-5.6	26.9 (2.0)	0.245
	BOP-2	Ol	shell of inner BO	Fo_{98}	oxy-ol-chd2@9456	liso-ol-chd2@8706	-4.8 (1)	-8.0 (3)	-5.5	6.4 (1.2)	0.655
	BOP-2	Ol	inner BO	Fo_{99}	oxy-ol-chd2@9473	liso-ol-chd2@8709	-5.8 (1)	-8.4 (3)	-5.4	23.8 (1.1)	0.717
	BOP-2	Ol	inner BO	Fo_{98}	oxy-ol-chd2@9474	liso-ol-chd2@8674	-4.6 (1)	-8.3 (3)	-5.9	27.1 (1.3)	0.563
	BOP-2	Ol	shell of outer BOP	Fo_{98}	oxy-ol-chd2@9492	liso-ol-chd2@8945	-4.7 (1)	-8.3 (3)	-5.9	12.9 (1.9)	0.26
	BOP-2	Ol	shell of outer BOP	Fo_{97}	oxy-ol-chd2@9493	liso-ol-chd2@8946	-3.8 (1)	-7.5 (2)	-5.6	16.3 (3.0)	0.137
	BOP-2	Ol	shell of outer BOP	Fo_{98}	oxy-ol-chd2@9494	liso-ol-chd2@8947	-3.8 (2)	-7.8 (4)	-5.8	4.7 (3.2)	0.0811
	BOP-2	Ol	shell of inner BO	Fo_{98}	oxy-ol-chd2@9504	liso-ol-chd2@8712	-4.4 (1)	-7.4 (3)	-5.1	-0.6 (1.0)	0.876
	BOP-2	Ol	inner BO	Fo_{99}	oxy-ol-chd2@9505	liso-ol-chd2@8726	-3.3 (1)	-7.0 (3)	-5.2	11.7 (1.1)	0.719
	BOP-2	Ol	shell of inner BO	Fo_{96}	oxy-ol-chd2@9507	liso-ol-chd2@8975	-6.3 (2)	-8.4 (4)	-5.1	9.9 (1.2)	0.887
	BOP-2	Ol	shell of outer BOP	Fo_{97}	oxy-ol-chd2@9509	liso-ol-chd2@8977	-7.0 (2)	-8.4 (3)	-4.7	13.6 (1.8)	0.237
	BOP-2	Ol	shell of outer BOP	Fo_{96}	oxy-ol-chd2@9511	liso-ol-chd2@8979	-5.5 (1)	-7.9 (3)	-5.1	7.3 (1.5)	0.371
	BOP-2	Ol	shell of outer BOP	Fo_{95}	oxy-ol-chd2@9512	liso-ol-chd2@8980	-6.0 (1)	-8.4 (3)	-5.2	-5.0 (1.9)	0.217
	BOP-2	Ol	shell of outer BOP	Fo_{99}	oxy-ol-chd2@9513	liso-ol-chd2@8981	-5.5 (1)	-7.7 (3)	-4.9	2.2 (1.4)	0.469
	BOP-2	Ol	shell of outer BOP	Fo_{96}	oxy-ol-chd2@9515	liso-ol-chd2@8948	-5.0 (1)	-7.7 (3)	-5.1	5.6 (2.9)	0.126
	BOP-2	Ol	shell of outer BOP	Fo_{96}	oxy-ol-chd2@9733	liso-ol-chd2@8949	-3.4 (1)	-7.2 (3)	-5.4	7.7 (2.4)	0.161
	BOP-2	Ol	shell of outer BOP	Fo_{98}	oxy-ol-chd2@9734	liso-ol-chd2@8950	-4.6 (1)	-7.5 (3)	-5.1	9.3 (2.8)	0.069
	BOP-2	Ol	shell of outer BOP	Fo_{98}	oxy-ol-chd2@9735	liso-ol-chd2@8951	-3.9 (2)	-7.0 (3)	-4.9	8.2 (3.3)	0.0946
	BOP-2	Ol	outer BOP	Fo_{97}	oxy-ol-chd2@9737	liso-ol-chd2@8952	-4.5 (2)	-7.7 (3)	-5.4	7.0 (2.4)	0.196
	BOP-2	Ol	outer BOP	Fo_{98}	oxy-ol-chd2@9738	liso-ol-chd2@8953	-4.7 (1)	-8.2 (3)	-5.7	26.2 (1.8)	0.302
	BOP-2	Ol	shell of outer BOP	Fo_{96}	oxy-ol-chd2@9739	liso-ol-chd2@8954	-4.3 (1)	-8.0 (3)	-5.7	9.0 (2.3)	0.138
	BOP-2	Ol	shell of inner BO	Fo_{99}	oxy-ol-chd2@9749	liso-ol-chd2@8673	-5.4 (2)	-9.0 (3)	-6.2	7.1 (0.91)	0.342
	BOP-2	Ol	shell of inner BO	Fo_{98}	oxy-ol-chd2@9750	liso-ol-chd2@8710	-3.9 (2)	-8.0 (3)	-6.0	9.0 (1.5)	0.436
	BOP-2	Ol	shell of inner BO	Fo_{96}	oxy-ol-chd2@9751	liso-ol-chd2@8711	-5.2 (1)	-8.2 (3)	-5.5	4.6 (1.2)	0.849
	BOP-2	Ol	shell of inner BO	Fo_{99}	oxy-ol-chd2@9753	liso-ol-chd2@8713	-4.3 (2)	-7.2 (3)	-5.0	5.3 (1.2)	0.822
	BOP-2	Ol	shell of inner BO	Fo_{88}	oxy-ol-chd2@9754	liso-ol-chd2@8714	-5.6 (1)	-8.4 (4)	-5.4	6.6 (1.4)	0.494
	BOP-2	Ol	shell of inner BO	Fo_{99}	oxy-ol-chd2@9758	liso-ol-chd2@8715	-4.1 (1)	-7.6 (4)	-5.4	3.9 (1.0)	0.743
	BOP-2	Ol	shell of inner BO	Fo_{99}	oxy-ol-chd2@9759	liso-ol-chd2@8716	-4.3 (1)	-7.5 (4)	-5.3	7.2 (1.3)	0.588
	BOP-2	Ol	shell of inner BO	Fo_{99}	oxy-ol-chd2@9760	liso-ol-chd2@8717	-5.7 (1)	-8.1 (3)	-5.2	3.0 (2.7)	0.143
	BOP-2	Ol	inner BO	Fo_{98}	oxy-ol-chd2@9762	liso-ol-chd2@8727	-3.3 (2)	-6.5 (3)	-4.7	26.8 (2.0)	0.223
	BOP-2	Ol	shell of inner BO	Fo_{98}	oxy-ol-chd2@9763	liso-ol-chd2@8728	-5.1 (1)	-7.8 (4)	-5.1	7.6 (0.96)	1.21
	BOP-2	Ol	shell of inner BO	Fo_{99}	oxy-ol-chd2@9764	liso-ol-chd2@8729	-4.2 (1)	-8.1 (3)	-5.9	0.9 (1.9)	0.359
	BOP-2	Ol	shell of inner BO	Fo_{97}	oxy-ol-chd2@9868	liso-ol-chd2@8736	-6.6 (1)	-8.7 (3)	-5.3	3.7 (1.4)	0.436
	BOP-2	Ol	shell of inner BO	Fo_{98}	oxy-ol-chd2@9869	liso-ol-chd2@8737	-6.5 (1)	-7.8 (3)	-4.4	8.6 (1.2)	0.647

Table S4: Continued

	phase	occurrence	compo*	O-analysis ID	Li-analysis ID	$\delta^{18}O$	$\delta^{17}O$	$\Delta^{17}O$	$\delta^{7}Li$	[Li]$^{\mu g \cdot g^{-1}}$
BOP-2	Ol	shell of inner BO	Fo_{99}	oxy-ol-chd2@9870	liso-ol-chd2@8738	-5.4 (2)	-8.4 (3)	-5.5	3.3 (1.4)	0.795
BOP-2	Ol	shell of inner BO	Fo_{99}	oxy-ol-chd2@9872	liso-ol-chd2@8739	-4.4 (2)	-7.9 (3)	-5.6	12.7 (2.1)	0.342
BOP-2	Ol	shell of inner BO	Fo_{99}	oxy-ol-chd2@9873	liso-ol-chd2@8740	-5.3 (2)	-8.7 (3)	-6.0	6.8 (1.8)	0.28
BOP-2	Ol	shell of inner BO	Fo_{99}	oxy-ol-chd2@9874	liso-ol-chd2@8741	-5.1 (2)	-8.2 (4)	-5.5	7.0 (2.3)	0.355
BOP-2	Ol	shell of inner BO	Fo_{97}	oxy-ol-chd2@9876	liso-ol-chd2@8742	-5.3 (2)	-8.4 (3)	-5.7	17.0 (1.8)	0.367
BOP-2	Ol	shell of inner BO	Fo_{98}	oxy-ol-chd2@9877	liso-ol-chd2@8743	-6.1 (1)	-8.1 (3)	-4.9	7.8 (1.5)	0.437
BOP-2	Ol	inner BO	Fo_{99}	oxy-ol-chd2@9879	liso-ol-chd2@8707	-5.2 (2)	-8.3 (3)	-5.5	15.4 (1.7)	0.225
BOP-2	Ol	inner BO	Fo_{99}	oxy-ol-chd2@9880	liso-ol-chd2@8708	-5.4 (1)	-7.9 (3)	-5.1	19.9 (1.2)	0.599
BOP-2	Ol	shell of outer BOP	Fo_{96}	oxy-ol-chd2@9881	liso-ol-chd2@8978	-5.6 (1)	-8.7 (3)	-5.8	9.5 (1.1)	0.637
BOP-2	Ol	shell of inner BO	Fo_{95}	oxy-ol-chd2@9892	liso-ol-chd2@8973	-4.3 (2)	-7.5 (3)	-5.2	6.9 (1.2)	0.561
BOP-2	Ol	shell of inner BO	Fo_{97}	oxy-ol-chd2@9893	liso-ol-chd2@8974	-5.0 (1)	-7.4 (4)	-4.8	5.6 (1.1)	0.186
BOP-2	Ol	shell of inner BO	Fo_{98}	oxy-ol-chd2@9896	liso-ol-chd2@8696	-5.0 (1)	-8.0 (2)	-5.5	11.5 (1.3)	0.44
BOP-2	Ol	shell of inner BO	Fo_{98}	oxy-ol-chd2@9897	liso-ol-chd2@8695	-4.9 (1)	-7.6 (2)	-5.0	11.5 (1.5)	0.547
BOP-2	Ol^{irim}	igneous rim	Fo_{89}	oxy-ol-chd2@9902	liso-ol-chd2@8982	-4.7 (1)	-7.7 (3)	-5.2	4.3 (1.7)	0.264
BOP-2	Ol^{irim}	igneous rim	Fo_{92}	oxy-ol-chd2@9903	liso-ol-chd2@8983	-4.9 (2)	-8.1 (3)	-5.5	5.7 (2.4)	0.125
BOP-2	Ol	shell of outer BOP	Fo_{98}	oxy-ol-chd2@9920	liso-ol-chd2@8955	-4.3 (2)	-7.6 (3)	-5.4	12.6 (2.1)	0.193
BOP-2	Ol	shell of outer BOP	Fo_{98}	oxy-ol-chd2@9921	liso-ol-chd2@8956	-4.3 (2)	-7.8 (3)	-5.5	15.2 (1.9)	0.216
BOP-2	Ol	shell of outer BOP	Fo_{97}	oxy-ol-chd2@9923	liso-ol-chd2@8957	-4.0 (2)	-7.2 (4)	-5.1	7.3 (3.0)	0.361
BOP-2	Ol	shell of outer BOP	Fo_{96}	oxy-ol-chd2@9924	liso-ol-chd2@8958	-4.3 (2)	-7.0 (3)	-4.8	4.6 (2.2)	0.227
BOP-2	Ol	shell of outer BOP	Fo_{98}	oxy-ol-chd2@9925	liso-ol-chd2@8959	-3.9 (1)	-7.4 (3)	-5.4	10.0 (2.1)	0.188
BOP-2	Ol	shell of inner BO	Fo_{94}	oxy-ol-chd2@10013	liso-ol-chd2@8730	-4.8 (1)	-8.5 (4)	-5.9	4.1 (1.4)	0.666
BOP-2	Ol	shell of inner BO	Fo_{98}	oxy-ol-chd2@10014	liso-ol-chd2@8731	-4.5 (2)	-7.9 (3)	-5.6	4.6 (1.3)	0.713
BOP-2	Ol	shell of inner BO	Fo_{96}	oxy-ol-chd2@10015	liso-ol-chd2@8732	-5.1 (2)	-7.4 (2)	-4.8	4.2 (0.74)	1.74
BOP-2	Ol	shell of inner BO	Fo_{99}	oxy-ol-chd2@10017	liso-ol-chd2@8733	-4.8 (2)	-8.3 (3)	-5.9	4.4 (1.8)	0.304
BOP-2	Ol	shell of inner BO	Fo_{99}	oxy-ol-chd2@10018	liso-ol-chd2@8734	-5.0 (1)	-7.9 (3)	-5.3	4.0 (0.94)	1.38
BOP-2	Ol	shell of inner BO	Fo_{99}	oxy-ol-chd2@10019	liso-ol-chd2@8735	-5.1 (2)	-7.8 (3)	-5.1	5.1 (0.94)	1
BOP-2	Ol	shell of inner BO	Fo_{99}	oxy-ol-chd2@10021	liso-ol-chd2@8968	-5.2 (2)	-7.8 (3)	-5.1	2.0 (1.3)	1.49
BOP-2	Ol	shell of inner BO	Fo_{91}	oxy-ol-chd2@10022	liso-ol-chd2@8969	-5.2 (2)	-8.1 (3)	-5.4	3.6 (1.4)	1.1
BOP-2	Ol	shell of inner BO	Fo_{99}	oxy-ol-chd2@10023	liso-ol-chd2@8970	-5.4 (1)	-8.1 (3)	-5.3	0.4 (1.8)	0.826
BOP-2	Ol	shell of inner BO	Fo_{98}	oxy-ol-chd2@10025	liso-ol-chd2@8971	-5.2 (1)	-8.4 (4)	-5.7	-3.5 (1.0)	1.58
BOP-2	Ol	shell of inner BO	Fo_{93}	oxy-ol-chd2@10026	liso-ol-chd2@8972	-5.2 (1)	-7.6 (3)	-4.9	4.3 (1.3)	0.944
BOP-2	LPx^{irim}	igneous rim	$En_{98}Wo_1$	oxy-opx-chd2@9371	liso-opx-chd2@8787	-2.3 (1)	-6.1 (3)	-4.9	-9.5 (1.5)	5.67
BOP-2	LPx^{irim}	igneous rim	$En_{98}Wo_1$	oxy-opx-chd2@9372	liso-opx-chd2@8788	-0.5 (1)	-4.6 (3)	-4.4	-8.2 (1.5)	5.54
BOP-2	LPx	outer BOP	$En_{98}Wo_1$	oxy-opx-chd2@9436	liso-opx-chd2@8824	-3.1 (1)	-7.4 (4)	-5.8	10.5 (2.0)	1.28
BOP-2	LPx	outer BOP	$En_{98}Wo_1$	oxy-opx-chd2@9437	liso-opx-chd2@8826	-2.7 (1)	-7.8 (3)	-6.4	33.2 (3.8)	0.405
BOP-2	LPx	outer BOP	$En_{98}Wo_2$	oxy-opx-chd2@9438	liso-opx-chd2@8827	-3.3 (2)	-7.4 (3)	-5.7	1.5 (1.1)	4.75
BOP-2	LPx	outer BOP	$En_{98}Wo_1$	oxy-opx-chd2@9440	liso-opx-chd2@8819	-3.3 (1)	-6.8 (3)	-5.1	-33.2 (1.2)	2.75
BOP-2	LPx	outer BOP	$En_{99}Wo_1$	oxy-opx-chd2@9441	liso-opx-chd2@8830	-2.4 (1)	-6.5 (3)	-5.3	-8.0 (1.1)	5.03
BOP-2	LPx	outer BOP	$En_{98}Wo_1$	oxy-opx-chd2@9442	liso-opx-chd2@8821	-3.0 (2)	-7.3 (3)	-5.7	-9.2 (1.7)	1.68
BOP-2	LPx^{irim}	igneous rim	$En_{98}Wo_1$	oxy-opx-chd2@9444	liso-opx-chd2@8856	-3.1 (2)	-7.3 (3)	-5.7	0.0 (1.4)	4.64
BOP-2	LPx^{irim}	igneous rim	$En_{99}Wo_1$	oxy-opx-chd2@9445	liso-opx-chd2@8857	-3.5 (1)	-7.4 (3)	-5.6	-0.6 (1.5)	5.55

Table S4: Continued

	phase	occurrence	compo*	O-analysis ID	Li-analysis ID	δ^{18}O	δ^{17}O	Δ^{17}O	δ^{7}Li	[Li]$^{\mu g \cdot g^{-1}}$
BOP-2	LPx	outer BOP	$En_{99}Wo_{1}$	oxy-opx-chd2@9487	liso-opx-chd2@8785	-3.8 (2)	-8.3 (3)	-6.3	-10.3 (0.61)	5.92
BOP-2	LPx	outer BOP	$En_{99}Wo_{1}$	oxy-opx-chd2@9488	liso-opx-chd2@8786	-2.6 (1)	-7.0 (4)	-5.6	-14.2 (0.86)	3.19
BOP-2	LPx	outer BOP	$En_{98}Wo_{1}$	oxy-opx-chd2@9489	liso-opx-chd2@8809	-2.5 (2)	-6.6 (3)	-5.3	-7.1 (2.5)	1.13
BOP-2	LPx^{irim}	igneous rim	$En_{98}Wo_{1}$	oxy-opx-chd2@9894	liso-opx-chd2@8925	-3.1 (1)	-6.5 (3)	-4.9	0.0 (1.6)	4.82
BOP-2	LPx	outer BOP	$En_{98}Wo_{1}$	oxy-opx-chd2@9899	liso-opx-chd2@8915	-2.3 (2)	-6.9 (3)	-5.7	-4.0 (1.5)	2.96
BOP-2	LPx	outer BOP	$En_{98}Wo_{1}$	oxy-opx-chd2@9900	liso-opx-chd2@8916	-3.0 (2)	-6.9 (4)	-5.3	-6.0 (1.3)	4.44
BOP-2	LPx^{irim}	igneous rim	$En_{98}Wo_{1}$	oxy-opx-chd2@9904	liso-opx-chd2@8858	-3.0 (1)	-6.5 (3)	-4.9	-10.9 (1.6)	4.72
BOP-2	LPx^{irim}	igneous rim	$En_{98}Wo_{1}$	oxy-opx-chd2@9905	liso-opx-chd2@8926	-1.2 (1)	-5.9 (4)	-5.2	0.3 (1.3)	5.23
BOP-2	LPx	outer BOP	$En_{97}Wo_{2}$	oxy-opx-chd2@9936	liso-opx-chd2@8829	-3.4 (1)	-7.4 (3)	-5.6	-10.1 (0.76)	5.92
BOP-2	LPx	outer BOP	$En_{98}Wo_{1}$	oxy-opx-chd2@9938	liso-opx-chd2@8823	-3.7 (2)	-7.8 (4)	-5.8	-12.9 (1.1)	3.18
BOP-2	LPx	outer BOP	$En_{98}Wo_{1}$	oxy-opx-chd2@9940	liso-opx-chd2@8843	-3.2 (1)	-7.3 (3)	-5.6	20.3 (2.4)	0.899
BOP-2	LPx	outer BOP	$En_{98}Wo_{1}$	oxy-opx-chd2@9941	liso-opx-chd2@8825	-3.0 (1)	-6.8 (3)	-5.2	24.8 (2.6)	0.658
BOP-2	LPx	outer BOP	$En_{97}Wo_{2}$	oxy-opx-chd2@9942	liso-opx-chd2@8828	-2.6 (1)	-6.6 (3)	-5.3	-5.8 (1.1)	3.64
BOP-2	LPx	outer BOP	$En_{98}Wo_{1}$	oxy-opx-chd2@9944	liso-opx-chd2@8820	-2.4 (2)	-6.8 (3)	-5.6	-0.4 (1.4)	4.75
BOP-2	LPx	outer BOP	$En_{99}Wo_{1}$	oxy-opx-chd2@9945	liso-opx-chd2@8831	-1.8 (2)	-6.1 (3)	-5.1	-20.8 (1.1)	2.46
BOP-2	LPx	outer BOP	$En_{97}Wo_{2}$	oxy-opx-chd2@9946	liso-opx-chd2@8847	-2.5 (1)	-7.2 (3)	-5.9	-0.7 (1.1)	4.96
BOP-2	LPx	outer BOP	$En_{98}Wo_{1}$	oxy-opx-chd2@9948	liso-opx-chd2@8848	-2.1 (2)	-6.4 (3)	-5.3	-21.5 (1.6)	2.78
BOP-2	LPx	outer BOP	$En_{99}Wo_{1}$	oxy-opx-chd2@9949	liso-opx-chd2@8849	-1.6 (2)	-6.1 (3)	-5.3	-4.1 (1.2)	5.25
BOP-2	LPx	outer BOP	$En_{99}Wo_{1}$	oxy-opx-chd2@9950	liso-opx-chd2@8850	-2.5 (1)	-6.6 (3)	-5.3	-13.0 (1.3)	2.92
BOP-2	LPx	outer BOP	$En_{98}Wo_{1}$	oxy-opx-chd2@9952	liso-opx-chd2@8851	-2.8 (1)	-6.6 (3)	-5.1	-23.2 (1.4)	2.64
BOP-2	LPx	outer BOP	$En_{98}Wo_{1}$	oxy-opx-chd2@9953	liso-opx-chd2@8852	-2.3 (1)	-6.6 (3)	-5.4	-17.1 (1.0)	4.37
BOP-2	LPx	outer BOP	$En_{97}Wo_{2}$	oxy-opx-chd2@9964	liso-opx-chd2@8893	-3.8 (2)	-7.5 (3)	-5.5	-2.6 (0.82)	6.73
BOP-2	LPx	outer BOP	$En_{98}Wo_{1}$	oxy-opx-chd2@9965	liso-opx-chd2@8894	-4.1 (2)	-7.3 (4)	-5.2	-10.8 (1.1)	5.27
BOP-2	LPx	outer BOP	$En_{97}Wo_{2}$	oxy-opx-chd2@9966	liso-opx-chd2@8895	-3.8 (1)	-7.4 (3)	-5.4	-12.2 (1.1)	4.57
BOP-2	LPx	outer BOP	$En_{98}Wo_{1}$	oxy-opx-chd2@9968	liso-opx-chd2@8896	-4.7 (2)	-7.9 (3)	-5.4	-4.0 (1.0)	6.35
BOP-2	LPx	outer BOP	$En_{98}Wo_{1}$	oxy-opx-chd2@9969	liso-opx-chd2@8897	-3.8 (1)	-6.6 (3)	-4.6	0.2 (1.1)	3.64
BOP-2	LPx	outer BOP	$En_{96}Wo_{3}$	oxy-opx-chd2@9972	liso-opx-chd2@8899	-3.4 (2)	-7.2 (3)	-5.5	19.4 (2.3)	0.253
BOP-2	LPx	outer BOP	$En_{94}Wo_{5}$	oxy-opx-chd2@9973	liso-opx-chd2@8900	-3.2 (2)	-7.0 (3)	-5.3	1.8 (1.5)	1.56
BOP-2	LPx	outer BOP	$En_{96}Wo_{4}$	oxy-opx-chd2@9974	liso-opx-chd2@8901	-3.3 (2)	-7.3 (3)	-5.6	10.3 (2.0)	0.258
BOP-2	LPx	outer BOP	$En_{95}Wo_{4}$	oxy-opx-chd2@9986	liso-opx-chd2@8902	-3.8 (2)	-7.7 (3)	-5.7	-3.4 (1.7)	1.64
BOP-2	LPx	outer BOP	$En_{94}Wo_{5}$	oxy-opx-chd2@9987	liso-opx-chd2@8911	-3.8 (2)	-7.4 (3)	-5.4	-0.4 (1.7)	0.906
BOP-2	LPx	outer BOP	$En_{93}Wo_{6}$	oxy-opx-chd2@9988	liso-opx-chd2@8912	-3.2 (1)	-6.0 (4)	-4.4	-2.9 (1.8)	1.47
BOP-2	LPx	outer BOP	$En_{91}Wo_{8}$	oxy-opx-chd2@9990	liso-opx-chd2@8913	-2.1 (2)	-5.8 (3)	-4.7	-1.6 (1.5)	1.35
BOP-2	LPx	outer BOP	$En_{90}Wo_{9}$	oxy-opx-chd2@9991	liso-opx-chd2@8914	-4.0 (1)	-6.8 (3)	-4.8	-1.1 (1.8)	1.23
BOP-2	LPx	outer BOP	$En_{99}Wo_{1}$	oxy-opx-chd2@9992	liso-opx-chd2@8808	-2.8 (2)	-5.7 (4)	-4.3	-7.3 (2.1)	2.07
BOP-2	LPx	outer BOP	$En_{99}Wo_{1}$	oxy-opx-chd2@9994	liso-opx-chd2@8810	-3.0 (1)	-7.3 (3)	-5.8	0.3 (2.3)	2.26
BOP-2	LPx	outer BOP	$En_{98}Wo_{1}$	oxy-opx-chd2@9995	liso-opx-chd2@8844	-3.9 (2)	-7.9 (4)	-5.8	-2.6 (1.1)	4.47
BOP-2	LPx	outer BOP	$En_{98}Wo_{1}$	oxy-opx-chd2@9996	liso-opx-chd2@8846	-3.0 (1)	-7.1 (3)	-5.6	-7.5 (0.86)	4.7
BOP-2	HPx	outer BOP	$En_{72}Wo_{27}$	oxy-cpx-chd2@9462	liso-cpx-chd2@8917	-3.5 (1)	-8.0 (3)	-6.2	0.5 (2.5)	0.324
BOP-2	HPx	outer BOP	$En_{71}Wo_{28}$	oxy-cpx-chd2@9463	liso-cpx-chd2@8918	-1.1 (2)	-5.3 (3)	-4.7	-8.8 (2.7)	0.506
BOP-2	HPx	outer BOP	$En_{65}Wo_{35}$	oxy-cpx-chd2@9464	liso-cpx-chd2@8919	-1.6 (1)	-6.8 (3)	-5.9	-4.9 (2.6)	0.435

Table S4: Continued

	phase	occurrence	compo*	O-analysis ID	Li-analysis ID	$\delta^{18}O$	$\delta^{17}O$	$\Delta^{17}O$	$\delta^{7}Li$	$[Li]^{\mu g \cdot g^{-1}}$
BOP-2	HPx	outer BOP	$En_{69}Wo_{31}$	oxy-cpx-chd2@9483	liso-cpx-chd2@8853	-2.7 (1)	-6.9 (3)	-5.5	-14.1 (3.3)	0.388
BOP-2	HPx	outer BOP	$En_{57}Wo_{42}$	oxy-cpx-chd2@9484	liso-cpx-chd2@8854	-2.5 (1)	-6.7 (3)	-5.4	0.8 (2.7)	1.06
BOP-2	HPx	outer BOP	$En_{74}Wo_{26}$	oxy-cpx-chd2@9485	liso-cpx-chd2@8920	-3.2 (1)	-7.8 (4)	-6.1	-6.8 (2.2)	0.747
BOP-2	Pl	inner BO	$An_{81}Ab_{19}$	oxy-pl-chd2@9458	liso-pl-chd2@9206	4.1 (1)	-1.1 (3)	-3.2	6.4 (5.6)	0.0079
BOP-2	Pl	inner BO	$An_{83}Ab_{17}$	oxy-pl-chd2@9459	liso-pl-chd2@9212	3.9 (1)	-1.6 (3)	-3.7	-4.6 (1.4)	0.129
BOP-2	Pl	inner BO	$An_{81}Ab_{19}$	oxy-pl-chd2@9460	liso-pl-chd2@9213	4.6 (1)	-0.3 (3)	-2.7	1.3 (2.6)	0.0463
BOP-2	Pl	outer BOP	$An_{83}Ab_{17}$	oxy-pl-chd2@9476	liso-pl-chd2@9215	6.0 (1)	0.0 (3)	-3.1	-2.0 (2.9)	0.0224
BOP-2	Pl	outer BOP	$An_{82}Ab_{18}$	oxy-pl-chd2@9477	liso-pl-chd2@9232	6.3 (1)	-0.2 (3)	-3.4	-2.0 (5.6)	0.00972
BOP-2	Pl	outer BOP	$An_{82}Ab_{18}$	oxy-pl-chd2@9478	liso-pl-chd2@9233	6.8 (1)	0.2 (2)	-3.3	1.5 (2.1)	0.0524
BOP-2	Pl	inner BO	$An_{81}Ab_{19}$	oxy-pl-chd2@9480	liso-pl-chd2@9235	4.9 (2)	-1.1 (3)	-3.7	10.3 (5.6)	0.0153
BOP-2	Pl	inner BO	$An_{81}Ab_{18}$	oxy-pl-chd2@9481	liso-pl-chd2@9236	4.9 (2)	-0.6 (3)	-3.2	0.4 (6.4)	0.0257
BOP-2	Pl	inner BO	$An_{83}Ab_{17}$	oxy-pl-chd2@10010	liso-pl-chd2@9214	2.1 (1)	-3.4 (4)	-4.5	-1.3 (2.9)	0.0356
BOP-2	Pl	outer BOP	$An_{82}Ab_{18}$	oxy-pl-chd2@10011	liso-pl-chd2@9234	7.0 (1)	0.9 (3)	-2.7	2.9 (2.4)	0.0525
PO-6	Ol	main	Fo_{99}	oxy-ol-chd6@9774	liso-ol-chd6@9115	-7.0 (1)	-10.1 (3)	-6.5	-8.4 (1.2)	0.504
PO-6	Ol	main	Fo_{94}	oxy-ol-chd6@9775	liso-ol-chd6@9116	-4.6 (1)	-6.9 (3)	-4.5	6.1 (1.4)	0.31
PO-6	Ol^{FeO}	main	Fo_{65}	oxy-ol-chd6@9776	liso-ol-chd6@9117	4.9 (2)	1.0 (3)	-1.6	3.4 (2.8)	0.274
PO-6	Ol	main	Fo_{98}	oxy-ol-chd6@9778	liso-ol-chd6@9118	-5.1 (2)	-7.4 (2)	-4.7	2.0 (1.3)	0.855
PO-6	Ol	main	Fo_{86}	oxy-ol-chd6@9781	liso-ol-chd6@9120	-3.6 (1)	-6.9 (3)	-5.1	1.9 (2.4)	0.0836
PO-6	Ol	main	Fo_{88}	oxy-ol-chd6@9782	liso-ol-chd6@9121	-4.8 (1)	-7.6 (4)	-5.1	3.9 (3.1)	0.0882
PO-6	Ol	main	Fo_{88}	oxy-ol-chd6@9783	liso-ol-chd6@9122	-3.7 (2)	-7.2 (3)	-5.3	7.7 (2.7)	0.115
PO-6	Ol^{irim}	igneous rim	Fo_{90}	oxy-ol-chd6@9793	liso-ol-chd6@9124	-4.6 (2)	-7.2 (3)	-4.8	9.0 (1.7)	0.26
PO-6	Ol^{irim}	igneous rim	Fo_{85}	oxy-ol-chd6@9794	liso-ol-chd6@9125	-4.5 (2)	-7.2 (3)	-4.9	-0.9 (4.2)	0.0532
PO-6	Ol^{irim}	igneous rim	Fo_{78}	oxy-ol-chd6@9796	liso-ol-chd6@9126	-4.0 (1)	-6.5 (3)	-4.4	8.9 (5.6)	0.0435
PO-6	Ol^{FeO}	main	Fo_{63}	oxy-ol-chd6@9805	liso-ol-chd6@9127	4.6 (1)	-1.2 (4)	-3.6	0.9 (5.5)	0.0562
PO-6	LPx^{irim}	igneous rim	$En_{96}Wo_{1}$	oxy-opx-chd6@9797	liso-opx-chd6@9175	-2.9 (2)	-6.0 (3)	-4.5	-14.8 (0.69)	9.01
PO-6	LPx^{irim}	igneous rim	$En_{97}Wo_{1}$	oxy-opx-chd6@9798	liso-opx-chd6@9176	-3.8 (1)	-6.6 (4)	-4.6	-7.7 (0.75)	12.2
PO-6	LPx^{irim}	igneous rim	$En_{98}Wo_{1}$	oxy-opx-chd6@9800	liso-opx-chd6@9173	-2.7 (1)	-6.1 (3)	-4.7	-6.6 (0.78)	8.94
PO-6	LPx^{irim}	igneous rim	$En_{98}Wo_{1}$	oxy-opx-chd6@9801	liso-opx-chd6@9174	-3.3 (2)	-7.1 (3)	-5.3	-17.1 (0.71)	4.85
PO-6	LPx^{irim}	igneous rim	$En_{97}Wo_{1}$	oxy-opx-chd6@9803	liso-opx-chd6@9184	-3.6 (2)	-7.2 (3)	-5.4	-21.2 (0.95)	7.05
PO-6	LPx^{irim}	igneous rim	$En_{98}Wo_{1}$	oxy-opx-chd6@9804	liso-opx-chd6@9185	-4.5 (2)	-7.9 (3)	-5.6	-7.2 (0.73)	13.6
PO-6	LPx^{irim}	igneous rim	$En_{98}Wo_{1}$	oxy-opx-chd6@9814	liso-opx-chd6@9186	-4.0 (1)	-7.3 (4)	-5.2	-6.2 (1.0)	3.55
PO-6	LPx^{irim}	igneous rim	$En_{98}Wo_{1}$	oxy-opx-chd6@9815	liso-opx-chd6@9187	-3.4 (2)	-6.9 (3)	-5.1	-14.3 (0.94)	10.5
PO-6	LPx^{irim}	igneous rim	$En_{98}Wo_{1}$	oxy-opx-chd6@9816	liso-opx-chd6@9188	-4.1 (1)	-7.3 (3)	-5.1	-14.5 (1.0)	5.52
PO-6	LPx^{irim}	igneous rim	$En_{98}Wo_{1}$	oxy-opx-chd6@9819	liso-opx-chd6@9189	-4.3 (2)	-7.4 (3)	-5.2	-25.0 (1.1)	5.01
PO-6	LPx^{irim}	igneous rim	$En_{98}Wo_{1}$	oxy-opx-chd6@9820	liso-opx-chd6@9190	-4.2 (1)	-7.2 (3)	-5.0	-21.7 (0.9)	5.61
PO-6	LPx^{irim}	igneous rim	$En_{98}Wo_{1}$	oxy-opx-chd6@9821	liso-opx-chd6@9191	-3.7 (2)	-6.7 (4)	-4.8	-17.8 (0.79)	6.7
BO-4	Ol	main	Fo_{98}	oxx-ol-chd4@565	liso-ol-chd4@9019	-4.1 (3)	-7.9 (4)	-5.8	14.4 (2.7)	0.115
BO-4	Ol	main	Fo_{99}	oxx-ol-chd4@566	liso-ol-chd4@9020	-4.1 (2)	-7.5 (4)	-5.4	6.6 (2.4)	0.106
BO-4	Ol	shell	Fo_{92}	oxx-ol-chd4@567	liso-ol-chd4@9021	-4.9 (2)	-8.0 (4)	-5.5	16.7 (1.7)	0.287
BO-4	Ol	shell	Fo_{95}	oxy-ol-chd4@9832	liso-ol-chd4@9037	-4.8 (2)	-7.6 (3)	-5.1	11.4 (1.5)	0.508

Table S4: Continued

		phase	occurrence	compo*	O-analysis ID	Li-analysis ID	$\delta^{18}O$	$\delta^{17}O$	$\Delta^{17}O$	$\delta^{7}Li$	[Li]$^{\mu g \cdot g^{-1}}$
	BO-4	Ol	shell	Fo_{90}	oxy-ol-chd4@9833	liso-ol-chd4@9039	-4.8 (1)	-7.4 (3)	-4.9	-1.4 (4.5)	0.0588
	BO-4	Ol	main	Fo_{99}	oxy-ol-chd4@9834	liso-ol-chd4@9040	-4.2 (2)	-7.1 (3)	-4.9	39.1 (2.7)	0.322
	BO-4	Ol	main	Fo_{99}	oxy-ol-chd4@9837	liso-ol-chd4@9042	-4.3 (2)	-7.3 (2)	-5.0	-5.3 (4.0)	0.143
	BO-4	Ol	main	Fo_{98}	oxy-ol-chd4@9838	liso-ol-chd4@9043	-5.5 (2)	-8.0 (4)	-5.1	5.9 (4.3)	0.0839
	BO-4	Ol	main	Fo_{98}	oxy-ol-chd4@9841	liso-ol-chd4@9045	-5.4 (2)	-9.2 (3)	-6.4	9.9 (2.0)	0.0836
	BO-4	Ol	main	Fo_{98}	oxy-ol-chd4@9852	liso-ol-chd4@9046	-4.0 (2)	-7.8 (4)	-5.7	14.1 (1.6)	0.129
	BO-4	Ol	main	Fo_{98}	oxy-ol-chd4@9854	liso-ol-chd4@9048	-3.6 (2)	-7.3 (3)	-5.4	2.7 (3.1)	0.0689
	BO-4	Ol	main	Fo_{97}	oxy-ol-chd4@9856	liso-ol-chd4@9049	-4.7 (1)	-7.7 (3)	-5.3	6.1 (1.7)	0.163
	BO-4	Ol	main	Fo_{97}	oxy-ol-chd4@9857	liso-ol-chd4@9022	-4.2 (1)	-8.5 (3)	-6.3	18.9 (1.5)	0.206
group 2	PO-7	Ol	main	Fo_{98}	oxy-ol-chd7@9571	liso-ol-chd7@9146	-6.1 (1)	-9.6 (3)	-6.4	0.1 (0.85)	1.53
	PO-7	Ol	main	Fo_{90}	oxy-ol-chd7@9572	liso-ol-chd7@9147	-6.3 (1)	-9.3 (3)	-6.0	10.2 (1.1)	0.234
	PO-7	Ol	main	Fo_{98}	oxy-ol-chd7@9582	liso-ol-chd7@9145	-5.6 (1)	-8.8 (3)	-5.9	-14.8 (1.1)	0.648
	PO-7	LPx^{irim}	igneous rim	$En_{98}Wo_{1}$	oxy-opx-chd7@9575	liso-opx-chd7@9192	-5.4 (2)	-8.6 (3)	-5.7	-15.0 (0.92)	8.52
	PO-7	LPx^{irim}	igneous rim	$En_{98}Wo_{1}$	oxy-opx-chd7@9576	liso-opx-chd7@9193	-5.8 (1)	-9.4 (3)	-6.3	-9.5 (0.95)	7.83
	PO-7	LPx^{irim}	igneous rim	$En_{98}Wo_{1}$	oxy-opx-chd7@9578	liso-opx-chd7@9194	-5.8 (1)	-9.5 (3)	-6.5	-14.4 (0.83)	6.83
	PO-1	Ol	shell-of-mantle	Fo_{99}	oxy-ol-chd1@9674	liso-ol-chd1@9136	-7.1 (1)	-10.0 (3)	-6.3	-6.2 (1.3)	0.491
	PO-1	Ol	shell-of-mantle	Fo_{93}	oxy-ol-chd1@9675	liso-ol-chd1@9137	-6.9 (1)	-9.3 (3)	-5.7	4.0 (1.3)	0.374
	PO-1	Ol^{FeO}	main	Fo_{65}	oxy-ol-chd1@9676	liso-ol-chd1@9138	5.8 (1)	0.8 (3)	-2.2	-2.4 (4.8)	0.108
	PO-1	Ol	shell-of-mantle	Fo_{97}	oxy-ol-chd1@9678	liso-ol-chd1@9139	-5.7 (2)	-9.6 (3)	-6.6	15.8 (4.5)	0.06
	PO-1	Ol	shell-of-mantle	Fo_{99}	oxy-ol-chd1@9679	liso-ol-chd1@9140	-5.5 (2)	-9.9 (3)	-7.0	-5.0 (3.4)	0.0694
	PO-1	Ol	shell-of-mantle	Fo_{100}	oxy-ol-chd1@9680	liso-ol-chd1@9142	-6.4 (2)	-10.1 (3)	-6.8	13.0 (3.8)	0.0822
	PO-1	LPx	main	$En_{93}Wo_{6}$	oxy-opx-chd1@9682	liso-opx-chd1@9256	-5.1 (2)	-8.8 (3)	-6.1	-5.9 (1.3)	3.53
	PO-1	LPx	main	$En_{92}Wo_{4}$	oxy-opx-chd1@9683	liso-opx-chd1@9257	-5.5 (2)	-9.8 (3)	-6.9	-0.3 (1.4)	2.75
	PO-1	LPx	main	$En_{95}Wo_{4}$	oxy-opx-chd1@9684	liso-opx-chd1@9258	-5.0 (1)	-8.6 (3)	-6.0	18.7 (1.9)	1.51
	PO-1	HPx	main	$En_{56}Wo_{43}$	oxy-cpx-chd1@9686	liso-cpx-chd1@9259	-6.2 (1)	-9.6 (3)	-6.4	8.7 (3.9)	0.129
	PO-1	HPx	main	$En_{59}Wo_{40}$	oxy-cpx-chd1@9687	liso-cpx-chd1@9260	-5.8 (2)	-9.5 (3)	-6.5	11.3 (3.7)	0.504
	PO-1	HPx	main	$En_{54}Wo_{45}$	oxy-cpx-chd1@9688	liso-cpx-chd1@9261	-6.8 (2)	-9.7 (3)	-6.2	-6.1 (3.9)	0.485
	PO-3c	Ol	main	Fo_{93}	oxy-ol-chd3c@9720	liso-ol-chd3c@9098	-5.9 (1)	-9.5 (3)	-6.4	-1.0 (3.5)	0.0869
	PO-3c	Ol	main	Fo_{81}	oxy-ol-chd3c@9721	liso-ol-chd3c@9099	-7.6 (1)	-9.8 (2)	-5.9	-12.2 (3.6)	0.0719
	PO-3c	Ol	main	Fo_{81}	oxy-ol-chd3c@9723	liso-ol-chd3c@9100	-6.8 (1)	-10.2 (2)	-6.7	-4.9 (3.4)	0.0781
	PO-3c	Ol^{FeO}	main	Fo_{62}	oxy-ol-chd3c@9724	liso-ol-chd3c@9101	-2.7 (2)	-4.5 (2)	-3.1	5.0 (4.9)	0.0483
	PO-3s	Ol	main	Fo_{99}	oxy-ol-chd3s@9726	liso-ol-chd3s@9102	-6.8 (1)	-10.0 (3)	-6.4	-4.6 (1.6)	0.392
	PO-3s	Ol	main	Fo_{86}	oxy-ol-chd3s@9727	liso-ol-chd3s@9103	-7.1 (1)	-9.7 (3)	-6.0	5.6 (1.1)	0.706
	PO-3s	Ol	main	Fo_{94}	oxy-ol-chd3s@9729	liso-ol-chd3s@9104	-6.9 (1)	-8.8 (2)	-5.3	5.6 (1.8)	0.548
	PO-3s	Ol	main	Fo_{97}	oxy-ol-chd3s@9730	liso-ol-chd3s@9105	-6.4 (2)	-9.5 (3)	-6.2	-18.2 (1.7)	0.307
	PO-3s	Ol	main	Fo_{94}	oxy-ol-chd3s@9731	liso-ol-chd3s@9106	-6.2 (1)	-9.1 (4)	-5.8	-5.6 (2.2)	0.359
group 3	PO-8	Ol	mantle	Fo_{96}	oxx-ol-chd8@601	lixo-ol-chd8@601	-16.7 (2)	-17.8 (3)	-9.1	-1.9 (1.1)	0.296
	PO-8	Ol	mantle	Fo_{93}	oxx-ol-chd8@602	lixo-ol-chd8@602	-44.2 (2)	-44.4 (5)	-21.4	-18.0 (1.1)	0.951
	PO-8	Ol	mantle	Fo_{92}	oxx-ol-chd8@603	lixo-ol-chd8@603	-45.4 (2)	-46.4 (3)	-22.8	-6.0 (1.4)	0.207
	PO-8	Ol	mantle	Fo_{97}	oxx-ol-chd8@745	lixo-ol-chd8@745	-49.9 (2)	-47.9 (4)	-22.0	-14.6 (1.6)	0.148
	PO-8	Ol	mantle	Fo_{96}	oxx-ol-chd8@746	lixo-ol-chd8@746	-48.9 (2)	-48.7 (4)	-23.3	-7.7 (1.6)	0.128

Table S4: Continued

	phase	occurrence	compo*	O-analysis ID	Li-analysis ID	$\delta^{18}O$	$\delta^{17}O$	$\Delta^{17}O$	$\delta^{7}Li$	$[Li]^{\mu g \cdot g^{-1}}$
PO-8	Ol^{irim}	igneous rim	Fo_{84}	oxx-ol-chd8@747	lixo-ol-chd8@747	-20.8 (2)	-24.3 (4)	-13.5	-3.6 (2.0)	0.0939
PO-8	Ol^{irim}	igneous rim	Fo_{93}	oxx-ol-chd8@748	lixo-ol-chd8@748	-43.8 (2)	-45.5 (4)	-22.7	-21.2 (1.5)	0.134
PO-8	Ol	mantle	Fo_{92}	oxx-ol-chd8@749	lixo-ol-chd8@749	-10.0 (2)	-11.4 (5)	-6.2	-8.8 (1.4)	0.181
PO-8	Ol	mantle	Fo_{92}	oxx-ol-chd8@750	lixo-ol-chd8@750	-18.7 (2)	-19.5 (5)	-9.8	-9.0 (1.5)	0.176
PO-8	Ol	mantle	Fo_{95}	oxx-ol-chd8@768	lixo-ol-chd8@768	-21.7 (3)	-23.6 (4)	-12.3	-5.8 (1.4)	0.217
PO-8	Ol	mantle	Fo_{98}	oxx-ol-chd8@769	lixo-ol-chd8@769	-17.2 (2)	-17.9 (5)	-9.0	-5.6 (1.7)	0.143
PO-8	Ol	mantle	Fo_{95}	oxx-ol-chd8@770	lixo-ol-chd8@770	-30.9 (3)	-33.0 (6)	-16.9	4.9 (0.88)	0.364
PO-8	Ol	mantle	Fo_{95}	oxx-ol-chd8@771	lixo-ol-chd8@771	-44.7 (2)	-46.0 (4)	-22.8	-10.4 (1.8)	0.0942
PO-8	Ol	mantle	Fo_{93}	oxx-ol-chd8@772	lixo-ol-chd8@772	-7.2 (2)	-11.5 (5)	-7.8	-9.5 (1.5)	0.144
PO-8	Ol^{irim}	igneous rim	Fo_{89}	oxx-ol-chd8@773	lixo-ol-chd8@773	-43.4 (2)	-46.1 (5)	-23.5	-7.5 (1.8)	0.106
PO-8	Ol^{irim}	igneous rim	Fo_{89}	oxx-ol-chd8@774	lixo-ol-chd8@774	-43.0 (2)	-45.5 (5)	-23.1	-3.9 (1.3)	0.2
PO-8	Ol	mantle	Fo_{97}	oxx-ol-chd8@778	lixo-ol-chd8@778	-17.7 (2)	-19.6 (4)	-10.4	-9.5 (1.0)	0.277
PO-8	Ol^{irim}	igneous rim	Fo_{89}	oxx-ol-chd8@779	lixo-ol-chd8@779	-8.7 (2)	-11.5 (5)	-7.0	-13.1 (1.2)	0.316
PO-8	Ol^{irim}	igneous rim	Fo_{89}	oxx-ol-chd8@780	lixo-ol-chd8@780	-3.8 (2)	-6.9 (5)	-4.9	-11.7 (1.0)	0.576
PO-8	Ol	mantle	Fo_{93}	oxx-ol-chd8@781	lixo-ol-chd8@781	-45.7 (2)	-45.9 (4)	-22.1	-9.4 (1.2)	0.243
PO-8	Ol	core	Fo_{81}	oxx-ol-chd8@801	lixo-ol-chd8@801	-11.3 (2)	-13.2 (5)	-7.3	-6.1 (1.7)	0.109
PO-8	Ol	mantle	Fo_{92}	oxx-ol-chd8@802	lixo-ol-chd8@802	-13.1 (2)	-14.8 (4)	-8.0	-13.1 (1.6)	0.147
PO-8	Ol	mantle	Fo_{96}	oxx-ol-chd8@803	lixo-ol-chd8@803	-35.8 (2)	-37.5 (5)	-18.9	-7.8 (1.6)	0.155
PO-8	Ol	mantle	Fo_{96}	oxx-ol-chd8@804	lixo-ol-chd8@804	-32.6 (2)	-35.4 (5)	-18.4	-11.4 (1.3)	0.215
PO-8	Ol	mantle	Fo_{96}	oxx-ol-chd8@805	lixo-ol-chd8@805	-8.2 (2)	-12.2 (4)	-7.9	-5.8 (1.7)	0.134
PO-8	Ol	mantle	Fo_{96}	oxx-ol-chd8@806	lixo-ol-chd8@806	-12.2 (2)	-15.2 (4)	-8.9	-2.7 (1.6)	0.133
PO-8	Ol	mantle	Fo_{91}	oxx-ol-chd8@822	lixo-ol-chd8@822	-46.5 (2)	-47.9 (5)	-23.7	-7.5 (1.4)	0.164
PO-8	Ol	mantle	Fo_{94}	oxx-ol-chd8@823	lixo-ol-chd8@823	-36.8 (2)	-38.8 (4)	-19.7	-6.9 (1.7)	0.145
PO-8	Ol	mantle	Fo_{85}	oxx-ol-chd8@824	lixo-ol-chd8@824	-43.1 (2)	-44.5 (4)	-22.1	-3.4 (1.8)	0.137
PO-8	Ol	mantle	Fo_{94}	oxx-ol-chd8@828	lixo-ol-chd8@828	-36.1 (2)	-35.8 (5)	-17.0	-13.4 (1.2)	0.217
PO-8	Ol	mantle	Fo_{92}	oxx-ol-chd8@829	lixo-ol-chd8@829	-37.4 (2)	-37.1 (4)	-17.7	-8.6 (1.2)	0.304
PO-8	Ol^{irim}	igneous rim	Fo_{82}	oxx-ol-chd8@830	lixo-ol-chd8@830	-7.9 (2)	-10.9 (4)	-6.8	-11.1 (0.86)	0.672
PO-8	Ol^{irim}	igneous rim	Fo_{87}	oxx-ol-chd8@831	lixo-ol-chd8@831	-43.2 (2)	-45.3 (4)	-22.8	-9.4 (1.4)	0.306
PO-8	Ol^{irim}	igneous rim	Fo_{86}	oxx-ol-chd8@833	lixo-ol-chd8@833	-11.7 (3)	-13.9 (4)	-7.8	-14.7 (1.9)	0.0869
PO-8	Ol^{irim}	igneous rim	Fo_{82}	oxx-ol-chd8@834	lixo-ol-chd8@834	-42.9 (2)	-44.7 (4)	-22.4	-23.1 (1.7)	0.12
PO-8	Ol	mantle	Fo_{91}	oxx-ol-chd8@849	lixo-ol-chd8@849	-8.6 (2)	-12.4 (5)	-7.9	-11.0 (1.4)	0.193
PO-8	Ol	mantle	Fo_{94}	oxx-ol-chd8@850	lixo-ol-chd8@850	-27.4 (2)	-29.8 (4)	-15.6	-2.4 (1.1)	0.306
PO-8	Ol	mantle	Fo_{94}	oxx-ol-chd8@851	lixo-ol-chd8@851	-49.1 (2)	-49.0 (4)	-23.5	-14.5 (1.8)	0.106
PO-8	Ol	mantle	Fo_{92}	oxx-ol-chd8@852	lixo-ol-chd8@852	-38.6 (3)	-40.3 (5)	-20.2	-6.8 (1.2)	0.233
PO-8	Ol	mantle	Fo_{92}	oxx-ol-chd8@853	lixo-ol-chd8@853	-21.6 (2)	-23.7 (4)	-12.5	-10.3 (1.4)	0.197
PO-8	Ol	mantle	Fo_{91}	oxx-ol-chd8@854	lixo-ol-chd8@854	-45.2 (2)	-47.1 (4)	-23.6	-10.9 (1.5)	0.154
PO-8	Ol	core	Fo_{89}	oxx-ol-chd8@858	lixo-ol-chd8@858	-17.0 (2)	-20.4 (4)	-11.6	-6.3 (1.4)	0.16
PO-8	Ol	core	Fo_{90}	oxx-ol-chd8@859	lixo-ol-chd8@859	-23.9 (2)	-26.0 (5)	-13.6	-8.0 (1.1)	0.259
PO-8	Ol	mantle	Fo_{95}	oxx-ol-chd8@860	lixo-ol-chd8@860	-45.4 (2)	-47.2 (4)	-23.6	-3.9 (1.4)	0.201
PO-8	Ol	mantle	Fo_{91}	oxx-ol-chd8@861	lixo-ol-chd8@861	-45.1 (2)	-46.5 (4)	-23.0	-5.9 (2.2)	0.0852

Table S4: Continued

	phase	occurrence	compo*	O-analysis ID	Li-analysis ID	δ^{18}O	δ^{17}O	Δ^{17}O	δ^{7}Li	[Li]$^{\mu g \cdot g^{-1}}$
PO-8	Ol	mantle	Fo_{93}	oxx-ol-chd8@862	lixo-ol-chd8@862	-37.6 (2)	-39.0 (4)	-19.4	-3.1 (2.9)	0.044
PO-8	Ol	mantle	Fo_{92}	oxx-ol-chd8@863	lixo-ol-chd8@863	-38.2 (2)	-40.4 (3)	-20.5	-6.5 (0.90)	0.355
PO-8	LPx^{irim}	igneous rim	$En_{93}Wo_{5}$	oxy-opx-chd8@9553	liso-opx-chd8@9262	-3.1 (1)	-7.1 (3)	-5.4	-2.9 (3.1)	0.591
PO-8	LPx^{irim}	igneous rim	$En_{92}Wo_{6}$	oxy-opx-chd8@9554	liso-opx-chd8@9263	-0.4 (1)	-5.7 (3)	-5.5	0.9 (2.1)	1.29
PO-8	HPx^{irim}	igneous rim	$En_{64}Wo_{35}$	oxy-cpx-chd8@9557	liso-cpx-chd8@9265	-5.5 (1)	-7.4 (3)	-4.5	-17.7 (5.2)	0.113
PO-8	HPx^{irim}	igneous rim	$En_{66}Wo_{33}$	oxy-cpx-chd8@9558	liso-cpx-chd8@9266	-4.8 (1)	-7.9 (3)	-5.3	-10.1 (3.3)	0.228
PO-8	HPx^{irim}	igneous rim	$En_{57}Wo_{42}$	oxy-cpx-chd8@9559	liso-cpx-chd8@9267	-5.6 (1)	-8.6 (3)	-5.7	-2.4 (3.0)	0.214
PO-8	HPx^{irim}	igneous rim	$En_{61}Wo_{38}$	oxy-cpx-chd8@9560	liso-cpx-chd8@9268	-5.7 (1)	-8.7 (3)	-5.7	-4.1 (2.3)	0.258
PO-8	Pl	mantle	$An_{82}Ab_{18}$	oxy-pl-chd8@9549	liso-pl-chd8@9237	4.3 (1)	-0.7 (3)	-2.9	-10.1 (4.7)	0.0512
PO-8	Pl	mantle	$An_{83}Ab_{17}$	oxy-pl-chd8@9550	liso-pl-chd8@9238	1.1 (1)	-2.8 (3)	-3.3	2.5 (3.8)	0.0591
PO-8	Pl	mantle	$An_{81}Ab_{19}$	oxy-pl-chd8@9551	liso-pl-chd8@9240	4.0 (2)	-1.6 (3)	-3.6	-4.6 (2.2)	0.122
PO-3n	Ol	main	Fo_{93}	oxy-ol-chd3n@9702	liso-ol-chd3n@9062	-8.5 (2)	-11.3 (3)	-6.9	5.2 (2.4)	0.214
PO-3n	Ol	main	Fo_{93}	oxy-ol-chd3n@9704	liso-ol-chd3n@9096	-23.6 (2)	-25.5 (4)	-13.2	5.5 (3.3)	0.0488
PO-3n	Ol	main	Fo_{95}	oxy-ol-chd3n@9707	liso-ol-chd3n@9095	-18.7 (2)	-20.7 (3)	-11.0	35.5 (1.9)	0.243
PO-3n	Ol	main	Fo_{77}	oxy-ol-chd3n@9709	liso-ol-chd3n@9093	-24.6 (2)	-27.1 (3)	-14.3	3.6 (2.3)	0.0984
PO-3n	Ol	main	Fo_{94}	oxy-ol-chd3n@9710	liso-ol-chd3n@9097	-14.2 (2)	-16.7 (3)	-9.3	4.3 (2.0)	0.119

Abbreviation compo* denotes major-element composition.
Ol, LPx, and HPx are olivine, low-Ca pyroxene, and high-Ca pyroxene at the main chondrule (including mantle or core regions).
Ol^{irim}, LPx^{irim}, and HPx^{irim} are olivine, low-Ca pyroxene, and high-Ca pyroxene at igneous rim.
Pl is plagioclase and Ol^{FeO} is olivine with chemical composition $Fo_{\leq 65}$.

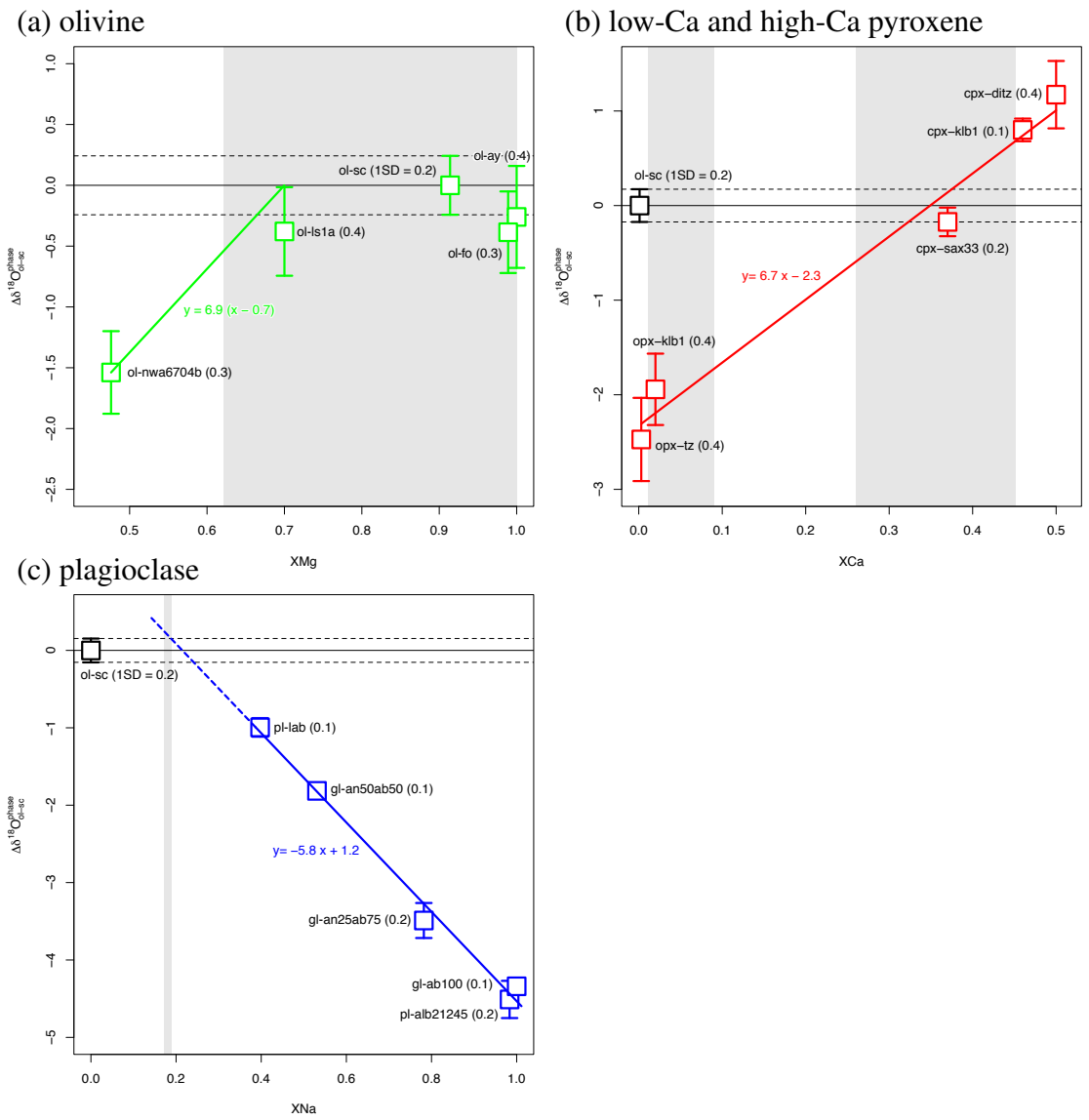

Figure S1: Matrix effects of (a) olivine, (b) low-Ca and high-Ca pyroxene, and (c) plagioclase in O-isotope analyses. Error bars and values in parentheses show 1SD deviations. Shaded regions indicate the compositional ranges of phases analyzed in this study.

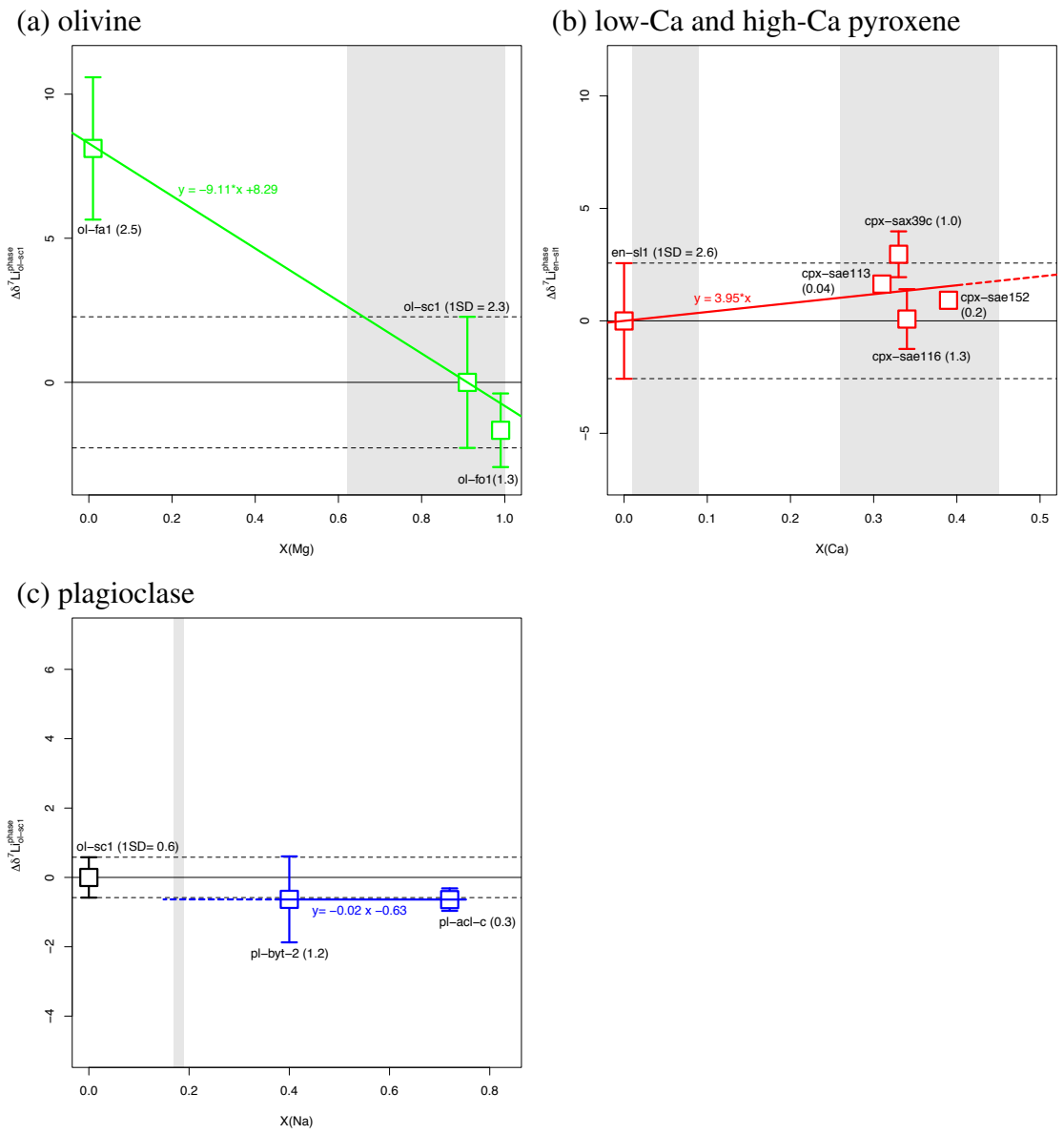

Figure S2: Matrix effects of (a) olivine, (b) low-Ca and high-Ca pyroxene, and (c) plagioclase in Li-isotope analyses. Error bars and values in parentheses show 1SD deviations. Shaded regions indicate the compositional ranges of phases in unknown samples analyzed by this study.

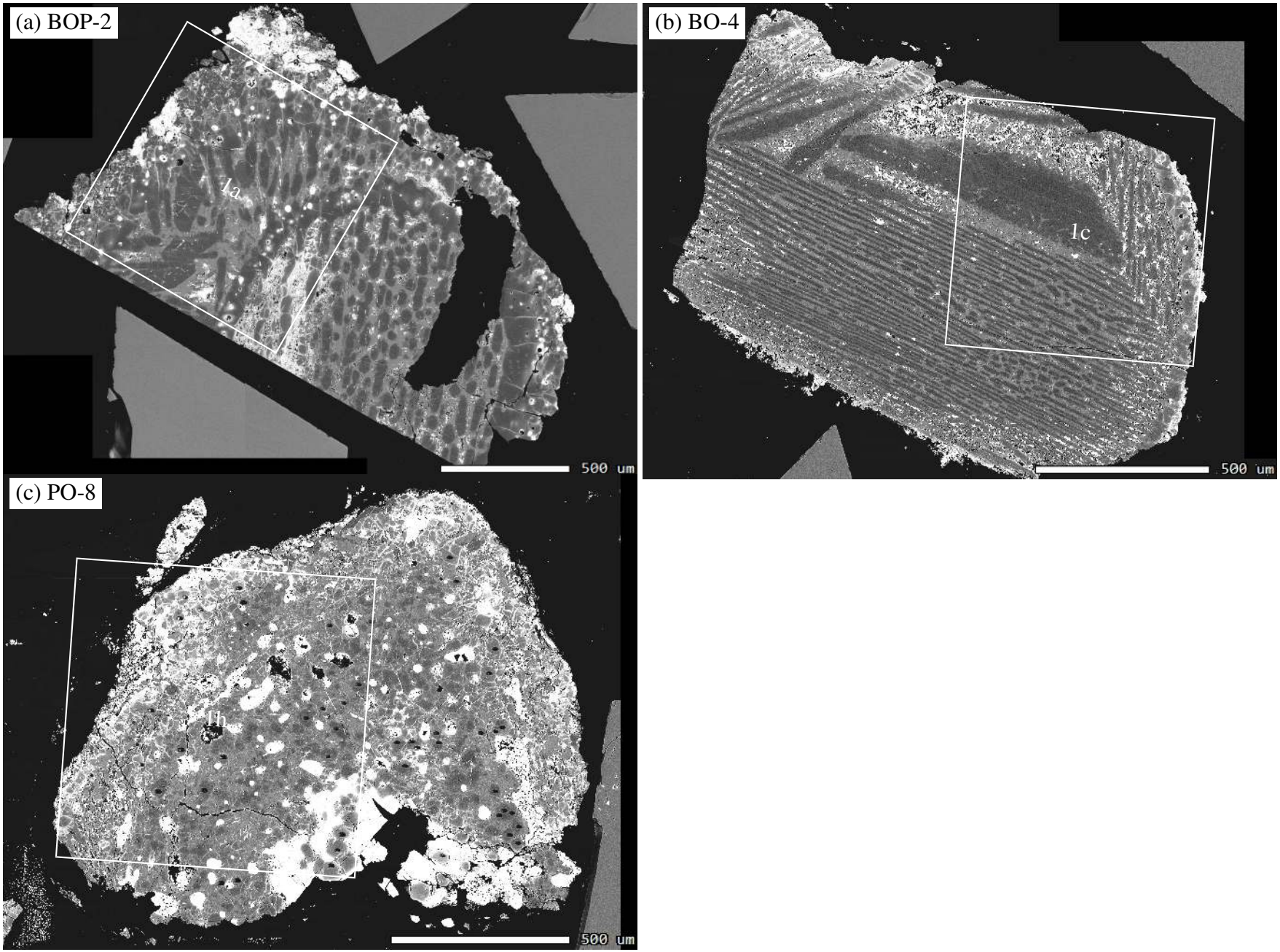

Figure S3: Backscattered electron images of (a) BOP-2, (b) BO-4, and (c) PO-8.

List of Figures

List of Tables